Damage behavior of ground pearlitic railway steel

Schotsman, B.

DOI
10.4233/uuid:0a0f240f-617c-40c9-809b-0ca61129465c

Publication date
2025

Document Version
Final published version

Citation (APA)
Schotsman, B. (2025). *Damage behavior of ground pearlitic railway steel*. [Dissertation (TU Delft), Delft University of Technology]. https://doi.org/10.4233/uuid:0a0f240f-617c-40c9-809b-0ca61129465c

DAMAGE BEHAVIOR OF GROUND PEARLITIC RAILWAY STEEL

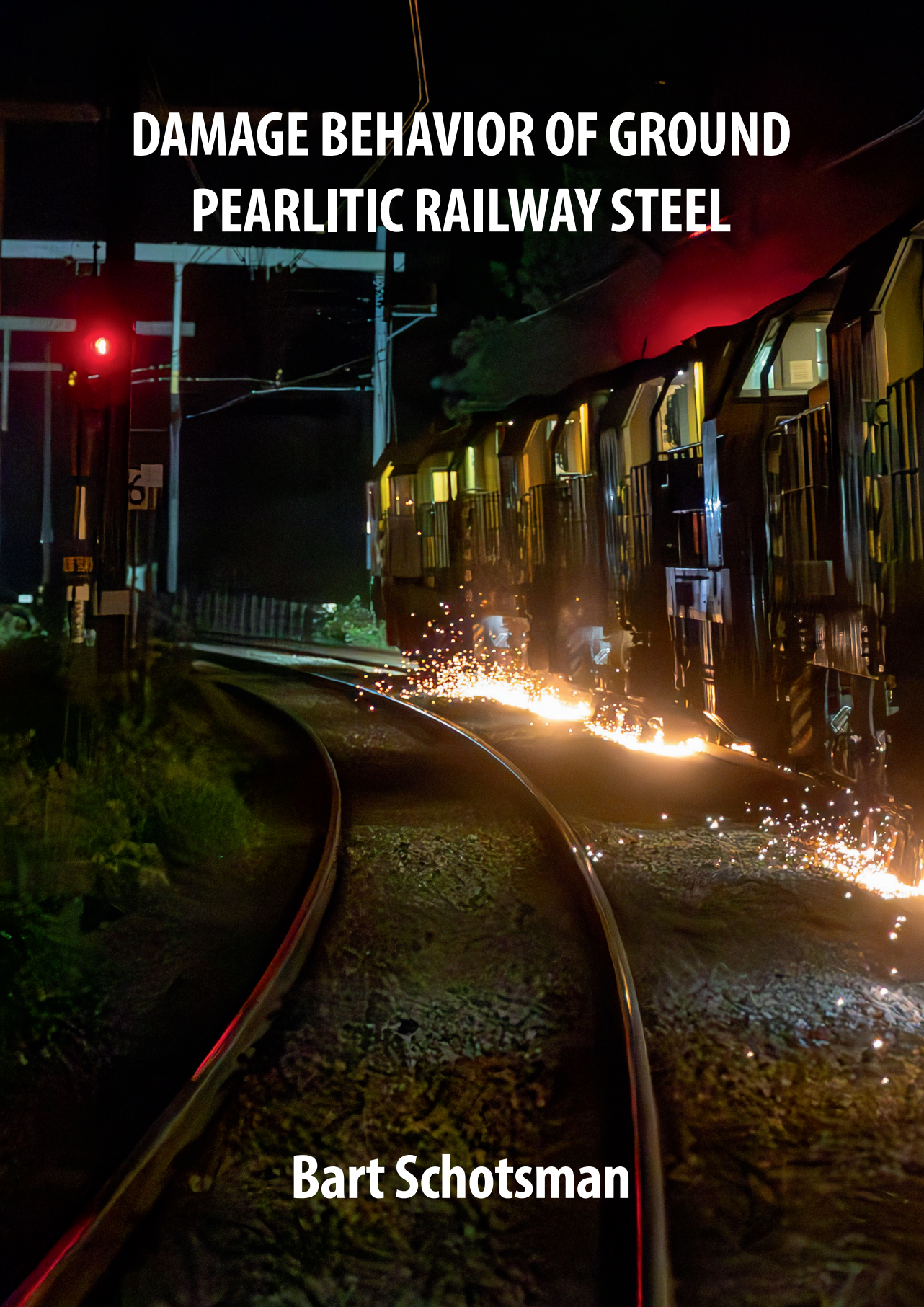

Bart Schotsman

DAMAGE BEHAVIOR OF GROUND PEARLITIC RAILWAY STEEL

DAMAGE BEHAVIOR OF GROUND PEARLITIC RAILWAY STEEL

Dissertation

for the purpose of obtaining the degree of doctor
at Delft University of Technology
by the authority of the Rector Magnificus prof. dr. ir. T.H.J.J. van der Hagen,
chair of the Board for Doctorates
to be defended publicly on
Wednesday 19 November 2025 at 15:00 o'clock

by

Bart SCHOTSMAN

Master of Science in Technology and Society,
Eindhoven University of Technology,
born in Rotterdam, The Netherlands.

This dissertation has been approved by the promotors

Composition of the doctoral committee:

Rector Magnificus,	Chairperson
Em Prof. dr. ir. J. Sietsma,	Delft University of Technology, promotor
Prof. dr. M.J. Santofimia Navarro,	Delft University of Technology, promotor
Prof. dr. ir. R.H. Petrov,	Delft University of Technology and University of Ghent, promotor
Independent members:	
Prof. dr. ir. R.P.B.J. Dollevoet	Delft University of Technology / ProRail
Prof. dr. ir. M.B. de Rooij	University of Twente
Prof. dr. D.I. Fletcher	University of Sheffield, UK
Dr. ir. R.H. Vegter	Delft University of Technology / M2i / SKF
Reserve member:	
Prof. dr. Z. Li	Delft University of Technology

This research was carried out under project number T18014 in the framework of the Partnership Program of the Materials Innovation Institute M2i (www.m2i.nl).

Printed by: Ridderprint | www.riderprint.nl

Front cover: © by Gijs Brefeld, Rail grinding in Enschede, The Netherlands
Back cover: Bart Schotsman, SEM image of a fresh ground surface. See Figure 2.4.

ISBN 978-94-6522-797-9

An electronic version of this dissertation is available at
http://repository.tudelft.nl/.

CONTENTS

SUMMARY

Traveling by train is becoming increasingly important, and, especially for long-distance travels, the current societal pressure for decarbonization is accelerating a modal shift from air travel to train travel.

With the introduction of faster and more comfortable trains, rolling contact fatigue (RCF) damage in rails started to spread over the networks, already in the 1990s. The RCF is controllable with newly introduced railhead profiles and with rails made of steels with improved wear resistant properties. Rails nevertheless need frequent maintenance, and for that purpose, high-powered precision grinding trains were developed. In **Chapter 1** the backgrounds and motivation to understand the mechanisms for damage development, in particular the relationship between rail grinding and the durability of the resulting rail contact surface, are presented.

Despite the proven rail life extension due to grinding maintenance, grinding-related rail damage may occur. The fixed mutual distance between initiations is a specific characteristic of this damage type. A second characteristic is the complete removal of the running surface during ongoing crack propagation. Grinding-related damage is mainly detected in the newly introduced rail steels with improved wear resistance.

Limited empirical evidence is available to explain the initiation of damage from the surface condition of the ground rail. The empirical evidence that is available points to an initiation mechanism involving deep grinding grooves and surface heating and rapid cooling during grinding, which produces hard and brittle white etching layers (WEL).

With grinding being an irreplaceable maintenance activity, the objective of the research is to obtain metallurgical understanding of the relation between the characteristic features of the freshly ground surface, the formation of the contact surface, and damage initiation. This understanding will support decisions on rail grinding design and further research into rail grinding and the development of applications, thereby avoiding the introduction of preferential locations for damage initiation.

Chapter 2 presents the results of a track test. In this test the processes acting on the freshly ground rail are studied in a medium-wide curve of a live track. This experiment is designed as follows. A new rail is installed before the start of the experiment and subsequently in-situ ground according to the ProRail specifications for preventive rail grinding. Inspections are performed during eight months to evaluate the contact surface formation and four rail samples were extracted for detailed tribological and metallographic evaluation.

First, the freshly ground rail surface is studied, and the surface condition is characterized. The grinding introduced facets on the rail head, and grinding roughness is present on these facets. This roughness has a normally distributed variation in height profile. Friction between abrasives and the rail surface caused deformation beneath the surface

and surface temperatures to rise to above A_{C3} leading to fresh WEL formation. Ploughing, typical for grinding processes, has resulted in the formation of ridges and slivers, which partially cover the freshly ground surface.

Inspection results and micrographs have revealed that roughness asperities are deformed and extruded under recurring wheel contacts, a process that proceeds fastest at the facet transitions. Most of the grinding-related WEL is fractured during the deformation processes and removed from the surface and fresh WEL is formed due to frictional heat generation during deformation.

The observed roughness-reduction mechanism contributes to the fast formation of the contact surface but carries the risk that detrimental particles cannot escape and become trapped. The results further show that especially deep grinding grooves containing WEL facilitate the initiation of damage. The characteristic ground surface features, successive steps in contact surface formation and damage initiation are captured in a novel schematic 5-stage wear model for ground rail surfaces.

The case study in **Chapter 3** is performed on rail samples extracted from the railway line Zutphen-Hengelo in The Netherlands. The objective of the study is to evaluate damage formation in rails subjected to light bi-directional traffic after grinding. For that purpose rail surface conditions, subsurface deformation patterns, and representative surface breaking damages are studied.

The rail surface shows, three years after the grinding maintenance, that grinding roughness is still present on the running surface, while on the gauge corner the roughness has worn away. These differences in wear are explained by the bi-directional use of the railway line. Tangential shear stresses acting on the gauge corner are independent of the direction of travel, causing locally a 'normal' wear rate whereas tractive shear stress reversal reduces the wear rate on the running surface.

The S-shaped deformation patterns of the lamellae of the pearlitic rail steel beneath the contact surface are explained by the tractive shear stress reversal and cracks propagate symmetrically in both running directions.

Finally, the damage initiation is explained by two, line-specific conditions that occur simultaneously. First, when traffic is light, rail wear is low and this wear rate is further reduced by the rolling direction reversal. Observations of the rail surface showed that these specific loading conditions prevent the complete removal of the ground surface features and thus the formation of a durable load-carrying surface. Second, rail corrugation is not fully removed by grinding, causing variations in the wheel contact conditions.

The case study shows that the sustainable maintenance of rails in lightly loaded railway lines requires a distinct specification, with special attention to the surface roughness after grinding and to the removal of short-pitch corrugations.

Chapter 4 presents the results of an experiment using a twin-disc test setup in which five representative surface conditions that may occur after rail maintenance, are studied. The objective of the experimental design was to evaluate the contact surface formation, the number of load cycles until the coefficient of friction between the two surfaces increases, and the level that is reached.

Periodic rail maintenance removes damage in a timely manner, but all characteristic surface features must also be worn away again and again by the passing wheels in order to obtain a smooth rail surface.

The experimental results show that the initial coefficient of friction is low. This is a known characteristic of freshly machined surfaces, but it is not reflected in the considerations in rail maintenance as found in the literature.

The results also reveal that when the contact surface is formed by asperity deformation, the coefficient of friction rises already after a low number of load cycles and a high level is reached. When deformation is insufficient and wear have to take place, the process takes more load cycles.

The third observation worth mentioning is that when rail maintenance leads to subsurface deformation and strain hardening, it can take longer for breaking-in processes to be completed.

The experimental results contribute to the determination of specific requirements for, for example, tool management during the performance of rail maintenance.

The railway industry is constantly striving for performance improvements, for example by developing rail steels with improved wear resistance, which can extend its service life. The increased wear resistance may result from controlled accelerated cooling after hot rolling. Another method is to alter the chemical composition. **Chapter 5** presents the results of an experimental study to determine the mechanical properties of a novel air-cooled, vanadium-alloyed, hypereutectoid rail steel. Fractographic evaluations are made to study the crack paths. The experimental results are compared with the performance of standard rail steels and a controlled accelerated cooled rail steel.

The air-cooled hypereutectoid rail steel and the hypo-eutectoid controlled accelerated cooled rail steel that are compared, exhibit comparable hardness, the material property that is traditionally used for the classification of rail steel grades. The mechanical behaviors of both rail steels are different. For example, the strain-hardening capacity and the crack growth rate of the air-cooled steel is higher compared to the controlled accelerated cooled rail steel.

The results of the linear elastic fracture mechanics tests are explained by means of a detailed characterization of the microstructure. Therefore the investigation contributes to the development of knowledge on the microstructure-mechanical relationships of pearlitic rail steels. In addition, the results also contribute to considerations in the selection of railway steel for specific applications.

Finally, **Chapter 6** discusses the main conclusions of the research presented in this thesis and the consequences for the performance of rail maintenance. It is concluded during the project that research on damage that may initiate on the freshly ground surface is a green field and, as a result, extensive research is necessary into various aspects. Recommendations for further research comprise the quantification of detrimental features of the freshly ground surface condition that were identified, the determination of limits of acceptable presence of these features, and the development of maintenance applications that are robust against the variations encountered in track.

SAMENVATTING

Reizen per trein wordt steeds belangrijker. Vooral bij lange-afstandsreizen zorgt de huidige maatschappelijke druk om CO2-vrij te reizen voor een snellere verschuiving van vliegreizen naar treinreizen.

In de jaren 90 van de vorige eeuw, na de introductie van snellere en comfortabelere treinen, begonnen spoorstaafdefecten, veroorzaakt door rolcontactvermoeiing (RCF), in een veel grotere mate te ontstaan. RCF in bogen bleek te kunnen worden beheerst door het aanpassen van spoorstaafkopprofielen samen met het toepassen van spoorstaven gemaakt van staal met verbeterde slijtageweerstand. De spoorstaven hebben echter regelmatig onderhoud nodig waarvoor krachtige slijptreinen zijn ontwikkeld. In **Hoofdstuk 1** worden de achtergronden en aanleiding beschreven om de mechanismen van schadeontwikkeling te begrijpen, met name de relatie tussen slijpen van spoorstaven en de duurzaamheid van de resulterende spoorstaafoppervlakteconditie.

Het regelmatig slijpen van de spoorstaven draagt aantoonbaar bij aan de levensduurverlenging. Echter, spoorstaafdefecten kunnen ook het directe gevolg zijn van de uitvoering van slijponderhoud. Een specifiek kenmerk van deze defecten is de repeterende defectinitiatie in de rijspiegel van de spoorstaaf waarbij de vaste onderlinge afstand van de initiaties is gelijk aan de karakteristieke lengte van het slijpproces. Een tweede kenmerk is de uitbrokkeling van het loopvlak van de spoorstaaf wanneer de spoorstaafdefecten groeien en de inwendige scheurvlakken elkaar ontmoeten. Dit type defect komt vooral voor in de recent geïntroduceerde railstaalsoorten met verbeterde slijtvastheid.

Over de kenmerken van het geslepen spoorstaafoppervlak waarin de defecten kunnen ontstaan is op dit moment weinig bekend. Er is enig empirisch metallurgisch bewijs dat diepe slijpgroeven bijdragen aan het ontstaan van defecten. Ook de snelle verhitting en snelle afkoeling tijdens het slijpen, waardoor harde en brosse lagen (white etching layers, WEL) aan het oppervlak ontstaan, lijken een rol te spelen in het initiatiemechanisme.

Slijpen is een onmisbare onderhoudsactiviteit om een lange levensduur van spoorstaven te bewerkstelligen. Het doel van dit onderzoek is daarom het verkrijgen van metallurgisch inzicht in de relatie tussen de karakteristieke eigenschappen van het geslepen spoorstaafoppervlak, de ontwikkeling van het contactoppervlak en de defectinitiatie. Het onderzoek zal daarmee bijdragen aan de verdere ontwikkeling van het slijpen van spoorstaven en aan de ontwikkeling van onderhoudssystemen om slijpschade in de toekomst te voorkomen.

In **Hoofdstuk 2** worden de resultaten gepresenteerd van een praktijktest waarin de ontwikkeling van het geslepen spoorstaafoppervlak in een spoorsectie in een boog is bestudeerd. Dit experiment is als volgt opgezet. Voor de start van het experiment is een nieuwe spoorstaaf geplaatst en vervolgens geslepen volgens de specificaties die ProRail heeft opgesteld voor cyclisch preventief slijpen. Vervolgens zijn gedurende acht maan-

den inspecties uitgevoerd om de ontwikkeling van het contactoppervlak vast te leggen. In verschillende fases van het experiment is in totaal vier keer een spoorstaaf uitgenomen voor nader onderzoek van het spoorstaafoppervlak en de vervorming onder het oppervlak.

Het geslepen oppervlak is, voordat treinbelasting plaatsvond, bestudeerd en gekarakteriseerd. De ronde spoorstaafcontour is na slijpen niet meer aanwezig. De contour wordt benaderd door facetten. Op ieder van deze facetten zijn slijpgroeven aanwezig. Typisch voor slijpen is dat het profiel van de ruwheid een normaal verdeelde variatie in ruwheidshoogte heeft. De wrijving die ontstaat tussen de slijpkorrel en het railoppervlak heeft gezorgd voor materiaalvervorming onder het oppervlak, en als gevolg van de temperatuurontwikkeling tot boven A_{C3} is er WEL ontstaan. Ploegen, typisch voor slijpprocessen, heeft geresulteerd in de vorming van ruggen naast de slijpgroef en extrusie van materiaal, waardoor het vers geslepen oppervlak gedeeltelijk wordt afgedekt.

Uit de inspectieresultaten en de bestudering van de microscoopfoto's is gebleken dat ruwheidspieken in het wiel-rail contact worden vervormd en geëxtrudeerd. Dit proces verloopt het snelst ter plaatse van de facetovergangen. Tijdens deze vervorming wordt ook het grootste deel van de, tijdens slijpen ontstane, WEL verbrijzeld en van het oppervlak verwijderd en verse WEL wordt gevormd als gevolg van wrijvingswarmte die ontstaat tijdens vervorming en de snelle afkoeling van het spoorstaafoppervlak.

Het beschreven vervormingsmechanisme draagt bij aan de snelle vorming van het contactoppervlak. Het risico is echter dat harde en mogelijk schadelijke delen niet worden verwijderd en worden ingesloten in het contactoppervlak. De experimentele resultaten bevestigen dat insluiting, bij vooral diepe slijpgroeven, plaatsvindt en zo preferentiele schade-initiatiepunten vormen. De karakteristieke oppervlakte-eigenschappen na slijpen, de opeenvolgende stappen waarin het contactoppervlak wordt gevormd en defecten kunnen ontstaan, zijn vastgelegd in een nieuw schematisch slijtagemodel voor geslepen spoorstaafoppervlakken.

In de casestudy in **Hoofdstuk 3** zijn spoorstaven onderzocht die afkomstig zijn uit de spoorlijn Zutphen-Hengelo. De defecten die na slijpen zijn ontstaan in de spoorstaven van deze lichtbelaste, enkelsporige spoorlijn zijn onderzocht, waarbij het spoorstaafoppervlak, de vervorming van de microstructuur en representatieve defecten zijn bestudeerd.

Het oppervlak laat zien dat, drie jaar na uitvoeren van het slijponderhoud, de slijpgroeven nog steeds zichtbaar zijn op het loopvlak van de spoorstaaf, terwijl deze wel zijn weggesleten in het gauge-cornergebied. De verschillen in slijtage kunnen worden verklaard door het bi-directionele gebruik van de spoorlijn. De tangentiële schuifspanningen die op de gauge corner worden uitgeoefend, zijn onafhankelijk van de rijrichting, hetgeen resulteert in een lokaal 'normale' slijtagesnelheid. De omkering van de rijrichting zorgt voor een omkering van de schuifspanningsrichting aan het loopvlak, hetgeen resulteert in een vertraging van de slijtage.

De S-vormige vervormingspatronen onder het contactoppervlak van de lamellen van het perlitische spoorstaafstaal zijn typerend voor de omkering van de schuifspanning. Scheurvorming in het materiaal ontwikkelt symmetrische scheurvlakken in beide rijrichtingen.

Het ontstaan van spoorstaafdefecten in deze spoorlijn wordt verklaard uit twee spe-

cifieke condities die tegelijkertijd optreden. Ten eerste, de trage slijtage van de licht belaste spoorstaaf welke door de omkering van de rijrichting nog wordt vertraagd. Uit de bestudering van het spooroppervlak blijkt dat de slijpruwheid niet volledig wordt verwijderd, waardoor er ook geen duurzaam contactoppervlak kan ontstaan. Ten tweede is het golfvormige slijtagepatroon op het spoorstaafoppervlak, een spoorstaafdefect dat golfslijtage wordt genoemd, niet volledig verwijderd, waardoor variaties in de wiel-contactcondities ontstaan.

De casestudy laat zien dat voor het onderhoud van spoorstaven in licht belaste spoorlijnen een specifieke specificatie vereist is, met speciale aandacht voor de oppervlakteruwheid na het slijpen en het volledig verwijderen van golfslijtage.

Door het uitvoeren van periodiek onderhoud van de spoorstaven worden defectinitiaties tijdig verwijderd. Het karakteristieke slijpoppervlak moet door de passerende treinwielen echter ook steeds worden weggesleten om een glad contactoppervlak te verkrijgen. **Hoofdstuk 4** presenteert de resultaten van een twin-disc experiment dat is ontworpen om het inloopgedrag van vijf representatieve oppervlaktecondities te bestuderen. Deze vijf oppervlaktecondities kunnen aanwezig zijn na de uitvoering van spoorstaafonderhoud.

De resultaten laten zien dat de wrijvingscoëfficiënt tussen het onderhouden oppervlak en, in dit experiment, de contra disc, initieel laag is, wat een bekende eigenschap is van bewerkte oppervlakken. De initieel lage wrijvingscoëfficiënt wordt in de literatuur echter nooit genoemd bij de overwegingen over het uitvoeren van onderhoud van spoorstaven.

De resultaten laten verder zien dat wanneer het contactoppervlak kan worden gevormd door vervorming van de ruwheid, de wrijvingscoëfficiënt al na een klein aantal belastingscycli toeneemt. Wanneer vervorming echter onvoldoende is en conformiteit door slijtage moet worden vergroot, duurt het langer voordat de wrijvingscoëfficiënt toeneemt. De derde bevinding is dat, wanneer spooronderhoud leidt tot vervorming en rekversteviging van het materiaal aan het oppervlak, het langer kan duren voordat de inloopprocessen, processen voorafgaand aan de stijging van de wrijvingscoëfficient, zijn voltooid.

De inzichten uit dit experiment dragen bij aan het bepalen van specifieke eisen voor bijvoorbeeld gereedschapsbeheer bij spoorstaafonderhoud.

De spoorwegindustrie is voortdurend op zoek naar prestatieverbeteringen, bijvoorbeeld door het ontwikkelen van spoorstaafstaal met een verbeterde slijtvastheid. Deze verbeterde slijtvastheid kan worden bereikt door warmtebehandeling, bij spoorstaven veelal door gecontroleerde versnelde afkoeling na het warmwalsproces. Een andere methode is het veranderen van de chemische samenstelling. **Hoofdstuk 5** presenteert de resultaten van experimenteel onderzoek aan de mechanische eigenschappen van een nieuw luchtgekoeld, vanadiumgelegeerd, hypereutectisch spoorstaafstaal. De resultaten van de lineair elastische breukmechanica testen worden vergeleken met de mechanische eigenschappen van standaard spoorstaafstaal en een warmtebehandeld spoorstaafstaal.

Het luchtgekoelde hypereutectsche staal en het hypo-eutectische warmtebehandelde spoorstaafstaal hebben een vergelijkbare oppervlaktehardheid, de materiaaleigenschap die traditioneel wordt gebruikt voor de classificatie van spoorstaafstaalsoorten. Het me-

chanische gedrag van beide staalsoorten is verschillend. De rekversteviging van het luchtgekoelde staal is bijvoorbeeld hoger, evenals de scheurgroeisnelheid.

De resultaten van de lineair elastische breukmechanica proeven worden toegelicht aan de hand van een gedetailleerde karakterisering van de microstructuur en dragen zo bij aan de ontwikkeling van kennis over de relatie tussen de microstructuur en de mechanische eigenschappen van perlitisch staal. Daarnaast dragen de resultaten ook bij aan de ontwikkeling van toepassingscriteria van spoorwegstaal.

Tot slot worden in **Hoofdstuk 6** de belangrijkste conclusies van het onderzoek in dit proefschrift bediscussieerd. Ook worden de implicaties voor de uitvoering van het spooronderhoud besproken. Tijdens het project is geconcludeerd dat onderzoek naar defecten die kunnen ontstaan uit het geslepen spoorstaafoppervlak nog een *green field* is. Uitgebreid vervolgonderzoek is daarom noodzakelijk. De aanbevelingen voor vervolgonderzoek omvatten de kwantificering van de aanwezigheid van risicovolle kenmerken in het geslepen oppervlak, de bepaling van limietwaardes voor acceptabele aanwezigheid van deze kenmerken en de ontwikkeling van onderhoudstoepassingen.

LIST OF TERMS

abrasive The sharp and hard particle that is bonded in the grinding wheel to remove the material. Abrasives are usually made from silicon carbide or aluminum oxide. 6, 45, 68, 123

angle of attack The angle that arises between the train wheel and the direction of travel of a train in a curved track section. 69

BEL Brown Etching Layer. BEL is formed from white etching layer (WEL) by tempering during successive reheating cycles with lower heat penetration. 45

blueing Temper color on the rail surface after grinding as a result of temperature raise of the surface during grinding. The degree of surface blueing is an important indicator of grinding quaility. See also burn. 4, 23

breaking-in Surface breaking-in takes place by simultaneously occurring processes to achieve geometrical conformity between surfaces, and a stable level of surface friction. 68

burn Purple to black surface oxidation resulting from local heating of the surface reaching surface temperatures above 735 °C. Burn is accompanied by WEL formation and may even result in damage formation due to thermal stresses. 124

facet The ground facet is a flat longitudinal strip on the rail surface that is applied during vertical-axis grinding. 3, 8, 45, 123

facet transition The connection between the facets on the ground surface. This facet transition is a zone. The width of this is determined by the variation in grinding groove lengths. 8, 45, 124

grinding pattern The specific sequence of grinding motor orientations in vertical-axis grinding and, as a result, the grinding positions at the transverse rail head. 8, 18

grinding wheel The grinding wheel or grinding stone is the tool mounted on the grinding motor, containing the bonded abrasives used to remove material. 3, 18, 126

head check A rail defect that mainly occurs in the gauge corner of the outer rail in curved tracks. Head checks are fine, closely-spaced cracks. 2

Hertz Wheel-rail contacts are considered Hertz contacts. Hertz contact is a frictionless contact between two bodies with curved surfaces. The stresses in a Hertz contact are within the elastic limit. 69

lay The lay is the orientation of the dominant pattern on the surface after grinding. This pattern is formed by abrasive particles following a similar trajectory as the grinding wheel is simultaneously moved along the rail. 123

preventive grinding Preventive grinding is a rail maintenance strategy where the rails are ground frequently, each time achieving a small grinding depth and thus only removing defect initiations. Also the rail is only re-profiled to a limited extent. 2, 18, 44

RCF Rolling contact fatigue (RCF) is the process of fatigue of the rail steel due to rolling/sliding contact resulting in damage initiation and cracks. 2

slip Slip is the speed difference in the wheel-rail contact between wheel and rail as a result of traction. 7, 51, 71

slip zone The part of the wheel-rail contact zone in which slip takes place. 77

stick zone The part of the wheel-rail contact zone in which no slip takes place. 77

target profile The transverse railhead profile that must be obtained during the re-profiling grinding maintenance of rails. 3, 8

UIC Union Internationale des Chemins de fer. International union of railways. 71

vertical-axis grinding Grinding with a grinding setup in which grinding motors are vertically placed. The grinding of the whole transverse rail profile is realized by grinding motor rotation. 8, 35, 123

WEL White Etching Layer. Hard and brittle surface layer that is formed on the rail surface by heating above the A_{C3}-temperature followed by fast cooling. 8, 45, 68, 124, 142

List of Symbols

α	Geometric factor depending on the specimen shape
ε	Strain
γ	(micro) Slip. The speed difference between wheel and rail
γ_D	Sliding distance
ϕ	Angle of attack
σ	Stress
σ_{UTS}	Ultimate tensile stress
σ_y	0.2%-offset yield strength
a	Crack length in Linear Elastic Fracture Mechanics (LEFM) C(T) test specimens
$\mathrm{d}a/\mathrm{d}n$	Crack growth rate
a_e	Cutting depth
d_e	Diameter of the grinding wheel
m	Paris-Erdogan crack growth coefficient
n	Strain hardening exponent
p	Contact pressure
p_m	Mean contact pressure
r_y	Radius of the plastic zone ahead of the crack tip
t	Ratio of the chip thickness to the average undeformed chip thickness
u	Crack mouth opening compliance
v	Clip gauge opening displacement
v_s	Circumferential speed of the grinding wheel
v_w	Grinding feed speed
A	Constant in the Archard law for sliding wear
B	Specimen thickness of C(T) test specimens

C	Paris-Erdogan material parameter
$C(T)$	Compact tension test specimen
E	Modulus of elasticity
F_C	Creep force
F_M	Traction force
F_N	Normal force
G	Number of abrasives of the grinding wheel that are simultaneously in contact with the workpiece
H	Hardness
HBW	Brinell hardness
HV	Vickers hardness
I	Plane-strain loading condition
K	Stress-intensity factor
K_Q	Provisional fracture toughness
ΔK	Stress-intensity factor range
M	Drive torque
P	Applied load
P_Q	Intersection of the offset line and the load-displacement record
Q	Wear volume
R	Load ratio
R_a	Average height of the surface profile
R_t	Height difference between the highest and lowest point of the surface profile
R_v	Valley depth of the roughness profile
S_Q	Secant offset
T	Temperature
V	Speed
V_D	Rotational velocity
W	Specimen width of C(T) test specimens
Z	Area reduction

1

INTRODUCTION

Railway transportation, both for freight and for passenger transport, is of great societal importance. Freight is transported from harbors to major multimodal hubs for further distribution, and frequently running trains bring commuters from suburbs to their job locations in the inner-cities. These inner-cities were difficult to reach in the past because of traffic congestion and are now rapidly being transformed into zero-emission zones.

Recently, railway transportation is gaining in importance for long-distance passenger travels as well. A development that is driven by societal pressure to reduce carbon emissions. To promote the modal shift from traveling by car and airplane to traveling by train, reliability of the services are of the utmost importance. In order to achieve high reliability, adequate and effective maintenance is required.

The transportation system consists of rolling stock, being the trains and train operators, and the railway track. Figure 1.1 shows the railway track construction consisting of a ballasted foundation embedding concrete sleepers on which spring-mounted railway rails are fit.

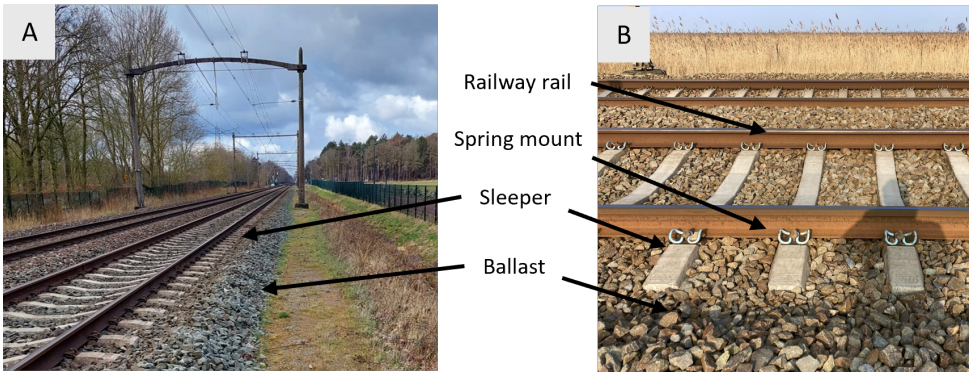

Figure 1.1: The railway track construction. A) Overview of a double-track railway section. B) Detail of a track construction consisting of ballast, concrete sleepers, spring mounts, and railway rails.

The rails form the interface with the trains and experience plastic deformation and wear as a result of hundreds of thousands of train wheels rolling over. To restore the rail profile and remove dents, imprints, and damage initiations, rail grinding is carried out.

During the past two decades, rail grinding was developed into cyclic preventive grinding and schedules were developed to effectively remove damage initiations and to improve the cross-sectional rail profile. The cyclic preventive grinding has proven to be cost effective as it increases the rail service life and reduces the frequency of unplanned repairs [1, 2].

This thesis presents in the introductory chapter, section 1.1, first the reasons for cyclic preventive grinding of railway rails. Then, in section 1.2, the motivation for this study is explained. In section 1.3, characteristics of freshly ground rail surfaces and the interaction with the introduction of rail steels with improved wear resistance are described. The last section, section 1.4, the thesis outline is presented.

1.1. PREVENTIVE RAIL MAINTENANCE

Preventive rail maintenance is a relatively new strategy that primarily involves grinding. In the past, rail grinding was mainly used as a corrective maintenance measure, for example to reduce noise emissions by removing rail corrugations. Only the top of the rail had to be ground for this. Since that time, rail grinding machines have been developed into precision equipment for reprofiling [3].

Rapid spread of rolling contact fatigue (RCF) damage in curved track sections in the 1990s [4] has led to an increase in rail replacements. Moreover, the cause of this rapid spread was initially not fully understood and the risks were underestimated [3]. It was discovered that new, high-speed, passenger trains were equipped with more tightly controlled suspension causing repeated running in the same band and high wheel-rail contact stresses which resulted in a ratcheting material response and damage initiation.

To reduce rail replacements, and to prevent rail fracture and derailments, rail infrastructure managers successfully introduced three important countermeasures:

- Stress-relief rail profiles were introduced in curved track sections. By adjusting the rail head geometry, wheel contact stresses are reduced. The lower contact stress in the relocated wheel contacts prevents the typical head check defects from initiating [2, 5]. The profiles require maintenance because they lose their stress-relieving effect due to wear.

- Rails steels with improved wear resistance were developed and introduced to reduce grinding frequencies and thus maintenance costs, and to elongate rail life.

- Ultrasonic inspection programs were expanded and eddy current measurement technology was introduced to detect superficial rail damages that can be removed by grinding before the unstable crack growth phase is reached [6].

Network-specific rail maintenance schedules were developed to maintain the stress-relief rail profiles. The majority of these can be considered ‘preventive grinding strategies’. Preventive grinding strategies consist of frequent grinding maintenance with limited capacity for reprofiling. The grinding frequency and material removal are balanced

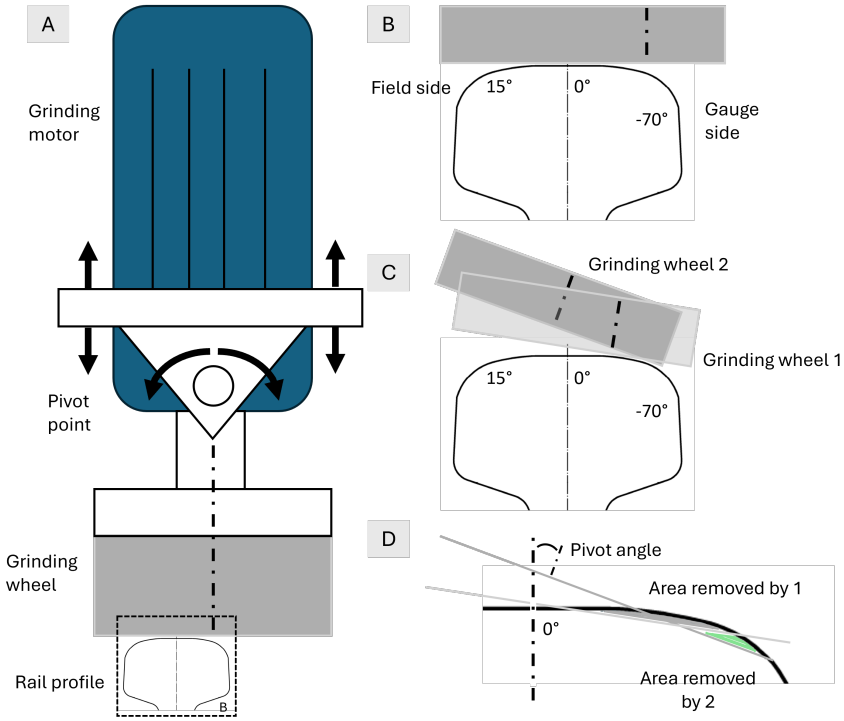

Figure 1.2: Vertical axis grinding setup. A) Each grinding motor is mounted in a frame that can be moved up and down, and rotated to grind different parts of the rail profile. B) Detail of A). The grinding motor is upright. C) Two grinding wheels, which are positioned one after the other in the grinding train, at different angular rotations. D) The area removed by grinding wheel 1 in grey, and by grinding wheel 2 in green. Grinding wheel 2 is positioned behind 1.

based on knowledge of track use, crack growth, and available grinding motor power [7]. The use of rail condition data to optimize schedules or to locally adjust preventive grinding strategies are recent and promising developments. Before introducing such a preventive grinding strategy, one or more 'preventive-gradual' grinding treatments are required to ensure that the rail head profile is as close as possible to the target profile [4].

Mainline rail grinders that are currently employed in high-speed single-pass grinding, are typically equipped with 48 to 96 24 kW grinding motors. Grinding speeds up to 20 km/h are realized and the application of durable grinding wheels prevents grinding wheel replacement during the short maintenance slots. The vertical-axis setup allows for a grinding motor rotation from $-70°$ to $15°$ for material removal and reprofiling of the full rail head. Figure 1.2 presents a schematic representation of a vertical axis grinding setup. The grinding motor is rotated to grind different areas of the profile, as is shown in Figure 1.2D. Each grinding wheel forms a facet on the surface.

The acceptance of rail grinding works in Europe is regulated by the EN13231-2:2020-standard [8]. This standard provides minimum requirements on the width of the resurfacing area of the rail head, dimensional tolerances, and surface characteristics. The

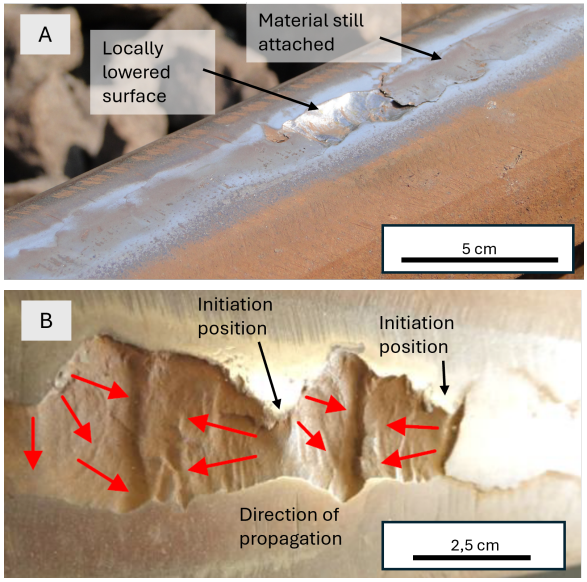

Figure 1.3: The grinding-related rail defects in a rail from a steel with increased wear resistance. A) The rail with the repetitive rail defect in track. The bright polished surface where the material is removed evidences the recent removal. B) The repetitive damage initiation positions are indicated by the black arrows. This mutual distance of the initiation positions is equal to the characteristic length of the grinding process. The red arrows indicate the local damage-propagation direction. The material spalls off after the subsurface crack planes of different damages intersect.

surface characteristics in the standard are defined by corrugation limits, introduced by the grinding process, surface quality, and limitations on blueing. This blueing refers to temper colors which are the result of temperature-specific oxide layer formation during grinding [9]. The surface quality is presented as an index representing track-specific classes of acceptable surface roughness.

With the introduction of stress-relief rail profiles and rail steels with improved wear resistance, the aforementioned countermeasures to prevent the initiation of fatigue damage due to rolling contact, and the introduction of frequent, preventive rail grinding, new rail defects have emerged.

Steenbergen [10] and Rasmussen et al. [11] point to specific aspects of the ground surface condition to explain the rail damages that arise shortly after the resurfacing treatment. Others, like Grassie [12], show damages in ground rails in the presence of grinding marks and wheel slip marks. Steenbergen [10] describes the damages as *'a hybrid defect type with properties of both short-pitch corrugation and rolling contact fatigue'*. Figure 1.3 shows rail defects that were observed in the rail infrastructure of ProRail. Figure 1.3A shows the defect as observed during track inspections. Figure 1.3B presents the repetitive defect initiations that coincide with the characteristic length of the grinding process. The propagation of subsurface cracks causes the removal of material from the contact surface.

1.2. MOTIVATION

ProRail has adopted all previously described countermeasures to prevent RCF damages to propagate. Around 2007, the installation of rails equipped with a newly developed stress-relief profile [5] made of steel with improved wear-resistant properties, started. These rails are installed in track sections with small radius curves and also in gently curved sections with radii up to 3000 m. Cyclic preventive grinding was gradually introduced to cover the whole network in 2013. The grinding frequency and grinding depth were based on the rate of damage initiation and propagation, as determined at various monitoring locations.

In 2014, grinding-related defects were first observed in the newly introduced rail steel grades. The number of occurrences peaked in 2017, concentrated in curves with a gentle curve radius of 2000 m to 2400 m. The occurrence of the defects reduced the rail life in these track sections to approximately seven years and ~95 Mt.

ProRail found a strong statistical correlation between the number of preventive grinding cycles and the presence of the defects [13]. Meanwhile, some empirical metallurgical evidence was available to explain the occurrence of the damage initiation as presented by, for instance, Steenbergen [10], Fau et al. [14], Rasmussen et al. [11] and Schotsman [15].

Since cyclic preventive grinding is still an irreplaceable maintenance activity to prevent rolling contact fatigue damage, further research is needed to evaluate the characteristics of the freshly ground surface condition and predict which features may serve as preferential sites for damage initiation. Preventive grinding strategies can then be adjusted accordingly to avoid the presence or to limit the extent of these critical features.

1.3. THEORETICAL BACKGROUND

The freshly ground rail surface is characterized by the presence of grinding-related surface roughness, the reprofiled rail head contour, and the blueing that may have occurred. In this section *Theoretical background*, the origin of these characteristic surface features is explained from the basic principles of grinding. Also the criticality of these features and the mechanisms that may explain the damage initiation in the ground rail surface are introduced. First the rail steel types will be briefly discussed.

1.3.1. RAIL STEELS

Classical rail steel is generally low-alloyed pearlitic steel with a hypo-eutectoid carbon content, i.e. lower than 0.78 wt%. The microstructure consists of pearlite colonies, which are composed of cementite and ferrite lamellae. Figure 1.4A presents a representative microstructure for standard-grade steels. The surface hardness of these standard-grade steels is 260 to 300 HBW [16].

The production method of rails is hot rolling of re-austenitized blooms of predefined size from which typically rails with a length of 108 m to 120 m are rolled. The hot-rolling is followed by air-cooling. Hot rolling may be followed by controlled accelerated cooling which leads to a lower lamellar thickness and thus an increase in hardness, strength, and wear-resistance [17, 18, 19]. The resulting refined microstructure is shown in Figure 1.4B.

To obtain better mechanical properties, modern rail steels are micro-alloyed and the carbon content is increased to a hyper-eutectoid level. Typical alloying elements are silicon, to prevent grain boundary embrittlement, manganese, for ductility, and chromium, to increase the transformation kinetics and decrease the subsurface hardness gradient. The surface hardness of these steels can be as high as 400 to 440 HBW [16].

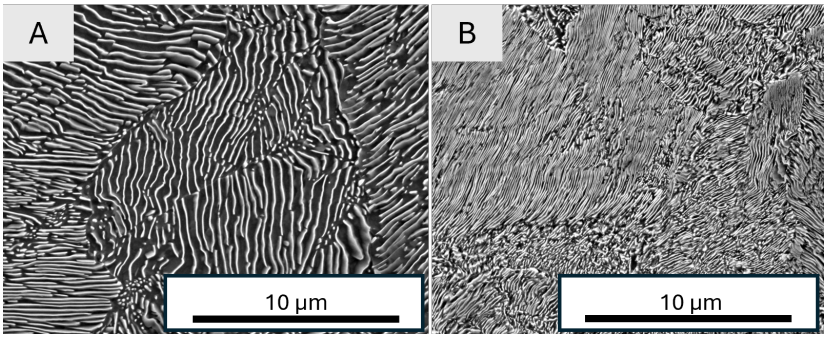

Figure 1.4: The microstructure of rail steels. A) Standard-grade R260Mn rail containing 0.53-0.77 wt% carbon and 1.25-1.75 wt% manganese [20]. The lamellar microstructure of pearlitic rail steel and different colonies are shown. B) A rail steel with improved wear resistance, R350HT. R350HT contains 0.70-0.82 wt% carbon and 0.65-1.25 wt% manganese [20]. The controlled accelerated cooling after hot-rolling reduced the lamellar thickness.

The improved wear resistance of modern and accelerated-cooled rail steels means that the stress-relief zone of the rail profile takes longer to wear away, and the frequency of re-profiling of the rail profile can be reduced. Industry guidelines and technical reports, like [21], suggest to install rails from these steels in curved sections with a radius up to 3000 m when the annual tonnage exceeds 10 Mt.

A recent trend is to install rails made from these steel types only in tighter curves as rail wear decreases due to the increasing share of rolling stock equipped with wheel lubrication. Another trend is the interest in rail steels with a bainitic microstructure. Monitored test sites are being set up by several rail infrastructure managers where rails from various manufacturers are installed. Rail steels with a bainitic microstructure are expected to be less susceptible to rolling contact fatigue [22]. This means that the life of the rail is less dependent on well-timed and frequent grinding.

1.3.2. SURFACE ROUGHNESS

The roughness after grinding is the first characteristic of the freshly ground surface of which the properties are explained.

Grinding is performed with grinding wheels containing abrasive particles. Conventional abrasives are Al_2O_3 and SiC which can be of mineral or synthetic origin. The size distribution of the abrasives is expressed by the grit number referring to the sieve maze; the higher the number, the finer the abrasive particles and the narrower the size distribution. The roughness height profile of the surface after grinding is the result of abrasive particle contact with particles that are randomly distributed in the volume of the grinding wheel.

Figure 1.5 presents a schematic illustration of a grinding wheel. Volume loss and wear of grinding wheels are an essential part of the self-sharpening process in grinding. Self-sharpening occurs by fracturing of abrasive particles and by removal of particles from the grinding wheel [23, 24].

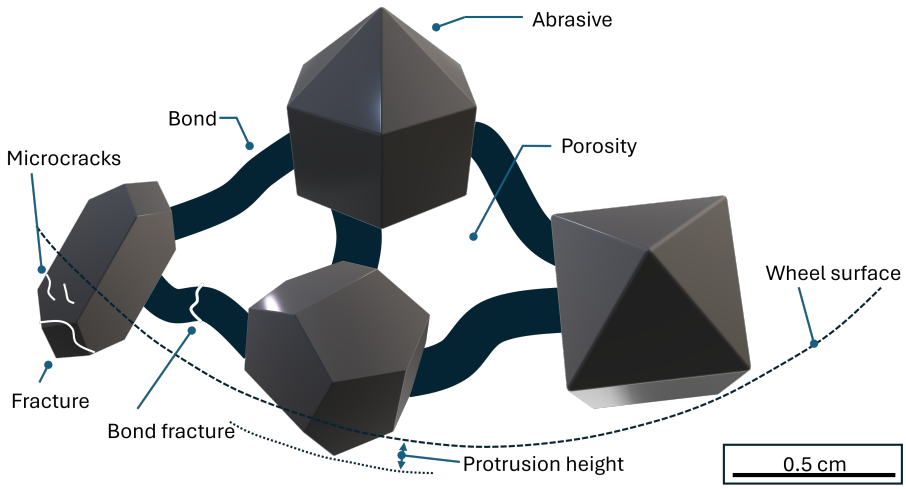

Figure 1.5: A schematic illustration of a grinding face of a grinding wheel. The abrasive particles have irregular shapes, various sizes, and orientations and are bonded in the grinding wheel. The different protrusion heights cause the roughness height distribution. Self-sharpening takes place by bond fracture or fracture of abrasives.

The surface roughness wears away during train passages to form the contact surface. Chen and Ishida [25] concluded that the roughness rapidly converges to a steady state value independent of the initial roughness height. They also observed that the reduction is faster at higher loads and higher levels of wheel slip. However, Daves and Fischer [26] and Kapoor et al. [27] showed that the presence of roughness leads to near-surface plastic strain differences. The discussion on wear and deformation is of interest because an increase in surface roughness, under conditions without wear, adversely affects fatigue life. Novovic et al. [28] published a literature review article on the fatigue life of machined surfaces. The reviewed literature showed that workpiece residual stress and surface roughness after grinding and hard turning contribute to a reduction in fatigue strength. However there is not much evidence on the influence of rail roughness due to grinding on the reduction of rail fatigue life [3].

1.3.3. GEOMETRY

The geometry of the rail after grinding is the second surface characteristic that is explained. The transverse rail head geometry and the longitudinal geometry are introduced separately.

The transverse rail head profile, as a result of vertical-axis grinding, is characterized by the presence of facets. The origination of these facets is previously shown in Figure 1.2C and D. The facet transitions, the zones connecting these facets, are associated with stress concentrations in the wheel-rail contact. Kalousek et al. [29] were the first to address the possible reduction in remaining rail life, and Mesaritis et al. [30] and Fau et al. [14] observed defects to initiate at the facet transition zones in rails during experiments performed under controlled laboratory conditions and in track.

To minimize the grinding time, specific sequences of grinding motor orientations were developed. These sequences are indicated as grinding patterns. The patterns are specific for the grinding equipment and for the target transverse rail head profile provided its actual profile. Kalousek et al. [29] presented the sequence of cross-sectional areas that were removed during consecutive grinding wheel passes. The removed area from the initially curved rail head profile results in a facet. The grinding motor angle of the second grinding motor is different and a second facet is formed, as shown in Figure 1.2. Nowadays, simulation software is used to design grinding patterns [31]. Grinding machines approach the target profile with an accuracy of 0.1 mm [32] and by reducing the power of the grinding motors in successive passes, the profile deviation from the target profile is reduced even further.

Concerning the longitudinal profile, the most important aspect to assess is the waviness of the rail surface due to grinding. The grinding process applies waviness in the rail surface with a characteristic length. This specific wavelength is determined by the distance that is covered during one revolution of the grinding wheel. Factors such as tool roundness, track stiffness, and vibrations in the grinding equipment contribute to location-specific wave height.

The excitation of the rail at this specific wavelength by the trains rolling over can cause noise emissions and damage. The allowable wave height after grinding is 0.01 mm [8]. Nielsen and Ekberg [33] additionally defined acceptance criteria to reduce noise emissions and prevent RCF damage from occurring. To reduce rolling contact noise emissions, also grinding speed variations can be introduced in subsequent grinding passes causing variations in wavelengths [24].

1.3.4. WHITE ETCHING LAYER FORMATION

The white etching layer (WEL) that may be formed during grinding is the third characteristic that is discussed. The WEL owes its name to its Nital etching resistance [34].

WEL can be formed after heating the surface above the A_{C3}-temperature followed by fast cooling. The specific energy, the energy dissipated in producing a chip [23], is between 10 J/mm^3 to 100 J/mm^3 for grinding [35], which is an order of magnitude higher compared to milling and turning operations [36]. Therefore material removal by grinding is limited by the probability of thermal damage to occur [37]. Subsequent grinding passes will even result in an additional rise in surface temperature [9, 38]. In order to prevent thick WEL to appear or quenching cracks to occur, the material removal must be

controlled.

Heat partitioning in a non-cooled grinding process is 60 % to 85 % [39], which indicates that 15 % to 40 % of the energy of the grinding motors is used for material removal. Frictional heat is generated in the chip-formation zone in front of the abrasive particle but the main friction area is between the wear surface of the abrasive particle and the rail surface [40]. The temperature in the chip formation zone is estimated to be higher than 1100 °C [9, 36, 38, 39]. The rubbing of the abrasive particles results in the temperature increase of subsurface layers, indicated as the grinding background temperature.

The high grinding temperatures result in the aggravation of surface oxidation and the accumulation of non-ferrous oxides [9]. Temper colors on rail steel, which range from yellow to black, are therefore an indication of the temperature during grinding. Blue indicates surface temperatures between 600 °C and 735 °C. Purple to black temper colors indicate a temperature higher than 735 °C and grinding cracks and quenching cracks might form [9].

In machining operations thermally induced WEL and mechanically induced WEL are distinguished [41]. For WEL formed under wheel rail contact two main theories are proposed [42]. The first theory suggests that WEL is formed by severe plastic deformation under repetitive wheel loads, resulting in grain refinement at the rail surface [43]. The main support for this theory is that martensitic structures observed at the surface contain more carbon in solution rather than being decarburized during the high surface temperatures necessary for transformation [44].

The second theory explains WEL formation from heating and fast cooling. Although simulation studies show that austenitization can take place during wheel and rail contact [45], there is still debate whether fast heating actually occurs and heating duration is sufficient for austenitization [44, 46].

When repetitive preventive grinding was introduced there was immediate concern about the formation of hard and brittle WEL. Magel et al. [3] observed WEL to be present in the roughness asperities and expected it to shear off, but Dikshit et al. [47] concluded already in 1991 that the WEL can induce damage. Over two decades later renewed research interest in the subject emerged and Steenbergen [10] and Rasmussen et al. [11] concluded that damage might start at WEL-particles and at transverse WEL-bands that originate from grinding maintenance.

1.4. THESIS OUTLINE

Applying rolling and sliding wheels on the rail surface causes plastic deformation and wear, and may cause damage initiation, crack propagation, and failure. The wheel contact might even cause a significant temperature increase, introducing thermal surface stresses or even phase transformations take place. These rolling and sliding wheels must first wear away the characteristic features of the ground surface to form a durable contact surface.

This research project aimed to gain metallurgical understanding of the relationship between the condition of the rail surface resulting from grinding and the durability of the contact surface. The thesis presents research results on the estimation of the criticality of features of ground surfaces on a microstructural scale, and the damage and wear mechanisms during contact surface formation.

Chapter 2 presents the surface characterization and microstructural evolution of railway rails in a track section with a curve radius of 1860 m, after preventive grinding. The aim of the field test was to gain insight into the relationship between the characteristic features of the freshly ground rail surface, the wear mechanisms, and the deformation processes. The study further evaluates the durability of the resulting contact surface.

To meet these objectives first the ground rail surface condition was characterized. This surface is the reference for the consecutive tribological and metallographic analyses of the surface evolution and the subsurface deformation. The observations were summarized in a novel schematic five-stage wear model for ground rail surfaces. The schematic wear model presents the surface evolution directly after grinding, and covers surface-roughness reduction mechanisms, the removal of grinding related WEL, deformation and finally damage initiation.

In **Chapter 3** the focus is on the surface evolution and microstructural deformation of standard grade rail steel under light bi-directional rail traffic conditions. The objective of the study was to determine reasons for damage initiation in rails of single-track railway lines. To conduct this case study, rail sections containing representative defects were extracted from the track, and the surface condition and representative surface breaking defects were evaluated.

After studying the rail surface it was concluded that, under the specific loading conditions, partial removal of rail corrugation and wheel slip caused a reduction in fatigue life. The loading conditions prevent the features of the ground surface from being completely removed. The shear stress reversal that occurs when a train passes from the opposite direction causes symmetrically shaped cracks to develop. This case study shows the complexity of the formation of a contact surface and further shows that locally specific loading conditions also require local specifications for rail maintenance.

Chapter 4 presents the research results that were obtained in a twin-disc experiment. After each resurfacing of the rail, by either grinding or milling, a new contact surface must be formed. The objective of the experiment was to study the contact-surface formation on the fresh surface and the transient behavior of the coefficient of friction.

The twin-disc experiment is designed such that the contact stress and the slip in the contact patch are representative for the contact conditions on the outer rail in a 1200 m radius curve.

In the experiment five machined and ground surfaces, representative for different resurfacing operations, are tested. The results show that the formation of the contact surface follows a different course for each of the surface conditions. Increasing the conformity between the surfaces appeared to be an essential aspect, and when surface wear is required to generate a sufficiently large contact area, it takes longer for the contact surface to form. It was further observed that when it takes more load cycles until the contact surface is formed, a lower coefficient of friction between the test disc and contra disc is achieved.

These findings are discussed with respect to observations in the literature and the relevance to the design of rail maintenance procedures.

Chapter 5 presents the microstructural characterization and results of an experimental study to determine the mechanical properties of a novel air-cooled vanadium-alloyed hypereutectoid rail steel.

In this experimental study, linear elastic fracture mechanics (LEFM) tests were performed using C(T)-specimens that were produced from freshly rolled rails. The test results were benchmarked with the mechanical properties of a controlled accelerated-cooled pearlitic steel and air-cooled pearlitic steels.

The results are discussed with respect to the distinct microstructural characteristics of the steel and the production route, and are supported by fractographic analyses. The experimental study fills knowledge gaps on the microstructure characteristics of pearlite steels that determine mechanical properties. The results contribute to the assessment of railway steel grades for application under specific loading conditions.

Finally, **Chapter 6** presents a discussion of the main conclusions that were derived from the research presented in this thesis, section 6.1.

The recent emergence of new rail defects shows that rail grinding involves more than just selecting the required grinding intervals and material removal. This research was a first exploration of a new research field, a field of research that ranges from materials science to contact mechanics and process technology. The recommendations section, section 6.2, provides suggestions for future research and process application development based on knowledge gaps identified during the conducted research.

BIBLIOGRAPHY

[1] R. de Vries, P. Sroba, and E. Magel. “Preventive Grinding Moves into the 21 st Century on Canadian Pacific Railway”. In: *Proceedings from the AREMA Annual Conference, Chicago, IL*. 2001.

[2] P. Sroba and M. Roney. *Rail grinding best practices*. Tech. rep. National research council of Canada, 2003.

[3] E. Magel et al. “The blending of theory and practice in modern rail grinding”. In: *Fatigue and Fracture of Engineering Materials and Structures* 26.10 (2003), pp. 921–929. ISSN: 8756758X. DOI: 10.1046/j.1460-2695.2003.00669.x.

[4] S.L. Grassie. “Rolling contact fatigue on the British railway system: Treatment”. In: *Wear*. Vol. 258. 7-8. Mar. 2005, pp. 1310–1318. DOI: 10.1016/j.wear.2004.03.065.

[5] R.P.B.J. Dollevoet. “Design of an Anti Head Check profile based on stress relief”. PhD thesis. University of Twente, 2010.

[6] U. Zerbst et al. “Introduction to the damage tolerance behaviour of railway rails - a review”. In: *Engineering Fracture Mechanics* 76.17 (Nov. 2009), pp. 2563–2601. ISSN: 00137944. DOI: 10.1016/j.engfracmech.2009.09.003.

[7] P. Hyde and D. Fletcher. “Planning Rail Grinding Using Crack Growth Predictions”. In: *Journal of Mechanical Systems for Transportation and Logistics* 3.1 (2010), pp. 216–225. DOI: 10.1299/jmtl.3.216.

[8] CEN. *EN13231-2 - Railway application - Track - Acceptance of works - Part 2: Acceptance of reprofiling rails in plain line, switches, crossings and expansion devices*. 2020.

[9] B. Lin et al. “Influence of grinding parameters on surface temperature and burn behaviors of grinding rail”. In: *Tribology International* 122 (June 2018), pp. 151–162. ISSN: 0301679X. DOI: 10.1016/j.triboint.2018.02.017.

[10] M. Steenbergen. “Rolling contact fatigue in relation to rail grinding”. In: *Wear* 356-357 (June 2016), pp. 110–121. ISSN: 00431648. DOI: 10.1016/j.wear.2016.03.015.

[11] C.J. Rasmussen et al. “Surface crack formation on rails at grinding induced martensite white etching layers”. In: *Wear* 384-385 (Aug. 2017), pp. 8–14. ISSN: 00431648. DOI: 10.1016/j.wear.2017.04.014.

[12] S.L. Grassie. “Squats and squat-type defects in rails: the understanding to date”. In: *Proceedings of the Institution of Mechanical Engineers, Part F: Journal of Rail and Rapid Transit* 226.3 (2011), pp. 235–242. ISSN: 0954-4097 2041-3017. DOI: 10.1177/0954409711422189.

[13] CQM. *Effect slijpen op defecten*. Tech. rep. CQM, 2016.

[14] F. Fau et al. "Effect of grinding quality, lubrication quality and rail hardness on flaking defect initiation on high rails". In: *Proc. 10 th Int. Conf. Contact Mech. Wear Rail/Wheel Systems CM2015, Colorado, USA*. Vol. 30. 2015.

[15] B. Schotsman. *Spalling defects in MHH steel rails, a study on the defect initiation and spalling after aggressive grinding*. Tech. rep. Utrecht: ProRail, Oct. 2017.

[16] CEN. *prEN13674-1 - Railway applications - Rail - Part 1: Vignole railway rails 46 kg/m and above*. European Committee for Standardization, 2023, pp. 1–112.

[17] D.J. Alexander and I.M. Bernstein. "Cleavage Fracture in Pearlitic Eutectoid Steel". In: *Metallurgical Transactions A* 20A (1989), pp. 2321–2335. DOI: 10.1007/BF02666667.

[18] M. Dollar, I.M. Bernstein, and A.W. Thompson. "Influence of deformation substructure on flow and fracture of fully pearlitic steel". In: *Acta Metallurgica* 36.2 (1988), pp. 311–320. DOI: 10.1016/0001-6160(88)90008-9.

[19] F.P.L. Kavishe and T.J. Baker. "Effect of prior austenite grain size and pearlite interlamellar spacing on strength and fracture toughness of a eutectoid rail steel". In: *Materials Science and Technology* 2.8 (1986), pp. 816–822. DOI: 10.1179/mst.1986.2.8.816. URL: https://doi.org/10.1179/mst.1986.2.8.816.

[20] CEN. *prEN13674-1 - Railway applications - Rail - Part 1: Vignole railway rails 46 kg/m and above*. European Committee for Standardization, 2023, pp. 1–112.

[21] A. Ekberg and B. Paulsson. *INNOTRACK: concluding technical report*. International Union of Railways (UIC), 2010.

[22] T. Lesage et al. "Head check resistance of B320 bainitic rail steel grade". In: *Materials Today Communications* 31 (June 2022). ISSN: 23524928. DOI: 10.1016/j.mtcomm.2022.103259.

[23] S. Kalpakjian, S.R. Schmid, and K.S. Vijay Sekar. *Manufacturing Engineering and Technology*. 7th SI Edition. Pearson, 2014, pp. 1–1224. ISBN: 9780133128741.

[24] Y. Kanematsu and Y. Satoh. "Influence of Type of Grinding Stone on Rail Grinding Efficiency ype of Grinding Stone on Rail Grinding Efficiency ype of Grinding Stone on Rail Grinding Efficiency ype of Grinding Stone on Rail Grinding Efficiency ype of Grinding Stone on Rail Grinding Efficiency". In: *Quarterly Report of RTRI* 52.2 (2011), pp. 97–102. ISSN: 1880-1765. DOI: 10.2219/rtriqr.52.97.

[25] H. Chen and M. Ishida. "Influence of Rail Surface Roughness Formed by Rail Grinding on Rolling Contact Fatigue". In: (2006).

[26] W. Daves and F.D. Fischer. "Modelling of the plastification near the rough surface of a rail by the wheel–rail contact". In: *Wear* 253.1-2 (July 2002), pp. 241–246. ISSN: 00431648. DOI: 10.1016/S0043-1648(02)00107-2.

[27] A. Kapoor et al. "Surface roughness and plastic flow in rail wheel contact". In: *Wear* 253 (2002), pp. 257–264.

[28] D. Novovic et al. "The effect of machined topography and integrity on fatigue life". In: *International Journal of Machine Tools and Manufacture* 44.2-3 (2004), pp. 125–134. ISSN: 08906955. DOI: 10.1016/j.ijmachtools.2003.10.018.

[29] J. Kalousek, P. Sroba, and C. Hegelund. "Analysis of rail grinding tests and implications for corrective and preventative grinding". In: *Fourth International Heavy Haul Railway Conference 1989: Railways in Action*. 1989, pp. 193–204.

[30] M. Mesaritis et al. "Post-field grinding evaluation of different rail grades in full-scale wheel/rail laboratory tests". In: *Tribology International* 177 (Jan. 2023). ISSN: 0301679X. DOI: 10.1016/j.triboint.2022.107980.

[31] Q. Lin et al. "Optimal design of rail grinding patterns based on a rail grinding target profile". In: *Proceedings of the Institution of Mechanical Engineers, Part F: Journal of Rail and Rapid Transit* 232.2 (Feb. 2018), pp. 560–571. ISSN: 20413017. DOI: 10.1177/0954409716679447.

[32] E.E. Magel and J. Kalousek. "The application of contact mechanics to rail profile design and rail grinding". In: *Wear* 253 (2002), pp. 308–316.

[33] J.C.O. Nielsen and A. Ekberg. "Acceptance criterion for rail roughness level spectrum based on assessment of rolling contact fatigue and rolling noise". In: *Wear* 271.1-2 (May 2011), pp. 319–327. ISSN: 00431648. DOI: 10.1016/j.wear.2010.10.013.

[34] T.S. Eyre and A. Baxter. "The formation of white layers at rubbing surfaces". In: *Tribology* 5.6 (1972), pp. 256–261. ISSN: 0041-2678. DOI: https://doi.org/10.1016/0041-2678(72)90104-2. URL: https://www.sciencedirect.com/science/article/pii/0041267872901042.

[35] T. Jin and D.J. Stephenson. "Analysis of Grinding Chip Temperature and Energy Partitioning in High-Efficiency Deep Grinding". In: *Proceedings of the Institution of Mechanical Engineers, Part B: Journal of Engineering Manufacture* 220.5 (2006), pp. 615–625. DOI: 10.1243/09544054JEM389. URL: https://doi.org/10.1243/09544054JEM389.

[36] Z.B. Hou and R. Komanduri. "On the mechanics of the grinding process, Part II - Thermal analysis of fine grinding". In: *International Journal of Machine Tools and Manufacture* 44.2-3 (Feb. 2004), pp. 247–270. ISSN: 08906955. DOI: 10.1016/j.ijmachtools.2003.09.008.

[37] A.S. Lavine, S. Malkin, and T.C. Jen. "Thermal Aspects of Grinding with CBN Wheels". In: *CIRP Annals* 38.1 (1989), pp. 557–560. ISSN: 0007-8506. DOI: https://doi.org/10.1016/S0007-8506(07)62768-1. URL: https://www.sciencedirect.com/science/article/pii/S0007850607627681.

[38] Z.Y. Zhang et al. "Thermal model and temperature field in rail grinding process based on a moving heat source". In: *Applied Thermal Engineering* 106 (Aug. 2016), pp. 855–864. ISSN: 13594311. DOI: 10.1016/j.applthermaleng.2016.06.071.

[39] S. Malkin and C. Guo. "Thermal Analysis of Grinding". In: *CIRP Annals* 56.2 (2007), pp. 760–782. ISSN: 00078506. DOI: 10.1016/j.cirp.2007.10.005.

[40] C. Yao et al. "Experimental study on grinding force and grinding temperature of Aermet 100 steel in surface grinding". In: *Journal of Materials Processing Technology* 214.11 (2014), pp. 2191–2199. ISSN: 09240136. DOI: 10.1016/j.jmatprotec.2014.04.013.

[41] S.B. Hosseini et al. “Formation mechanisms of white layers induced by hard turning of AISI 52100 steel”. In: *Acta Materialia* 89 (2015), pp. 258–267. ISSN: 13596454. DOI: 10.1016/j.actamat.2015.01.075.

[42] V. Mattos Ferreira et al. “Microstructure Development of Pearlitic Railway Steels Subjected to Fast Heating”. In: *SSRN Electronic Journal* 221 (2022), p. 110989. ISSN: 0264-1275. DOI: 10.2139/ssrn.4108630. URL: https://doi.org/10.1016/j.matdes.2022.110989.

[43] W. Lojkowski et al. “The mechanical properties of the nanocrystalline layer on the surface of railway tracks”. In: *Materials Science and Engineering A* 303.1-2 (2001), pp. 209–215. ISSN: 09215093. DOI: 10.1016/S0921-5093(00)01948-1. arXiv: arXiv:1011.1669v3.

[44] S.B. Newcomb and W.M. Stobbs. “A transmission electron microscopy study of the white-etching layer on a rail head”. In: *Materials Science and Engineering* 66.2 (1984), pp. 195–204. ISSN: 00255416. DOI: 10.1016/0025-5416(84)90180-0.

[45] A Kumar et al. “Microstructural evolution of white and brown etching layers in pearlitic rail steels”. In: *To Be Published* (2019). ISSN: 1359-6454. DOI: 10.1016/j.actamat.2019.04.012. URL: https://doi.org/10.1016/j.actamat.2019.04.012.

[46] G. Baumann, H. J. Fecht, and S. Liebelt. “Formation of white-etching layers on rail treads”. In: *Wear* 191.1-2 (1996), pp. 133–140. ISSN: 00431648. DOI: 10.1016/0043-1648(95)06733-7.

[47] V. Dikshit, P. Clayton, and D. Christensen. *Investigation of rolling contact fatigue in a head-hardened rail*. Tech. rep. 1991, pp. 89–102.

2

SURFACE CHARACTERIZATION AND MICROSTRUCTURAL EVOLUTION OF RAILWAY RAILS IN A MEDIUM-WIDE CURVE AFTER PREVENTIVE GRINDING

Preventive grinding of rails is a recurring maintenance routine to remove damage initiated in the wheel-rail contact. The grinding routine increases the service life of rails and reduces operational costs. Despite these benefits, grinding-related defects are observed. In this work a field test is performed to investigate the contact-surface formation and to better understand its durability. Surfaces after grinding are studied at different stages of the test to characterize wear mechanisms and deformation. The freshly ground surface exhibits a higher roughness and is composed of facets. It is determined that roughness asperities are extruded and fill grinding grooves in the process. High contact stresses at the facet transitions accelerate the extrusion of roughness asperities and the fast formation of the contact surface. The analysis further shows that deeper grinding grooves prevent homogeneous deformation. Strain concentrations arise due to the inhomogeneous deformation leading to damage initiation sites. These grooves are still present in the rail surface after the test. The evolution of the ground surface is captured in a schematic wear model.

This chapter is based on: B. Schotsman, M.J. Santofimia, R.H. Petrov, J. Sietsma, "Surface characterization and microstructural evolution of railway rails in a medium-wide curve after preventive grinding", Wear, 2025, Volumes 580–581, 206237, ISSN 0043-1648, https://doi.org/10.1016/j.wear.2025.206237.

2.1. INTRODUCTION

Travelling by train is safe and has low environmental impact, especially for high-speed long-distance travel. During the travel, the wheels of the train are carried and guided by steel rails which leads to wear and damage in the wheel-rail contact zone. In medium-wide curves, the formation of damages and the subsequent crack propagation in rails can be faster than the wear rate [1, 2, 3]. Therefore, the objective of preventive grinding is to remove these damage initiations and to restore the limited worn transverse rail head profile. Recurring grinding increases the rail service life and reduces operational costs [4, 5, 6].

Grinding of rails is typically a non-cooled process executed by systems equipped with multiple grinding motors that are placed vertically. The grinding wheels are shifted by grinding motor rotation to grind the entire rail head. Dedicated grinding patterns are developed for efficient performance [7, 8, 9]. When the grinding motor power is reduced in consecutive passes, surface quality and conformity with the target profile are further improved [9].

Despite the known benefits, the literature points to specific grinding-related surface features that may cause damage initiation after grinding [10, 11, 12, 13]. Tribological and metallographic research on this topic is only available to a limited extent, although recent publications show a renewed interest [11, 12, 14, 15].

The vertical placement of the grinding motors results in characteristic longitudinal strips on the rail head contour after grinding, which are called facets. Transition zones between the facets are associated with high contact stresses [8, 14]. For instance, Fau et al. [13] observed flaking defects to arise from these zones.

During grinding, material is removed by cutting and ridge formation takes place by ploughing [16]. The size distribution of the abrasive particles, the orientation and penetration of these particles [17, 18] cause a characteristic roughness profile. As a result, the first wheel contacts after grinding are on roughness asperities [19], causing material deformation, extrusion, and generally a high wear rate [20, 21, 22].

White etching layers (WEL) are formed after a temperature increase above A_{C3}, followed by rapid cooling [23]. Such high temperatures are achieved while grinding by the friction of the abrasive particles with most of the generated heat being transferred to the rail [24]. WEL are associated with various damage mechanisms. Rasmussen [12] observed that damage started at transverse, grinding-related, WEL stripes and Steenbergen [25] suggested that the damage initiates at WEL patches that are pressed into the microstructure. The grinding-related WEL are typically thinner on high-strength rail steels compared to standard grade rail steels [26]. However, from high strength steels a smaller portion of the WEL breaks off compared to standard grades [15].

The objective of the present study is to better understand the relation between the ground rail surface characteristics, wear and deformation processes, and to evaluate the durability of the formed contact surface. For this purpose a field test was performed. A new rail was installed and subsequently in-situ ground to standard specifications for preventive rail grinding. For detailed studies of wear mechanisms and subsurface deformation, rail samples were extracted at different stages of contact-surface formation.

The freshly ground rail surface was analyzed with special attention to transition zones, roughness, and WEL. The results of this field test provide new insights into wear mechanisms acting on the rail surface and the present study also identifies damage-promoting aspects of the ground surface condition.

2.2. EXPERIMENTAL DETAILS

2.2.1. FIELD TEST LOCATION AND RAIL STEEL SELECTION

Figure 2.1 shows the location of the grinding field test. This location is selected because of its history of rail damage initiation, head checks and studs, accessibility for inspection, and moderate annual line load. The local train speed is 130 km h^{-1} and constant. Table 2.1 presents the relevant data of the track layout. The rail profile, curve radius, cant, which is the superelevation between the inner and outer rail, and the cant deficiency, provided the curve radius and train speed.

Table 2.2 shows the train traffic that passed the test site during the test. Trains were registered at the hot-bearing detector 5 km south of the test site. Axle load data from the closest weighing-in-motion measurement systems are coupled to these records. The table presents the cumulative and average axle loads, the latter accompanied by the standard deviation. Note that the typical local trains are short and equipped with 6 axles.

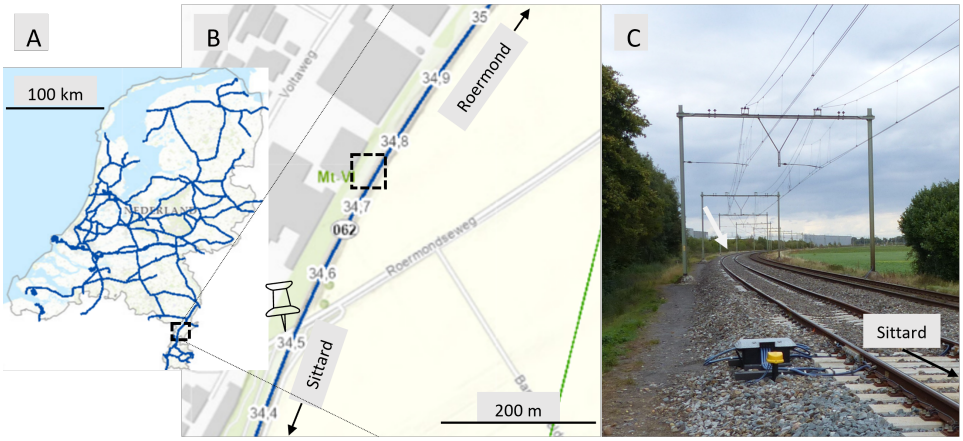

Figure 2.1: The test site location. A) Position in the south of The Netherlands. B) At km 34.75 on the southbound track of the railway line Roermond-Sittard. C) Site access from the level crossing *Roermondseweg*.

Table 2.1: Track lay-out and rail profile at the test site.

Rail profile	Curve radius	Cant	Cant deficiency
UIC54E5	1860 m	80 mm	25 mm

Table 2.2: Train traffic that passed the test site during the field test, from 29 March 2021 until 18 Dec 2021. The train traffic is divided into passenger trains, freight trains and other trains.

			Trains [#]	Axles [x10^3]	Cum. load [Mt]	Axle load [Tons]$\pm\sigma$
Measured trains	Passenger	Intercity	15122	320	4.58	14.3 ± 1.4
		Local	9610	64.6	0.877	13.6 ± 1.9
	Freight		1519	124	1.75	14.2 ± 6.6
	Other		142	5.30	0.0608	11.5 ± 5.3
Total measured			26393	515	7.27	14.2 ± 3.6

Table 2.3: Chemical composition (in wt%) and mechanical properties of R370CrHT rail steel as stated on the 3.1-certificate.

	C	Mn	Si	Cr	Re (MPa)	Rm (MPa)	ϵ (%)	Z (%)	Hardness (HV)
R370CrHT	0.81	0.94	0.67	0.503	917	1319	12	42.1	426

Table 2.3 shows the chemical composition and mechanical properties of the R370CrHT steel rail, subject of the current study. The R370CrHT is a fully pearlitic rail steel with chromium addition. The rail has a UIC54E5-stress relief profile [27], which is the common standard for curved track sections in the Dutch railway network. The pearlitic lamella thickness is 80 ± 3 nm [28].

The mechanical properties, determined in a monotonic tensile test as prescribed by the EN13674-1-standard [27], are shown in table 2.3. The ultimate tensile strength, R_m, is defined as the engineering tensile strength. R_e is the 0.2%-offset yield strength. The plastic elongation at fracture, ϵ, is defined as the increase in length of the parallel section of the specimens. The relative area reduction, Z, is calculated from the measured diameter in the necked area. The hardness is determined at the centerline of the rail head after removing 0.5 mm from the surface [27].

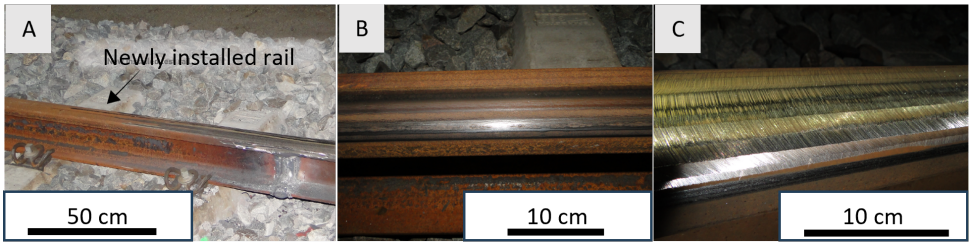

Figure 2.2: Impression of the test site. A) The newly installed rail. B) The rail prior to grinding but after 14 days in service. C) The ground rail surface.

2.2.2. INSPECTIONS AND METALLOGRAPHIC PREPARATIONS

In the present experiment, the in-situ rail grinding was performed as part of the preventive grinding program before the monitoring started. A rail grinder, equipped with 64 grinding wheels for vertical-axis grinding, removed 0.2 mm of material in three passes at a grinding speed of 14 km h^{-1}, which is scheduled every 15 Mt. Before the experiment was completed, no further preventive grinding maintenance was carried out.

Locations for recurring inspections and measurements were marked and numbered. The inspection frequency and the extraction moments of the four rail samples were determined in a reference project. Inspections were carried out during the day, and measurements of surface roughness and hardness at night.

Table 2.4 presents the train load for the four rail samples, each with a length of 3 m. The coding of the samples consists of *rail sample (RS)* combined with the cumulative train load in Mt. A standard portable rail cutter with a 16 inch cutting blade was used to extract the samples. Manual grinding of the weld of the replacement rail was kept short and was marked to avoid mixing with the preventive grinding. The straightness of the running surface was measured to be within regulations, in order to minimize impact loading due to the additional welds in track. In addition, the sample locations were shifted against the direction of travel with increasing test duration, so that the rail surface to be studied examined is passed before the fresh weld.

Hardness measurements and surface roughness measurements on the rail surface were performed to quantify the progress of the contact surface formation. The surface roughness was determined in accordance with the EN-ISO4287 standard [29], using a Mitutoyo SJ210 surftester. The hardness was measured using a Equotip 3 Leeb rebound hardness tester, as described in the ASTM-A956 standard [30]. The resulting Leeb hardness was converted to Vickers hardness according to the ASTM-E140 standard [31]. Pictures of the contact surface were made with a 5 Mpx digital camera.

Metallographic preparations started with a visual inspection of the sample surface. Pictures of the surface were made using the same 5 Mpx camera. Under lab conditions, the surface roughness and hardness were remeasured in agreement with the aforementioned standards at transverse positions A, B, and C, indicated in Figure 2.3. Six connecting measurements were made, covering the characteristic length of the grinding process. Also six hardness measurements were performed, evenly distributed over the same sample length.

Table 2.4: Rail samples (RS) extracted from the test site. The first row presents the rail sample codes, the second row the total load after grinding, and the third row the share of total load (%).

Rail sample	RS0	RS0.4	RS2.0	RS6.9
Total load [Mt]	0	0.43	2.04	6.92
Share of total load [%]	0	6.2	29.5	100

Figure 2.3 shows the transverse and longitudinal micrograph positions for all four rail samples, which were cut after aligning the rail samples with respect to the ground facets and the characteristic length of the grinding pattern. Specimens were extracted from the middle of the facet and from the facet transition zone in the longitudinal direction. Cross-section specimens from the contact surface were cut into three parts to fit the 20 mm mold for specimen mounting.

The specimens were embedded in Struers ClaroCit Acrylic resin and prepared using a Struers MD-piano disc with 9 µm diamond polishing fluid, followed by polishing with 3 and 1 µm diamond polishing fluid. Specimens were etched with 2% Nital for 10 seconds. For optical microscopy a Keyence VHX5000 microscope was used. For detailed observations of the surface and the microstructure a JEOL IT100 Scanning Electron Microscope was used in secondary-electron detection mode with an acceleration voltage of 15 kV and 11 mm working distance.

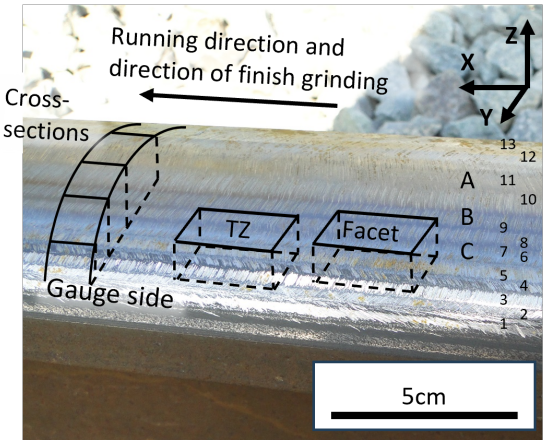

Figure 2.3: Image of the ground in-service rail. At the rail surface are indicated: 1) Visually distinguishable ground facets (1-13). 2) Positions for hardness and surface roughness measurements, A, B, and C. 3) The position of the metallographic sections: sections along the running direction at the facet and at the facet transition zone (TZ), and cross-sections.

2.3. RESULTS

2.3.1. CHARACTERIZATION OF THE FRESH GROUND SURFACE

SURFACE ANALYSIS

Figure 2.4A shows an optical micrograph of the rail surface of RS0 for detailed analysis. The grinding grooves are parallel and typical for vertical-axis grinding, formed transverse to the grinding direction. The average roughness is $R_a = 5.5 \pm 0.2$ µm. The pattern of repeated deeper grinding grooves evidences the characteristic length of the grinding process, which is ~67 mm.

Facets are smaller in the smaller-radius sections of the transverse rail head profile and wider in the larger-radius sections. The average width of the facets is 5±2 mm. Temper colors are an important quality indicator [32]. Blueing of individual grinding grooves is observed in facet 3, indicated with *i* in Figure 2.4A, whereas in facet 12, see *ii*, groups of colored grooves are present. The purple to black surface oxidation in facet 7, see *iii*, is associated with temperatures above 735 °C, indicated as metallographic burn [33]. This burn is accompanied by WEL formation and these temperatures may even result in damage formation due to thermal stress [16, 33, 34].

Figure 2.4B shows a SEM image of the blue-framed area in Figure 2.4A, enclosing the facet transition zone. The width of the zone is ~800 µm and is defined by the variation in grinding groove lengths, as highlighted in the figure.

The deepest grinding grooves cross the transition zone and are often characterized by a different orientation. One such groove is indicated in Figure 2.4C which corresponds to the area enclosed by the red frame in Figure 2.4A.

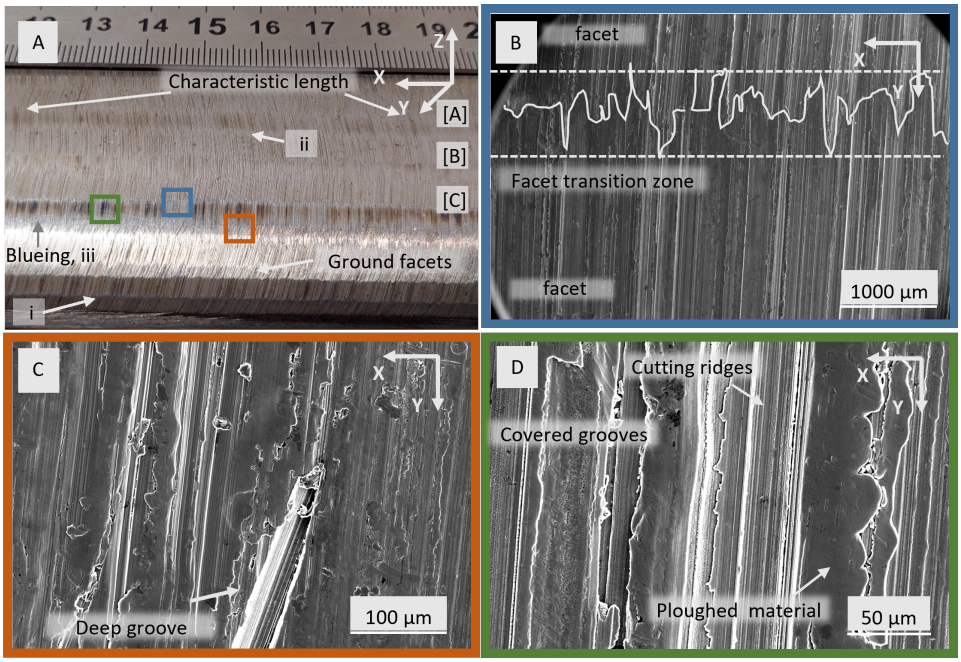

Figure 2.4: Representative micrographs of the ground rail surface of sample RS0. A) Optical micrograph of the ground surface. The measurement positions A-C, the characteristic length of the grinding process, and the various degrees of blueing, see *i-iii*, are indicated. B) Facet transition zone. The extremities of the grinding grooves that define the transition zone are highlighted. C) A grinding groove crossing the facet transition. D) The characteristic grinding groove. Cutting ridges are present in the grinding grooves. At both sides of the groove ploughed material is observed.

Figure 2.4D presents the surface in the green-framed area of Figure 2.4A and it encloses facet 7. Four characteristic features of the grinding grooves on facet 7 are:

- Cutting ridges are present at the bottom of the groove. In machining operations these ridges are associated with tool wear [16] and in grinding with the shape of the cutting face of abrasive particles.
- Parallel grinding grooves, which display a mutual distance of ~80 µm caused by abrasive particles that simultaneously treated the surface.
- Ploughing, which is characteristic for grinding [16] and causes material pile-ups or ploughed ridges. At the $-X$-side, the material is ploughed directly adjacent to the groove, whereas on the opposite side, several smaller frayed layers are present, covering adjacent grinding grooves. The smooth surface texture of the ploughed material is caused by the rubbing of the abrasive particle on the surface.

CROSS-SECTION ANALYSIS

Figure 2.5 shows representative micrographs of RS0 to study the freshly ground surface in more detail. The micrograph in Figure 2.5A is observed transverse to the running direction. It displays the variety of grinding groove profiles resulting from the abrasive particle size variation. The presence and orientation of extruded material in the parallel grinding grooves show a cutting sequence, although the grooves were cut in the same grinding pass.

The same figure shows a detached WEL at the top of the ridges, possibly caused by frictional heat generated in the friction zone of the abrasive particle. Thin WEL is present at the bottom of the groove, resulting from frictional heating in the cutting zone.

Figure 2.5B shows another consequence of the cutting depth variation between abrasive particles. Material is strained instead of cut and removed, and is covering the freshly ground surface.

The observation direction in Figures 2.5C and 2.5D is parallel to the running direction and perpendicular to the grinding grooves. Figure 2.5C shows a material pile-up that results from subsequent passages of different abrasive particles ploughing material to the side. The layers are shifted relative to each other due to different abrasive particle trajectories. The limited deformation below the pile-up, in the $-Y$-direction, evidences their direction of movement. In addition, some layers show evidence of WEL while other layers have remained pearlitic.

Figure 2.5D presents a detailed SEM image taken within the green framed area of Figure 2.5C. The strained pearlite of the middle layer has a ~1 µm thick WEL on both sides which is also present at the interface, see i. The surface layer, see ii, consists of WEL and the interface between the top layer and the pearlite middle layer is frayed. The protrusions seem to have deformed the pearlite microstructure.

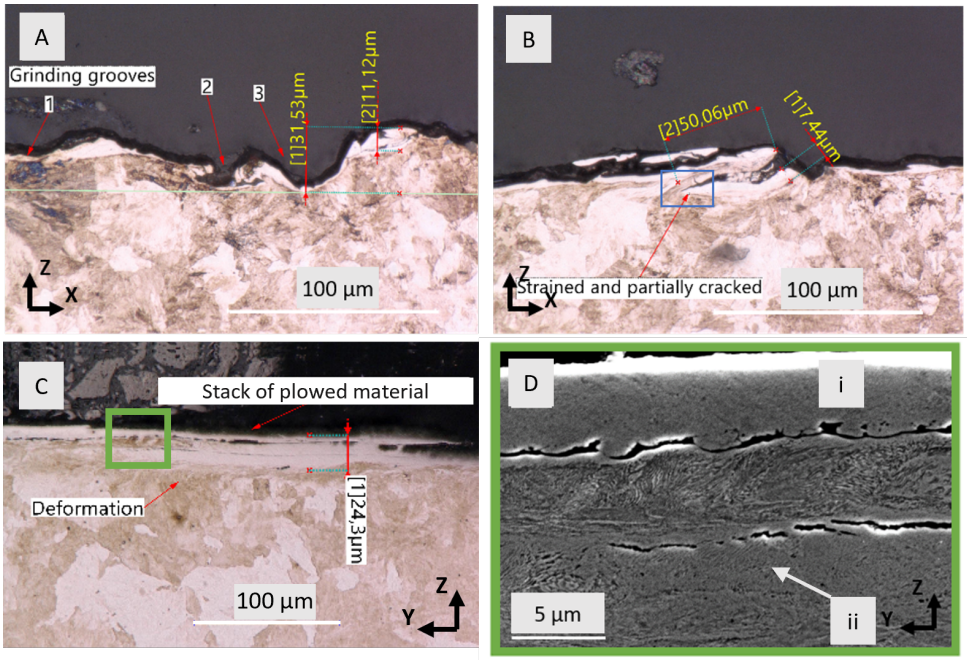

Figure 2.5: The freshly ground rail surface observed in cross-section on metallographic specimens from rail sample RS0. A) Grinding grooves with various shapes, widths, and depths. Grinding groove 1 is shallow and wider compared to grinding groove 2, which is deeper and covered with extruded material. Groove 3 is narrow and the distance to the ridge at the side is R_t ~31 µm. B) Strained and partially cracked material that was not removed and covers the WEL-coated surface. C) A stack of ploughed material. The layers have a total thickness of ~24 µm. Below the layers, the deformation orientation is in the $-Y$-direction. D) The SEM micrograph shows the green framed area in Figure 2.5c in detail. The top layer is phase transformed, see ii. At the bottom, see i, a ~2 µm WEL is observed while the middle layer consists of strained pearlite with a small WEL at both sides.

2.3.2. EVOLUTION OF THE GROUND RAIL DURING THE FIELD TEST

SURFACE EVOLUTION

Daylight inspections in track are performed at six stages of cumulative loading to evaluate the contact surface formation. Results of these inspections are presented in Figure 2.6 for increasing cumulative loads. Wear patterns are interpreted as the qualitative indication for the wheel-contact locations.

Figure 2.6A shows the rail surface after 1×10^{-3} Mt of load. The contact surface is narrow and facet transitions of facet 8, indicated by the arrow, are widening, evidencing localized contact.

In Figure 2.6B the contact surface after 0.12 Mt is presented. The contact has widened and includes facet 9, which can be determined well by the surface corrosion that was worn away. In addition to the contact surfaces on the facet transitions, load-carrying surfaces develop on the facet surface, as evidenced by the surface widening between the brownish grinding grooves.

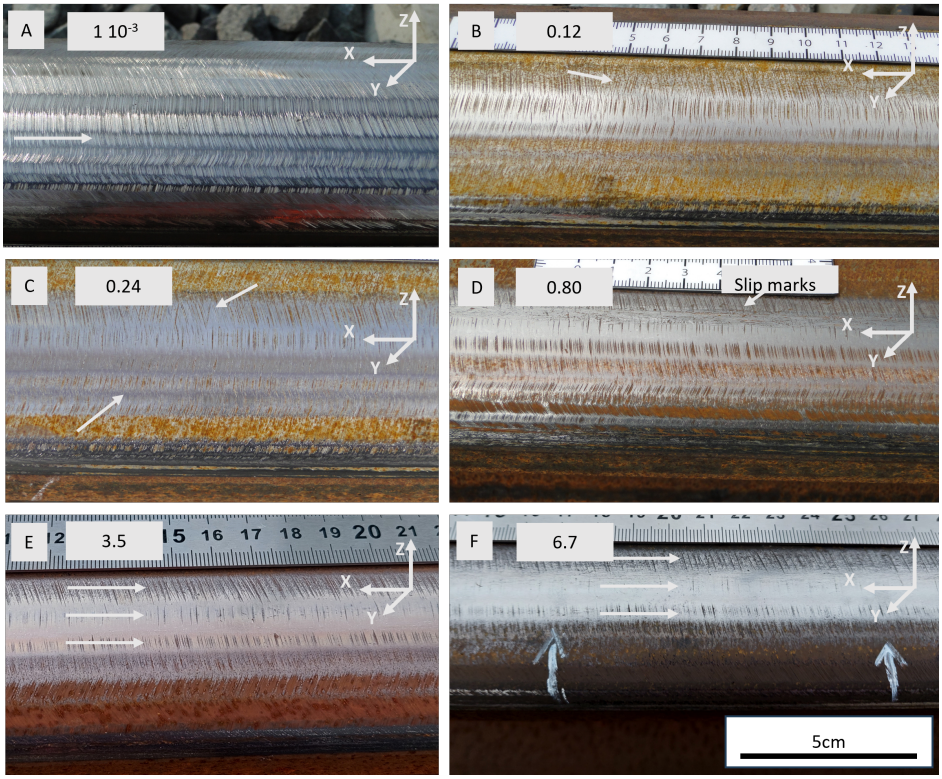

Figure 2.6: The contact-surface formation as a function of the cumulative load, based on rail surface inspections in daylight. The cumulative load in Mt is presented in each micrograph. A) 1×10^{-3} Mt. Contact-surface formation takes place at the facet transitions of facet 8, indicated by the arrow. Blueing is still present. B) 0.12 Mt. Surface corrosion has taken place. The contact surface widens and load-carrying surfaces start to develop between the grinding grooves at the face surface. Grinding grooves with diverging orientations appear. C) 0.24 Mt. The surface of the facet transitions is smooth on the gauge side of the contact zone. Surface corrosion is locally present at the facet surfaces and the grinding grooves with diverging orientation are still present. D) 0.80 Mt. The contact surface width is reached and the corrosion layer has thickened. The length of grinding grooves shortens, but deeper grooves remain. Slip marks at the surface are caused by track maintenance and are not investigated. E) 3.5 Mt. Three arrows are placed to observe the grinding groove lengths and the densities. F) 6.7 Mt. The surface condition just before the field test is completed.

Figure 2.6C shows that the contact width after 0.24 Mt of train load is wider than after 0.12 Mt. At the gauge side of the contact surface the wheel contact is concentrated at the facet transition zones, resulting in smooth and light gray surfaces.

The inspection results in Figures 2.6D-F cover a longer period of time because the development of the contact surface, after the initial stage, occurs more gradually. The figures present the rail surface at 0.80 Mt, 3.5 Mt, and 6.7 Mt of train load, respectively. The contact surface width in Figure 2.6D and in Figure 2.6C is the same from which it is deduced that the contact surface widening that took place during the initial stage of the contact surface formation stopped. The number of grinding grooves on the center of the contact surface decreases and the length shortens. Deep grooves are still present.

In order to compare the length and density of the remaining grinding grooves in Figures 2.6E and 2.6F three arrows are placed at the same longitudinal and transverse positions relative to the characteristic grinding length and the facets, in order to compare the length and density of the remaining grinding grooves. The comparison between the both surface conditions shows that at the middle arrow the length and density of the remaining grinding grooves decrease and some deeper grinding grooves remain. At the positions of both outer arrows, the length of the grinding grooves becomes only slightly shorter and the density remains almost the same.

EVOLUTION OF ROUGHNESS, HARDNESS AND WEAR

Qualitative results of the track inspections are supported by measurements of surface roughness and hardness as shown in Figure 2.7. Figure 2.7A shows that the surface roughness initially reduces at a higher rate at measurement positions B and C. These positions are adjacent to facet 8, which is the facet that is the first to show facet-transition widening in Figure 2.6A. At position A, at the center of the contact surface, the roughness initially decreases at a lower rate but eventually reaches the lowest surface roughness value.

The surface hardness is measured at the same positions A, B, and C to evaluate its development. The highest hardness is expected at positions experiencing the highest contact stresses. The results in Figure 2.7B show that hardening proceeds initially fast at all measurement positions, but the highest hardness value of 431 ± 1 HV is reached, similar to the roughness, at position A.

Figure 2.8 presents surface characteristics of wear mechanisms contributing to the contact-surface formation at the facet transition and at the facet. Figure 2.8A shows the surface of RS0.4. At the facet, load-carrying surfaces were formed between the deeper grinding grooves, indicated with i, and at the facet transition zones virtually no grinding grooves are present, see ii. Figure 2.8B shows the surface at i in detail. The surface is characterized by extruded slivers forming parallel lines. Deformation and sliver formation from roughness asperities is a known mechanism for surface roughness reduction [20, 21]. In the process of sliver formation grinding grooves are covered and filled. The surface at ii, presented in Figure 2.8C, is partially smooth and also similar parallel lines are present. The lines evidence a similar wear mechanism although the surface features may indicate a more advanced state of wear.

Figure 2.8D shows the rail surface of RS6.9, after completion of the field test. A different form of wear has taken place at the surface in the orange-framed area. Wear slivers show serrated edges and have various orientations and lengths in Figure 2.8E. These characteristics are associated with rolling contact fatigue damage initiation [1] rather than with wear tongue formation [35] or ratchetting-based wear [21].

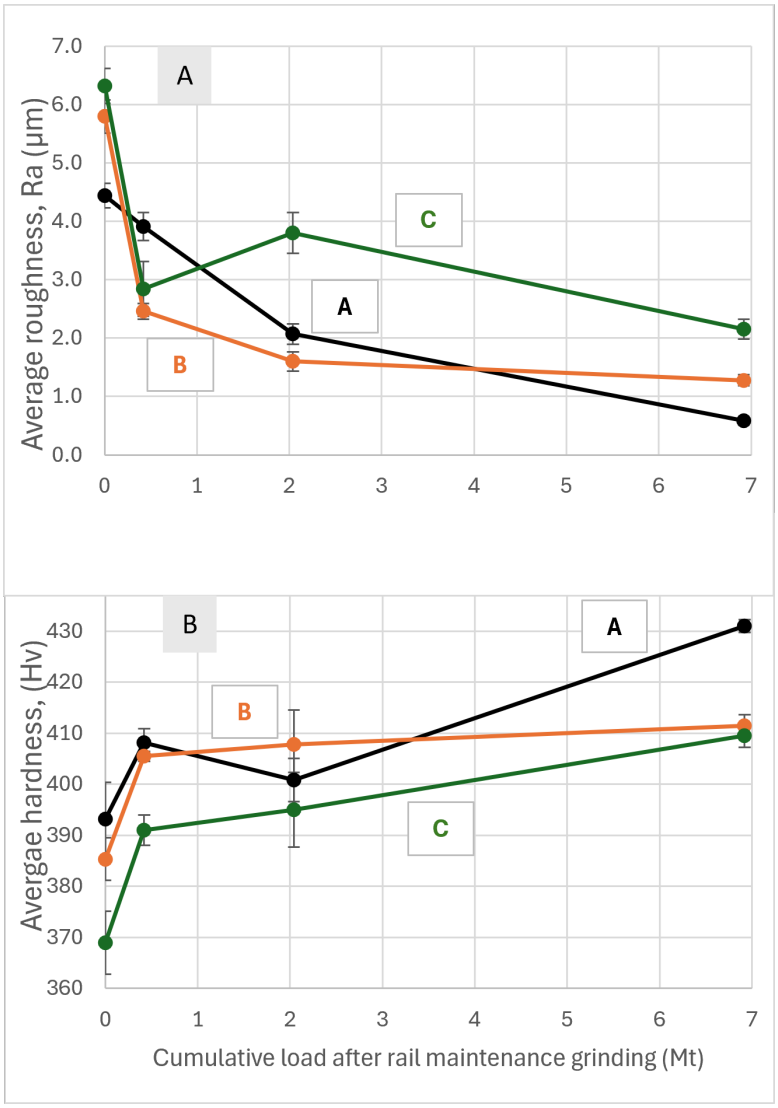

Figure 2.7: The evolution of surface roughness (A) and hardness (B) in positions A, B and C, during the field test. The measurements were made on the surfaces of the extracted rail samples. See Figure 2.3 for the reference of the measurement positions.

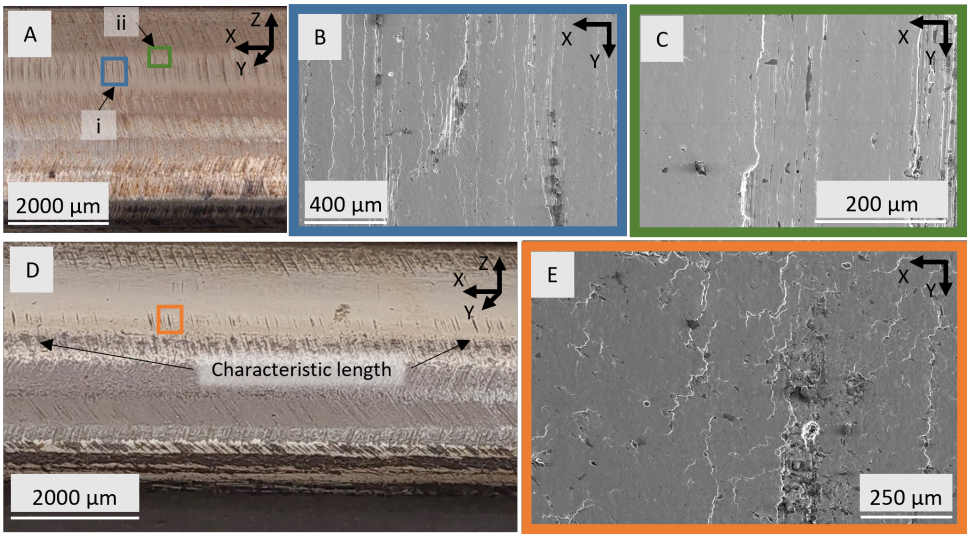

Figure 2.8: The contact surface at rail sample RS0.4, A-C, and rail sample RS6.9, D-E. A) Micrograph of the rail surface. Load-carrying surfaces develop between grinding grooves, see i, and the facet-transition zones are smooth, see ii. B) On the facet surface in the blue frame, vertical lines and partly covered grinding grooves are present. Both are the result of extrusion of roughness asperities. C) Extrusion lines on the surface in the facet-transition zone of the green-framed area. The parallel lines exhibit a lower density. D) Micrograph of the rail surface. The middle of the contact surface is smooth but on both sides the deeper grooves remain. E) The contact surface in the orange-framed area. The serrated edges of the lines on the surface exhibit various orientations and length. These are associated with rolling contact fatigue damage initiation.

MICROSTRUCTURE EVOLUTION

Until this point, the contact-surface formation on the ground rail surface has been analyzed using surface observations only. In Figure 2.9 representative cross-section micrographs of the four rail samples RS0, RS0.4, RS2.0, and RS6.9 are presented in rows, including micrographs from the facet transitions and the facets in separate columns.

The freshly ground surface of RS0 shows, in the transition zone, a detached WEL patch on a relatively smooth surface with only one narrow grinding groove. The WEL shows no evidence of material removal, such as the presence of a groove, and is probably the result of rubbing by an abrasive particle on the surface. The facet surface seems to be formed by multiple abrasive particle contacts producing a roughness profile with various heights. This surface shows clear similarities with the surface presented in Figure 2.5A, despite the different observation position.

Figures 2.9C and 2.9D present the rail surfaces at RS0.4. In the transition zone, the mechanisms that contribute to the rapid formation of the contact surface are explained by three characteristic features. First, material extruded from the asperities covers grinding grooves, see i. Second, WEL formation takes place. The deformation and sharp transition between WEL and the pearlitic microstructure evidence the high temperatures that are reached during extrusion of asperities [36, 37]. WEL is formed on both the extruded slivers and on adjacent areas, see ii. Third, subsurface deformation aligns with the direction of the traction, as highlighted by the dotted line. The deformation reaches

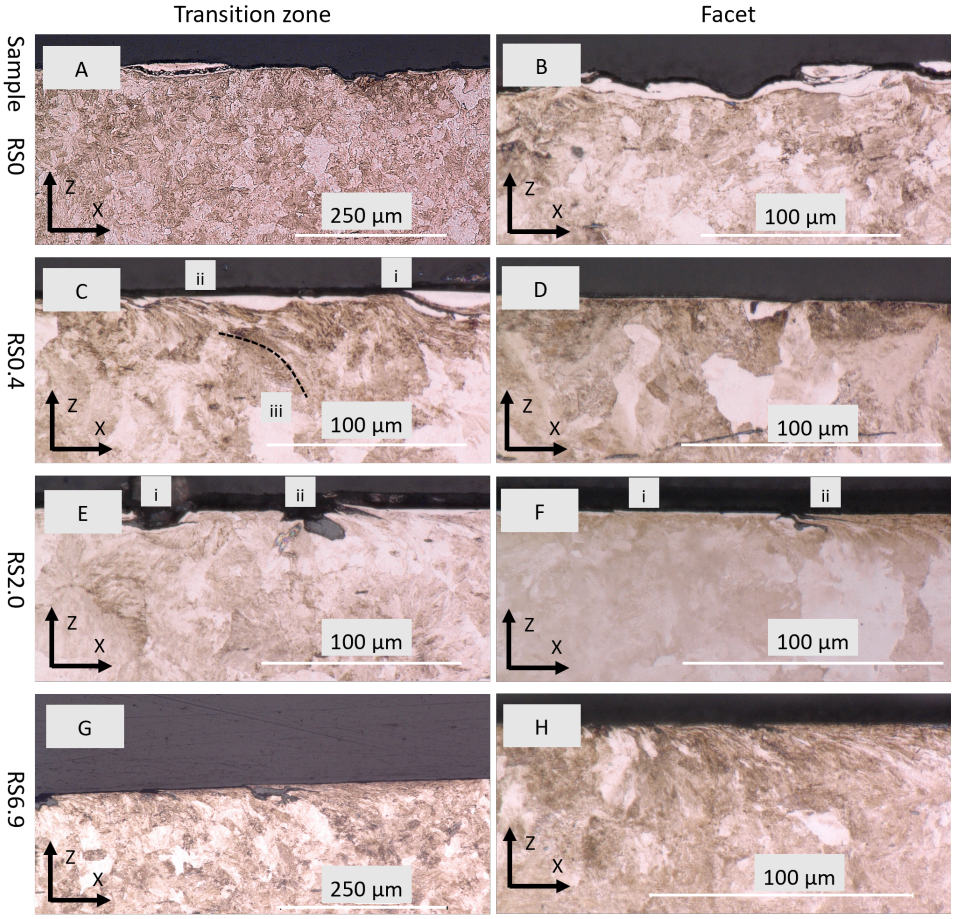

Figure 2.9: The contact surface formation as observed on longitudinal sections. The rows of the array present the micrographs of sections from rail samples RS0 to RS6.9. The columns present the micrographs of sections from the transition zone position on the left and from the middle of the facet on the right. The microstructure details are described in the main text.

a depth of ~60 µm and is only locally present, see *iii*. The facet surface is smooth and slightly wavy. At the facet no deformation or fresh WEL, associated with wheel load and slip, are observed.

Figures 2.9E and 2.9F present the surfaces at sample RS2.0. At the facet-transition zone, the WEL thickness is smaller than that of RS0.4. The residual grinding groove in Figure 2.9E, indicated with *i*, is partly covered with material from both sides. The second grinding groove, see *ii*, is filled with corroded material and damage initiates at the positive X-side. On the surface, next to the damage initation, a fresh WEL has formed. The facet surface in Figure 2.9F shows damage initiation at the extreme of the WEL, indicated with *i*, but the feature of interest is the large damage, see *ii*. A crack starts at the grinding groove bottom, bending downwards, and a parallel crack has initiated. Deformation, both at the surface and also below the surface, is concentrated at the positive X-side of the grinding groove.

Figures 2.9G and 2.9H show the surface and deformation of rail sample RS6.9. The surface conditions at the facet and the transition zone are comparable and only the larger depth of deformation in the transition zone indicates a still slightly higher load.

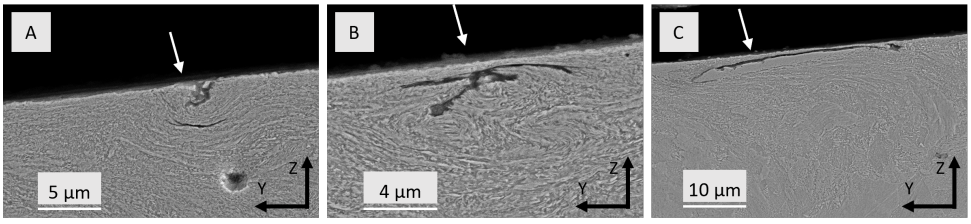

Figure 2.10: The freshly ground surface characteristics affect the contact surface formation, and are related to various features at the surface in rail sample RS6.9. A) Coil-shaped material filling a grinding groove cavity. B) Material extrusion which results in the coverage of a grinding groove. C) Material covering a WEL patch at the running surface.

Figure 2.10 presents micrographs of metallographic cross-sections that were made from RS6.9. The micrographs are presented to show the various ways in which the fresh ground surface characteristics affect the contact surface formation. The observations support the surface observations that some of the ground surface features do not wear quickly. Figure 2.10A shows a grinding groove which is still filled with deformed material. The deformed material shows a coil-like deformation pattern. Kapoor [21] observed comparable patterns of slivers when performing experiments to study the ratcheting-based roughness reduction mechanisms.

At the submerged grinding groove in Figure 2.10B, no sliver formation is observed. It is therefore expected that the extrusion direction is in longitudinal, X-, direction.

Figure 2.10C shows a WEL patch that was formed on the surface by grinding or wheel slip and is now covered. The WEL is ~3 µm thick and ~30 µm wide.

In summary, the main observations on the formation of the contact surface are:

- Initially, the surface roughness at the transition zone exhibits a lower surface roughness than at the facet surface.
- The contact surface formation is assisted by incremental asperity deformation covering grinding grooves. The observations of sliver formation and strain concentration confirm the occurrence of a ratcheting-based wear mechanism, as described by Akagaki and Kato [20] and Kapoor [21].
- Deformation and damage initiation occur mainly at one side of the grinding groove.
- The surface conditions of the facet transition and the facet after the grinding field test are similar.

2.3.3. WEL AND DAMAGE ON THE SURFACE AFTER THE FIELD TEST

WEL CHARACTERIZATION

In studies on the relationship between the durability of the contact surface that is formed and the surface characteristics of the freshly ground surface, WEL is always considered. However, the microstructure of the rail surface deforms as a result of train wheels rolling over it, which can also cause WEL [36]. Therefore, Figure 2.11 presents the pearlitic microstructure and WEL on the freshly ground surface of RS0, Figures 2.11A-C, and on RS6.9, extracted after the field test, Figures 2.11D-F, to indicate specific differences.

Figure 2.11A shows the shallow deformation and deformation orientation in $-Y$-direction, indicated with i, which is caused by grinding forces exerted on the surface by abrasive particles. The rubbing that simultaneously occurs causes a surface temperature rise to A_{C3} and above, facilitating WEL formation, see ii. In the SEM micrograph, shown in Figure 2.11B the WEL thickness is ~5 µm to 10 µm. A similar layer thickness is observed in Figure 2.11C in which the deformation underneath the WEL is highlighted by dotted lines.

Figure 2.11D presents the gauge side of the contact surface of rail sample RS6.9. No WEL is present and below the surface lamellae are strained and deformed having an orientation parallel to that surface.

Figure 2.11E shows the contact surface representative for the central part of the contact surface. Short localized and lens-shaped patches of WEL are present. The clear transition between WEL and the pearlite microstructure evidences a wheel slip-related origination.

Figure 2.11F presents the deformation orientation below the WEL. This deformation orientation is imposed by lateral shear stress in the wheel contact. The deformation, highlighted by dotted lines, is pointing in Y-direction, see i, which is the opposite the observed deformation orientation below the freshly ground surface in Figure 2.11C.

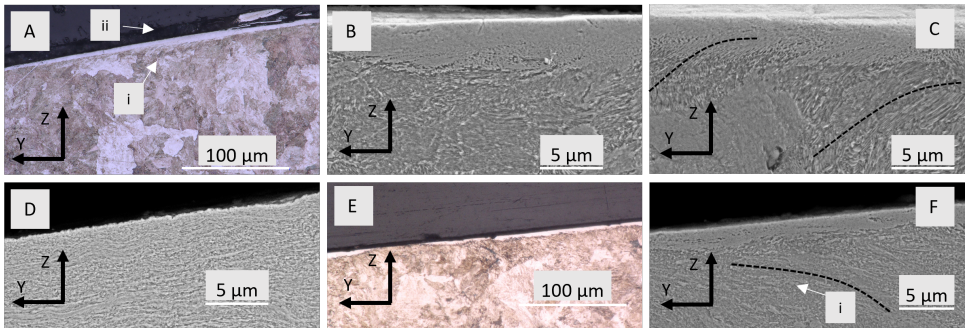

Figure 2.11: Evolution of damage in the facet transition zone of the rail surface. A) RS0.4; the WEL in the grinding groove acts as a boundary for deformation and is submerged. The figure shows a detached WEL caused by grinding, see i. The freshly formed surface is partly embedded by material that has been extruded, see ii. A second extrusion is present which also traps the WEL at the surface. Here the deformation is more evident and a slip related WEL has formed at the surface, see iii. B) RS2.0; damage initiates at the surface. The WEL patch is pressed and embedded into the surface, see i. The crack that forms next to it reached a crack depth of 19 µm and the propagation orientation is 40° with respect to the surface, see ii. C) RS6.9; at the surface two cracks are observed. One crack is present next to the residual grinding groove and is filled corrosion products, see i. The second crack is closed and has a slightly shallower propagation orientation, see ii. The crack depth is ~27 µm and the propagation orientation is 50° with respect to the surface, see iii.

DAMAGE INITIATION

Previous sections showed that, during contact-surface formation, the presence of grinding grooves contributes to inhomogeneous deformation, extrusion of material and damage initiation. Figure 2.12 highlights the evolution of the facet-transition zone surface under increasing cumulative load, evidencing damage initiation. Details of the microstructure, WEL and damage are described in the figure caption.

Figure 2.12A presents the contact surface that was formed at the facet transition zone of rail sample RS0.4. WEL patches are embedded and trapped in the surface, and deformation beneath the surface mainly takes place at the positive X-side of the grinding groove.

Figure 2.12B presents the surface of rail sample RS2.0 to demonstrate the next stage of damage initiation. The surface crack, indicated with ii, is filled with corroded material and the crack faces are open. The crack propagates along the local deformation orientation and shows characteristics of both rolling contact fatigue and wear tongue formation.

Figure 2.12C shows the surface of rail sample RS6.9 with two cracks, indicated with i and ii. Crack i is open and filled with corrosion products, which suggests that it has initiated at a grinding groove. These grinding grooves form an obstacle for deformation, resulting in a locally deformed area. Crack ii, as a result, initiates in the zone of accumulated deformation.

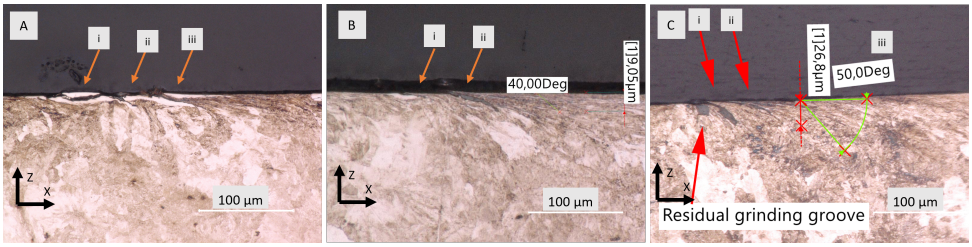

Figure 2.12: Evolution of damage in the facet-transition zone of the rail surface. A) RS0.4; the WEL in the grinding groove acts as a boundary for deformation and is submerged. The figure shows a detached WEL caused by grinding, see i. The freshly formed surface is partly embedded by material that has been extruded, see ii. A second extrusion is present which also traps the WEL at the surface. Here the deformation is more evident and a slip-related WEL has formed at the surface, see iii. B) RS2.0; damage initiates at the surface. The WEL patch is pressed and embedded into the surface, see i. The crack that forms next to it reached a crack depth of 19 µm and the propagation orientation is 40° with respect to the surface, see ii. C) RS6.9; at the surface two cracks are observed. One crack is present next to the residual grinding groove and is filled with corrosion products, see i. The second crack is closed and has a slightly shallower propagation orientation, see ii. The crack depth is ~27 µm and the propagation orientation is 50° with respect to the sruface, see iii.

2.4. DISCUSSION

The formation of the contact surface formation on the freshly ground rail surface is studied under actual operating conditions. The inspections of the surface deliver valuable insights into the wear mechanisms and damage formation that take place.

2.4.1. THE FACET TRANSITION ZONES

Figure 2.4a presents the freshly ground rail surface and Figure 2.4B shows that the facets are connected by transition zones. During grinding with vertical-axis grinding systems, facets are formed on the rail surface that together approximate the contour of the rail head. The angle between the facets depends on the position on the head of the rail and is sharper at small radius sections and more obtuse at the top of the rail. This geometric deviation from the continuous rail contour causes contact stress concentrations at the transition zones which is, in the literature, indicated as a cause of damage initiation [13, 15].

In this study it is observed that a contact surface is formed on the facet transition zones as soon as wheel-rail contact takes place, see Figure 2.6A. As the contact surface widens and extends over multiple facets, the contact surface forms first at the transition zones of the facets added to the contact, see Figure 2.6C. This contact surface-formation is faster at the transition zone compared to the facet itself because of the presence of locally high contact stresses and the local surface characteristics. These surface characteristics are determined by the grinding pattern whereby less material is removed in the transition zones than on the facet. Two aspects of rail grinding will be discussed briefly.

First, for all grinding process parameters being the same, a lower grinding depth results in a lower roughness height [16, 38]. From analyses made by Kalpakjian, Schmid and Vijay Sekar [16] and Koshal [38] the following indicative relation between surface roughness, R_a, and grinding depth a_e was derived:

$$R_a \sim \frac{1}{4}(a_e)^{1/4}. \tag{2.1}$$

Second, the grinding pattern results in a lower metal removal at the facet transitions compared the the facet itself. Kalousek et al. [8] presented a grinding pattern for efficient material removal using vertical-axis grinding which are optimized using advanced simulation software [9]. The first grinding wheel forms a facet and each subsequent grinding wheel passage is then shifted and, as a consequence of limited angular shift, a part of the previously formed facet is removed. As a result, the metal removal approaches zero at the side of the facet, forming the transition. By changing the inclination of the grinding motors, the differences in grinding depth between the facet and the facet transition are further increased, improving the grinding effectiveness and preventing the formation of circular grinding patterns on the rail surface.

The grinding pattern applied in the current study resulted in the presence of 13 observable facets on the final surface, as shown in Figure 2.1, although in the grinding design even more facets are identified. The large number of facets requires a small grinding depth and results in even lower removal, and hence lower roughness, in the transition zones.

2.4.2. WEAR TRANSITION

The observations of the contact surface in Figures 2.8 and 2.9 show that the wear mechanism directly after grinding is ratcheting-based. Ratchetting is the repetitive loading of the material above the yield limit [21], resulting in localized deformation and eventually to failure.

Ratchetting-based wear models of rough surfaces successively describe asperity deformation, sliver formation, and sliver separation [21]. The practical applicability of these wear models can be tested experimentally by moving a hard slider over a softer surface, demonstrating the formation of parallel slivers from parallel asperities [20, 39]. Akagaki and Kato [20] named this process of sliver formation 'flow wear'. The thin surface layers are progressively compressed and extruded, which is caused by contact stress concentration at the contact extremes [21].

Figures 2.8B and C present the surface of RS0.4 evidencing the ratchetting-based wear. The parallel extruded slivers exhibit small mutual distances corresponding with the distances of the grinding grooves shown in Figure 2.4D. Figure 2.9C shows a micrograph of a facet transition of RS0.4. The slivers that are formed by extrusion cover and fill valleys in the ground surface, accelerating the reduction of the roughness. The direction of extrusion is determined by the tractive shear stresses that point in the $-X$-direction.

Figure 2.8E shows the surface condition of RS6.9. The parallel slivers at the surface that were visible in RS0.4 are replaced by serrated lines and rolling contact fatigue (RCF) damage initiation has taken place.

When the contact surface is formed and the grinding roughness is removed, the wear rate becomes lower [40]. For a low wear mechanism like delamination wear to occur, platelets must be formed and removed from the rail surface. A process of void coalescence close to the surface has to take place, facilitating the detachment of the platelet [41]. For the formation of wear platelets a small crack propagation angle with respect

to the surface is required, along with a tendency to develop upward branching cracks to cause detachment [1, 42]. In contrast, RCF cracks tend to grow deep.

Wang et al. [1] performed two-disc experiments on eutectoid rail steel, applying a representative Hertz contact stress of 1161 MPa and slip ratios between 0.5% and 5% and found that crack growth exceeds the wear rate, independent of the slip ratio. They observed similar serrated lines at the surface which were ranked from 'coherent peeling' to 'tiny cracks' [1].

The expected wheel slip ratio at the railway steel in the test section is applied at the bottom of the slip range by Wang [1]. The surface condition as presented in Figure 2.8E shows the best fit with the 1% slip ratio of the eutectoid rail steel surface.

2.4.3. WEL FORMATION AND DEFORMATION

In this work we propose a 5-stage wear model of the ground surface that captures the interactions between asperity deformation, WEL formation and the embedding of characteristic surface features, wear and damage initiation which is based on the observations in this experiment. Figures 2.5A, 4.1C and 2.12 each show a portion of the overall development of the rail surface.

Figure 2.13 shows this schematic model for a simplified ground surface consisting of a representative single grinding groove and the adjacent surface. Figure 2.13A presents the freshly ground surface. Material removal caused a groove with ploughed ridges at both sides. The friction in the cutting zone caused heat generation resulting in a WEL at the bottom and at both sides, as well as the extrusion of material.

Figure 2.13B represents the second stage. The majority of extruded slivers and semi-detached WEL patches are fractured and removed from the surface.

In Figure 2.13C the load-carrying surface starts to form. Material is extruded, embedding ground surface features in the surface and the surface roughness is strongly reduced. The material extrusion causes strain concentration at one side of the grinding groove. At the extruded material fresh WEL is formed. WEL, present at the surface of the grinding groove, spalls off from the deformed side but stays attached on the opposite side. During this stage the grinding groove starts to align with the deformation orientation.

Figure 2.13D shows that, with the progress of the contact-surface formation, the reappeared WEL becomes thinner or is even worn off. The grinding groove, under ongoing deformation, is closed at this stage, resulting in flanks pressed together with the embedded WEL in between. Exposure to the elements causes the embedded WEL to corrode.

Figure 2.13E shows the last wear stage. Wear processes at the surface have reduced the number of submerged grinding grooves, but the deepest grinding grooves still remain. Thin WEL reappears at the surface and damage initiates at the bottom of the deformed grinding groove and in the deformed material next to it.

The presented schematic model provides a comprehensive qualitative overview covering the characteristics of the freshly ground surface, the roughness reduction mechanisms and preferential damage initiation sites. Nevertheless, more research is needed to quantify the interrelation between the observed grinding groove characteristics and damage initiation.

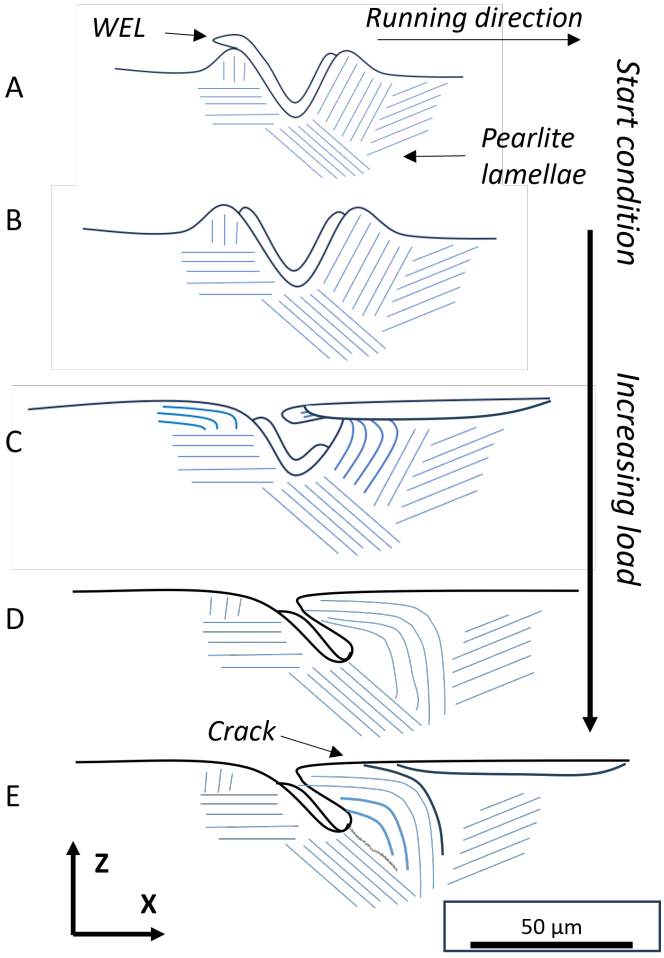

Figure 2.13: Schematic model describing roughness reduction and WEL removal, re-appearance and submerging of the freshly ground surface.

2.5. CONCLUSIONS

A field test is performed to study the characteristics of the freshly ground rail surface, wear and deformation processes, and to define critical aspects for the durability of the resulting contact surface. From the observations the following conclusions are drawn.

- The vertical-axis grinding forms facets at the rail profile. The width of the transition zones, between facets is defined by the variation in grinding groove length. The contact stress at these facet transitions is initially high as a result of the rail head geometry. When the facet-transition zones are worn away, the surface and the subsurface deformation become similar for facets and facet transition zones.

- A ratchetting-based wear mechanism contributes to the reduction of the surface roughness. Material from roughness asperities is extruded out of the contact, covers deeper grinding grooves and contributes to the fast formation of load-carrying surfaces. This wear mechanism is gradually replaced and crack initiation and propagation related to rolling contact fatigue starts to outgrow the wear.

- White etching layers (WEL) are present in the grinding grooves after grinding. WEL tend, as a result of deformation, to spall off but the remaining WELs are submerged and enclosed in the surface.

- A schematic wear model is proposed to capture the observed interactions between deformation, white etching layers (WEL) formation and the embedding of ground surface features. After grinding WEL are present in the grinding grooves. First, spallation of extruded and phase-transformed material takes place. Subsequently crushing and submerging of grinding grooves occurs which is accompanied by the reappearance of WEL. Deeper grooves act as obstacles and prevent uniform deformation from occurring. Damage initiates adjacent to these grinding grooves in the zone with strain concentration.

- The study shows that deep grinding grooves introduce the risk of damage initiation from the ground surface. Deep grinding grooves are associated with high grinding depth, deformation, and burn. Depth variation in the grinding grooves is an inevitable characteristic of rail grinding. Despite the characteristic variations, deep grinding grooves should be avoided or fully removed by finishing passes. An acceptable depth seems to be defined by the material removal by wear during the formation of the contact surface.

BIBLIOGRAPHY

[1] H.H. Wang et al. “Wear and rolling contact fatigue competition mechanism of different types of rail steels under various slip ratios”. In: *Wear* 522 (June 2023). ISSN: 00431648. DOI: 10.1016/j.wear.2023.204721.

[2] J.E. Garnham and C.L. Davis. “Very early stage rolling contact fatigue crack growth in pearlitic rail steels”. In: *Wear* 271.1-2 (May 2011), pp. 100–112. ISSN: 00431648. DOI: 10.1016/j.wear.2010.10.004.

[3] E. Magel, J. Kalousek, and P. Sroba. “Chasing the magic wear rate”. In: *Civil-Comp Proceedings*. Vol. 104. Civil-Comp Press, 2014. DOI: 10.4203/ccp.104.116.

[4] E. Magel et al. “The blending of theory and practice in modern rail grinding”. In: *Fatigue and Fracture of Engineering Materials and Structures* 26.10 (2003), pp. 921–929. ISSN: 8756758X. DOI: 10.1046/j.1460-2695.2003.00669.x.

[5] R. de Vries, P. Sroba, and E. Magel. “Preventive Grinding Moves into the 21 st Century on Canadian Pacific Railway”. In: *Proceedings from the AREMA Annual Conference, Chicago, IL*. 2001.

[6] P. Sroba and M. Roney. *Rail grinding best practices*. Tech. rep. National research council of Canada, 2003.

[7] E.E. Magel and J. Kalousek. “The application of contact mechanics to rail profile design and rail grinding”. In: *Wear* 253 (2002), pp. 308–316.

[8] J. Kalousek, P. Sroba, and C. Hegelund. “Analysis of rail grinding tests and implications for corrective and preventative grinding”. In: *Fourth International Heavy Haul Railway Conference 1989: Railways in Action*. 1989, pp. 193–204.

[9] Q. Lin et al. “Optimal design of rail grinding patterns based on a rail grinding target profile”. In: *Proceedings of the Institution of Mechanical Engineers, Part F: Journal of Rail and Rapid Transit* 232.2 (Feb. 2018), pp. 560–571. ISSN: 20413017. DOI: 10.1177/0954409716679447.

[10] S.L. Grassie et al. “Studs: a squat-type defect in rails”. In: *Proceedings of the Institution of Mechanical Engineers, Part F: Journal of Rail and Rapid Transit* 226.3 (2011), pp. 243–256. ISSN: 0954-4097 2041-3017. DOI: 10.1177/0954409711421462.

[11] M. Steenbergen. “Rolling contact fatigue in relation to rail grinding”. In: *Wear* 356-357 (June 2016), pp. 110–121. ISSN: 00431648. DOI: 10.1016/j.wear.2016.03.015.

[12] C.J. Rasmussen et al. “Surface crack formation on rails at grinding induced martensite white etching layers”. In: *Wear* 384-385 (Aug. 2017), pp. 8–14. ISSN: 00431648. DOI: 10.1016/j.wear.2017.04.014.

[13] F. Fau et al. “Effect of grinding quality, lubrication quality and rail hardness on flaking defect initiation on high rails”. In: *Proc. 10 th Int. Conf. Contact Mech. Wear Rail/Wheel Systems CM2015, Colorado, USA*. Vol. 30. 2015.

[14] M. Mesaritis et al. “A laboratory demonstration of rail grinding and analysis of running roughness and wear”. In: *Wear* 456-457 (Sept. 2020). ISSN: 00431648. DOI: 10.1016/j.wear.2020.203379.

[15] M. Mesaritis et al. “Post-field grinding evaluation of different rail grades in full-scale wheel/rail laboratory tests”. In: *Tribology International* 177 (Jan. 2023). ISSN: 0301679X. DOI: 10.1016/j.triboint.2022.107980.

[16] S. Kalpakjian, S.R. Schmid, and K.S. Vijay Sekar. *Manufacturing Engineering and Technology*. 7th SI Edition. Pearson, 2014, pp. 1–1224. ISBN: 9780133128741.

[17] Z.B. Hou and R. Komanduri. “On the mechanics of the grinding process - Part I. Stochastic nature of the grinding process”. In: *International Journal of Machine Tools and Manufacture* 43.15 (Dec. 2003), pp. 1579–1593. ISSN: 08906955. DOI: 10.1016/S0890-6955(03)00186-X.

[18] K. Kato. “Abrasive wear of metals”. In: *Tribology International* 30.5 (1997), pp. 333–338. ISSN: 0301-679X. DOI: https://doi.org/10.1016/S0301-679X(96)00063-1. URL: https://www.sciencedirect.com/science/article/pii/S0301679X96000631.

[19] P.J. Blau. “On the nature of running-in”. In: *Tribology International* 38.11-12 (2005), pp. 1007–1012. ISSN: 0301679X. DOI: 10.1016/j.triboint.2005.07.020.

[20] T. Akagaki and K. Kato. “Plastic flow process of surface layers in flow wear under boundary lubricated conditions”. In: *Wear* 117.2 (June 1987), pp. 179–196. ISSN: 00431648. DOI: 10.1016/0043-1648(87)90254-7.

[21] A. Kapoor. “Wear by plastic ratchetting”. In: *Wear* 212.1 (Nov. 1997), pp. 119–130. ISSN: 00431648. DOI: 10.1016/S0043-1648(97)00083-5.

[22] A. Kapoor et al. “Surface roughness and plastic flow in rail wheel contact”. In: *Wear* 253 (2002), pp. 257–264.

[23] V. Mattos Ferreira et al. “Microstructure development of pearlitic railway steels subjected to fast heating”. In: *Materials and Design* 221 (Sept. 2022). ISSN: 18734197. DOI: 10.1016/j.matdes.2022.110989.

[24] S. Malkin and C. Guo. “Thermal Analysis of Grinding”. In: *CIRP Annals* 56.2 (2007), pp. 760–782. ISSN: 00078506. DOI: 10.1016/j.cirp.2007.10.005.

[25] M. Steenbergen. “Squat formation and rolling contact fatigue in curved rail track”. In: *Engineering Fracture Mechanics* 143 (2015), pp. 80–96. ISSN: 00137944. DOI: 10.1016/j.engfracmech.2015.05.060.

[26] A.D. Bedoya-Zapata et al. “White Etching Layer (WEL) formation in different rail grades after grinding operations in the field”. In: *Wear* 502-503 (Aug. 2022). ISSN: 00431648. DOI: 10.1016/j.wear.2022.204371.

[27] CEN. *prEN13674-1 - Railway applications - Rail - Part 1: Vignole railway rails 46 kg/m and above*. European Committee for Standardization, 2023, pp. 1–112.

[28] S. Maya-Johnson, A.J. Ramirez, and A. Toro. "Fatigue crack growth rate of two pearlitic rail steels". In: *Engineering Fracture Mechanics* 138 (Apr. 2015), pp. 63–72. ISSN: 00137944. DOI: 10.1016/j.engfracmech.2015.03.023.

[29] CEN. *ISO4287:1997 - Geometrical Product Specification - Surface texture: Profile method - Terms, definitions and surface texture parameters*. 1997.

[30] ASTM. *A956 Standard Test Method for Leeb Hardness Testing of Steel Products*. American Society of Testing Materials, 2022.

[31] ASTM. *E140-12B Standard Hardness Conversion Tables for Metals Relationship Among Brinell Hardness, Vickers Hardness, Rockwell Hardness, Superficial Hardness, Knoop Hardness, Scleroscope Hardness, and Leeb Hardness*. Vol. 03.01. 2019.

[32] CEN. *EN13231-2 - Railway application - Track - Acceptance of works - Part 2: Acceptance of reprofiling rails in plain line, switches, crossings and expansion devices*. 2020.

[33] B. Lin et al. "Influence of grinding parameters on surface temperature and burn behaviors of grinding rail". In: *Tribology International* 122 (June 2018), pp. 151–162. ISSN: 0301679X. DOI: 10.1016/j.triboint.2018.02.017.

[34] J. Wu et al. "Micro and Nanoscale Characterization of Complex Multilayer-Structured White Etching Layer in Rails". In: *Metals* 8.10 (Sept. 2018), p. 749. ISSN: 2075-4701. DOI: 10.3390/met8100749.

[35] G. Zhou et al. "Fatigue damage mechanism of railway wheels under lateral forces". In: *Tribology International* 91 (July 2015), pp. 160–169. ISSN: 0301679X. DOI: 10.1016/j.triboint.2015.07.008.

[36] R. Pan et al. "Investigation into the microstructure evolution and damage on rail at curved tracks". In: *Wear* 504-505 (Sept. 2022). ISSN: 00431648. DOI: 10.1016/j.wear.2022.204420.

[37] M. Steenbergen and R. Dollevoet. "On the mechanism of squat formation on train rails - Part I: Origination". In: *International Journal of Fatigue* 47 (Feb. 2013), pp. 361–372. ISSN: 01421123. DOI: 10.1016/j.ijfatigue.2012.04.023.

[38] D. Koshal. *Manufacturing engineer's reference book*. Elsevier, 2014.

[39] A.C.F. Cocks and A.R.S. Ponter. "The plastic behaviour of components subjected to constant primary stresses and cyclic secondary strains". In: *The Journal of Strain Analysis for Engineering Design* 20.1 (1985), pp. 7–14. DOI: 10.1243/03093247V201007. URL: https://doi.org/10.1243/03093247V201007.

[40] P.J. Blau. "Mechanisms for transitional friction and wear behavior of sliding metals". In: *Wear* 72.1 (1981), pp. 55–66. ISSN: 0043-1648. DOI: https://doi.org/10.1016/0043-1648(81)90283-0. URL: https://www.sciencedirect.com/science/article/pii/0043164881902830.

[41] N.P. Suh. "The delamination theory of wear". In: *Wear* 25 (1973), pp. 111–124.

[42] D. Zapata, J. Jaramillo, and A. Toro. "Rolling contact and adhesive wear of bainitic and pearlitic steels in low load regime". In: *Wear* 271.1-2 (May 2011), pp. 393–399. ISSN: 00431648. DOI: 10.1016/j.wear.2010.10.009.

3

MICROSTRUCTURE EVOLUTION AND DAMAGE DEVELOPMENT IN THE RAILS OF A SINGLE-TRACK RAILWAY LINE AFTER PREVENTIVE GRINDING

In sparsely populated areas single-track railway lines are still common. Despite the low-density traffic and low axle loads, rail damage is observed to initiate in the rails of these lines. Not only large cracks requiring repair are found, but also newly initiated, post-grinding damage is observed. Rail specimens from the track containing representative damages are extracted to identify the reasons for the damage initiation in the R260Mn steel rail. At the rail surface, three years after the preventive grinding maintenance, the characteristic grinding facets and roughness patterns are still present. White etching layers are observed to surround the residual grinding grooves, maintaining the roughness as a result of the high wear resistance of these layers. The strain orientation at the gauge side of the rail is uni-directional due to lateral creep in the wheel-rail contact while in the center of the contact surface the strain patterns evidence shear stress reversal, associated with the bi-directional traffic. The damage initiation mechanism after preventive grinding is associated with low-wear conditions and stresses concentrated around long-lasting grinding grooves. The findings show that preventive grinding maintenance specifications for regional single-stock railway lines must be improved. Specific points of interest are stringent requirements on the number of facets and surface roughness, as well as directions for the removal of corrugation.

This chapter is based on: B. Schotsman, J. Huisman, M.J. Santofimia, R.H. Petrov, J. Sietsma, "Microstructure evolution and damage development in the rails of a single-track railway line after preventive grinding", Wear, Volumes 576-577, 2025, 206101, ISSN 0043-1648, https://doi.org/10.1016/j.wear.2025.206101.

3.1. INTRODUCTION

In sparsely populated areas single-track railway lines between small towns are still common. Trains run in both directions using the same railway track, and pass each other only at larger train stations along the line, see Figure 3.1. The service is provided by regional companies and the timetable is simple with one or two trains per direction each hour. The typical single-stock service is operated with light trains designed to meet the travelers' specific local needs. Under these use-conditions the rail wear is low and, as a result, the rail service life long. Despite the low annual track load, damages are detected in the railway rails which require additional rail maintenance and rail replacements. In the following, the available literature on the characteristics of bi-directional use, the resulting wear rate, and the required preventive grinding maintenance on single-track railway lines are discussed with respect to deformation, damage initiation and propagation under the specific loading conditions.

Figure 3.1: Impression of the, non-electrified, single track railway line, Zutphen - Hengelo.

In the microstructure of the in-service railway rails three zones can be identified. At the surface, to a depth of 50 µm to 150 µm, the plastic deformation is the most severe [1]. Below this zone, the lamellar structure of the pearlitic rail steels is still recognizable and uni-directionally sheared. The angle between the sheared lamellae and the surface is an indication of the deformation severity [2]. At the center of the running surface of the rail the lamellae can even be parallel to that surface [3]. The depth of the region with measurable increase in hardness can vary from 4 mm to 10 mm beneath the rail surface [1, 3], which is deeper than the observable deformation. This depth shifts with increasing contact widths [4, 5].

Cracks initiated at the surface initially follow the uni-directionally sheared lamellae structure [6]. Simon et al. [7] observed that, within the contact surface, the deformation orientation is not uniformly distributed, introducing new crack-initiation locations.

Under bi-directional use conditions the tangential shear forces exerted on a rail, defining the direction of deformation, are frequently reversed. Tyfour and Beynon [8] and Zeng et al. [9] have shown, in twin disc experiments on pearlitic steels, that reversal starts a process of microstructural re-orientation. The uni-directionally deformed lamellae align with the new shear stress orientation. This process gradually progresses from the surface downwards as the number of revolutions increases. Tyfour and Beynon [10] further showed that cracks, if present, branch after the reversal and realign to the new shear stress orientation.

Rail surface wear is characteristic for railway operations and contributes to the removal of rail damages [11]. On tangent railway tracks the rail wear is already low but Tyfour and Beynon [8] and Zeng et al. [9] observed that frequent rolling direction reversal reduces wear even further. The wear rate drops after the reversal of the tangential shear stress direction and returns to its former rate when the microstructural re-orientation is completed.

Grinding of rails was introduced to re-profile the rail head and correct corrugation wear, already in the 1980s [12]. Nowadays repetitive preventive grinding is a standard maintenance activity and a measure to prevent rolling contact fatigue damage to propagate [13, 14]. Rail grinding is regulated by the EN13231-2-standard [15].

The initially continuous rail head contour is approximated by facets after grinding and these facets are defined by grinding grooves perpendicular to the running direction. Both are characteristic of the modern grinding systems with vertical axis orientation of the grinding motors.

The specific energy in grinding is high, compared to other machining operations [16]. Approximately 50% of the input energy is converted to heat during rubbing of the abrasive particles on the surface [17, 18]. Surface temperatures will rise above the A_{C3}-temperature, the temperature above which full austenitisation of the microstructure takes place. White etching layer (WEL) is formed during cooling with the rail acting as a heat sink. With the increase in material removal during grinding, and thus the contact pressure of the grinding wheel, the WEL thickness increases [19, 20]. The typical hardness of WEL is 2 to 3 times higher than the bulk hardness of the rail steel [21].

Despite the benefits of preventive grinding, the ground surface condition itself may contain defect initiation sites. First, the ground facets are geometric deviations on the rail head. Mesaritis et al. [22], using a full-scale test rig, observed flaking defects to initiate at the facet transition zone. Fau et al. [23] observed discrete flaking to initiate from deep grinding grooves at the facet transition zones. Second, the WEL formation results in hard and brittle patches at the rail surface. Cracks in the WEL layer, damage between WEL and the bulk material [24, 25], and WEL stripes that result from singular abrasive particle contact [26] are reported to act as defect initiation sites.

Grinding is not the only cause of WEL formation. It also arises from regular train operations and can take place at the running surface of the rail [27, 28]. Sometimes WEL is present together with a brown etching layer (BEL). BEL is observed between the surface WEL and the bulk material or can be directly present at the surface [29]. There is not yet a common view on the mechanism of origin, and different mechanisms are proposed in the literature [30, 31, 32]. Mattos Ferreira [33] concluded, after performing laser heat treatment experiments, that BEL originates from WEL. The BEL is formed by tempering of WEL during successive heating cycles with lower heat penetration. The different stages of microstructure development in BEL and the hardness over depth are strong indicators for this. The BEL hardness is lower than that of WEL but still 1.5-2 times as high as the bulk hardness [30].

To summarize, the current research interest is on the resulting surface condition after high-powered rail grinding and the effect of the increased grinding frequency on the rail service life. The ground surface may contain potential defect initiation sites [23, 26, 34, 35] and well-founded limit values for surface deviations are currently lacking.

This work presents reasons for damage initiation in rails of single-track railway lines subjected to low-frequency, bi-directional traffic after investigating representative rail samples from the single-track railway line Zutphen-Hengelo, in The Netherlands. The surface condition and microstructure of the R260Mn standard-grade rail steel used in that railway line, are analyzed, and the contribution of preventive grinding to the occurrence of surface-initiated damage is considered. This study will add new insight to the discussion on preventive rail grinding design and the critical aspects of the resulting surface, especially for regional single-stock and bi-directional loading conditions.

3.2. MATERIALS AND METHODS

3.2.1. MATERIALS

The railway line is a 40 km single-track line, consisting of long tangent track sections and designed to be further developed into a main line, which never happened. The rails are annually inspected to detect rolling contact fatigue damage, to plan corrective maintenance and the necessary renewals. Several locations with rail damage were selected from the inspection reports, and, after day-light inspections, two sections containing representative surface-breaking defects of various sizes, were extracted for this study.

The standard grade R260Mn steel rail used in the line was produced in the Hayange rolling mill in 1992, as was shown by the branding marks on the rail profile. Table 3.1 shows the chemical composition ranges and mechanical properties from the EN13674-1-standard [36]. The actual carbon content is 0.62 wt.% which is measured using a LECO chemical analyzer. The bulk hardness is 278 ± 8 HV1.

Table 3.2 shows the traffic data that measured using a weighing-in-motion unit on the railway line with 3% measurement accuracy on the single-axle-level. The annual cumulative tonnage is ~1.75 Mt and the line is yearly used by 23540 trains with 157126 axles in total.

The single-stock passenger trains are Alstom LINT 41/H trains which run at 130 km h^{-1} and are equally distributed over both running directions. The average axle load of these light vehicles is 10.9 ± 0.6 tons.

The line is also used by a limited number of freight trains. In the direction of Zutphen the locomotives, with a typical axle load of 22 t, pull freight wagons and return empty, as can be concluded from the axle load data presented in Table 3.2. The freight trains account for only 0.7% of the total number of trains, but due to their length and high axle loads they contribute with 6.5% and 2.3% to the total annual line load, in the respective directions of travel.

Table 3.1: Chemical composition ranges (wt.%) and mechanical properties of R260Mn rail steel, as stated in the EN13674-1-standard [36]

Chemical composition						Mechanical properties		
C	Si	Mn	P	S	Cr	σ_{UTS} (MPa)	ε (%)	Hardness (HBW)
0.53-0.77	0.13-0.62	1.25-1.75	≤0.025	≤0.030	≤0.15	880	10	275-320

Table 3.2: Total trains and line load divided into running direction and freight and passenger trains. Measurement period: 10 Sept 2019 - 9 Sept 2020

Direction		Trains (#)	Axles (#)	Cum. load (kTons)	Axle load Tons($\overline{x}\pm\sigma$)
Hengelo	Passenger	11608	73310	797	10.9±0.6
	Freight	162	5174	40	8±5
Zutphen	Passenger	11604	73332	796	10.9±0.6
	Freight	166	5310	114	21±2
Total	All	23540	157126	1747	

When the annual tonnage is extrapolated over the rail life, until the rail replacement in 2020, and assuming that the annual tonnage has remained the same, the total load is ~50 Mt. The replacement took place three years after the last cyclic preventive grinding in 2017 and the analysis was performed in 2022.

3.2.2. METHODS

The analysis of the rails started with the visual inspection of the running surface before sectioning. Figure 3.2 shows the local coordinate system together with the positions of the micrographs. $Y = Z = 0$ is positioned at the top of the rail profile.

To prepare the specimens, the rails were first cut into slices using a water-cooled BekaMak BMSY 320C band saw. Then the specimens were cut with a Struers Discotom-6 equipped with a ceramic blade. All specimens were mounted with Struers Polyfast and heated and pressed according to the specification of the producer. The surfaces were then prepared using SiC-paper with #80-#4000 grit size and polished with 3 µm and 1 µm diamond polishing fluid. Etching was done with nitric acid, diluted with ethanol to 2 vol% (Nital), for 10 seconds.

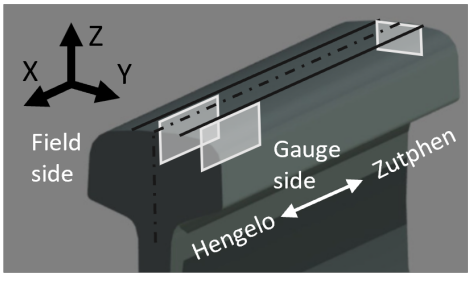

Figure 3.2: Scheme of the local coordinate system, and location and orientation of the metallographic cross-sections.

The observations are made using a Keyence VHX5000 digital microscope and a Jeol JSM 6500F scanning electron microscope, with an acceleration voltage of 15 kV and 9.5 mm working distance, in secondary electron imaging detection mode.

Four sets of hardness measurements were performed using a Struers Durascan 70 hardness tester:

- The first set is made to determine the hardness of the undeformed microstructure using a 10 N load for 10 seconds.
- Then, the hardness of the running surface is evaluated at the midpoint of the facets and at the facet transition zones. The differences in hardness are used as an estimate of the strain hardening of the rail under cyclic loading. A line of indents is made at seven positions, starting at the surface to $Z = -7$ mm, with an indent spacing of 0.25 mm. In this second set also 10 N load for 10 seconds is used.
- The aim of the third set is to characterize the WEL and BEL layers present at the running surface, using a 0.5 N indenter load.
- The fourth set aims to identify the hardness distribution of the running surface as a result of strain hardening and WEL formation for which a grid of indents with a mutual distance of 5 mm is made. A 30 N load is used for the hardness measurements which limits the observation variations due to local microstructural differences and thin surface layers.

3.3. RESULTS

3.3.1. SURFACE ANALYSIS

Figure 3.3 shows the ballasted railway track with wooden sleepers on which the rail is mounted with spring clips. The wheel-rail contact surface is light gray and contrasts with the corroded rail. The contact surface has a width of 22 ± 1 mm. At the gauge side of the rail a secondary contact is observed. The rail is lightly touched by the wheel flange, only removing the surface corrosion.

As a result of the preventive grinding maintenance in 2017, four facets are present, which are numbered 1 to 4 in this study. The facets are distinguished by the partly worn grinding grooves and the smooth transition zones separating them. Facets 1 and 2, close to the gauge side of the rail, where the rail head radius is small, have a width of 4 mm and

Figure 3.3: Railway track construction and characteristic contact surface, just before rail sample extraction in 2020. The numbers indicate the ground facets at the contact surface.

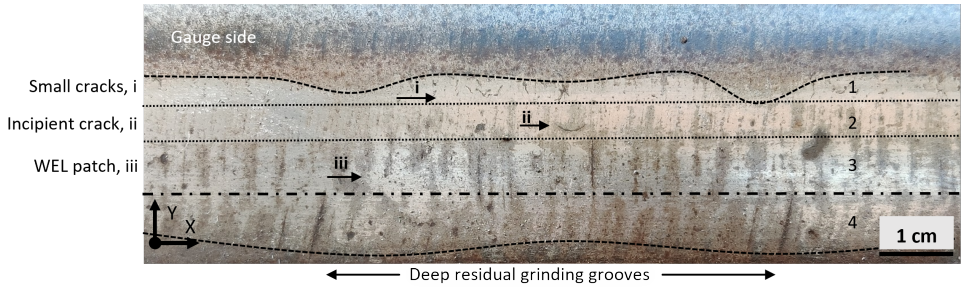

Figure 3.4: Rail contact surface as a result of the preventive grinding and wheel-rail contact. The deviations in the contact surface width are depicted with dotted lines. The ground facets are numbered 1 to 4. Cracks are present at facet 1, see i, an incipient crack at facet 2, see ii, and WEL at facet 3, see iii.

3 mm, respectively. Facets 3 and 4 have a width of 8 mm and 7 mm, and are situated on either side of the center line of the rail profile.

Figure 3.4 shows a detailed observation of the contact surface, with the facets also indicated. At the gauge side, next to facet 1, repetitive waves with an interspacing of 49 ± 2 mm are present. These waves are typical for the surface of the rail sections in this study. The surface corrosion visualizing the waves is the result of the absence of wheel contact and is most likely caused by local deviations in the rails' longitudinal profile. The darker spots, outside the contact surface at the gauge side, are formed by repetitive patches of corroded grinding grooves.

At the field side, next to facet 4, a more gradual wave is observed and depicted with a dotted line. A repetitive pattern of notch-like residual grinding grooves decorates the widest points. The notch spacing is 57 ± 1 mm and represents the characteristic length of the preventive grinding process performed at 12 km h^{-1} with a grinding train equipped with 64 grinding motors each operating at 3600 rpm.

On the contact surface, at both sides of the centerline, shiny WEL patches are observed after cleaning and light etching with Nital.

The facets 1 to 4 differ in the depth of the remaining grinding grooves. At facet 2 and especially facet 1, the surface is smooth and the grinding grooves are only recognized by a repetitive pattern in gray or as very shallow wrinkles. At the surface of facets 3 and 4 the pattern is clearly present and some deep, black colored residual grinding grooves are observed.

The damages in the surface of facet 1 are smaller than at other zones on the rail surface, exhibit a higher density and show a variety of orientations, whereas in facet 2 a larger incipient crack is observed, indicated wit ii. Figure 3.4 shows that the incipient crack is positioned close to the facet transition zone and between the deep residual grinding grooves at the gauge side of the contact surface.

Figure 3.5 shows the surface characteristics at facet 2 and the facet transition zone. The figure presents the surface of the same extracted rail but is taken outside the area shown in Figure 3.4, focusing on wider residual grinding grooves in facet 2 and facet 3. Figure 3.5A presents the surface after cleaning and light etching and Figure 3.5B shows the hardness contour plot which is constructed from a grid of measurements. The grind-

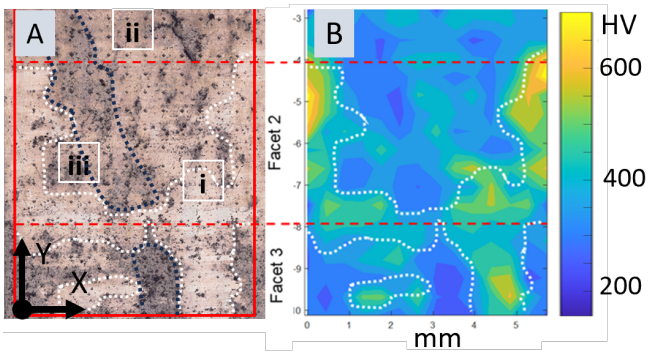

Figure 3.5: Detail of the rail surface. A) load-carrying surfaces, on which WEL-stripes are present (see i), surround the residual grinding groove, highlighted with dotted lines. In the grinding groove damage initiations are present, see ii and iii. B) The hardness distribution of that rail surface, showing locations of lower hardeness, the grinding groove (blue) and locations with higher hardness and WEL (yellow/green). The regions regions where WEL is observed are outlined by the white dotted lines.

ing grooves and the WEL are readily distinguished as the low-hardness blue and high-hardness yellow/green regions, respectively.

Figure 3.5A shows that the residual grinding grooves are surrounded by load-carrying surfaces and that a continuous band of WEL, indicated with i, is formed at the facet transition zone between facets 2 and 3. The surfaces of the grinding grooves are darker as a result of the absence of wheel contact and damage initiations, indicated with ii and iii, are present in the grinding grooves in both facet 1 and facet 2.

Figure 3.5B shows that large hardness differences are present in the rail surface, with strong gradients. The highest hardness of ~700 HV indicates the presence of WEL which is supported by the surface observations in Figure 3.5A. The crack in facet 2 initiates at the edge of the residual grinding groove.

3.3.2. CRACK PROPAGATION PATH

Investigating the subsurface crack propagation path is one of the objectives of this study. Short cracks propagate along the lamellae orientation of the deformed pearlitic microstructure, preferentially in the pro-eutectoid ferrite [6]. Directionality in longer cracks, for instance the squat defects, is visible in the difference between the leading crack planes and the trailing crack planes. The leading crack plane, in the running direction, propagates over longer lengths and greater depths compared to the trailing crack, developing in the opposite direction [37, 38, 39].

Figure 3.6 shows a characteristic symmetric squat defect. Figure 3.6A presents three of its distinguishing features: (1) the semi-elliptical crack tip with a length of 7 mm, (2) the parallel propagation paths towards the gauge side, and (3) the material extrusion at the side of the contact, where the crack deflects and becomes parallel to the running direction. All features are symmetrical in both running directions, with a slightly more pronounced development in positive X-direction.

Because of the defect size it, based on literature, Deng et al. [40] for instance, is

concluded that the damage initiation took place before the preventive grinding maintenance was performed. Cracks at the surface tend to shift towards the center line of the rail due to grinding. A displacement as much as 3 mm can occur [40]. The actual position of the semi-elliptical crack tip is close to the facet transition zone between facets 2 and 3.

Figure 3.6A shows a dark spot that is formed at the rail surface (see *i*). Locally reduced contact allows for the build-up of intermediate surface layers to form the dark spot. It indicates, together with contact surface widening (see *ii*), the presence of a subsurface crack plane [37]. The increased wheel slip causes longitudinal slip marks, see *iii*, spalling, and WEL formation. The arrow, see *iv*, indicates the probable displacement of the wheel-contact area.

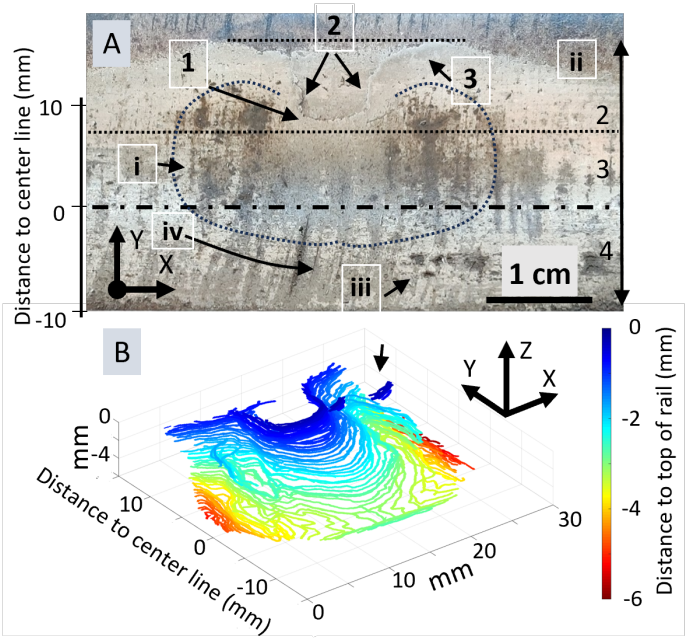

Figure 3.6: Symmetric squat defect with semi-elliptical crack tip. A) Three distinguishing features are indicated: (1) the semi-elliptical crack tip, (2) the parallel propagation paths, and (3) the deflection of the crack path. The dark spot, see *i*, is the result of intermediate-layer build-up and evidences the subsidence of the surface. The contact surface shows widening, see *ii*, longitudinal slipmarks, see *iii*, and spalling of material. The arrow indicates the probable wheel-contact displacement, see *iv*. B) 3D-representation of the subsurface crack plane composed of all contour lines after surface milling. The arrow indicate crack initiations present at a similar transverse position.

Figure 3.6B shows the subsurface crack plane situated under the dark spot in Figure 3.6A. Each line represents a crack contour observed at the milled surface. During each of the first 20 milling passes a layer thickness of 0.05 mm is removed, followed by 0.1 mm per pass until the crack was fully removed. Two additional superficial U-shaped cracks were found close to the crack tip, both initiated at a similar Y-position. These cracks are

indicated by the arrow in Figure 3.6B.

At a distance from the surface, $Z = -2$ mm, shallow crack branches are found. Crack branching and the subsequent development of parallel crack planes is a known propagation sequence [37]. These secondary cracks initiate at a later crack propagation stage. Therefore crack length and the distance to the surface are no indication for the moment of initiation.

The subsurface crack plane develops in $-Y$-direction, towards the field side of the rail, and in both longitudinal directions. The saddle-shaped plane forms a plateau at a depth of $Z = -3.1$ mm and $Y = -2$ mm. Initially, the crack propagates at a high angle and then deflects to a shallow crack plane orientation of 11°. The crack plane bends upwards at the field side.

The crack plane was assessed on a longitudinal section through both crack tips to study the propagation in the longitudinal directions. The crack plane pointing in X-direction is slightly longer, and from $Z = -4.0$ mm a crack plane propagation angle of 24° is observed. The crack plane reaches a depth of $Z = -5.8$ mm at $Y = 5$ mm. In the opposite direction, at the similar Y-position, a crack plane angle of 30° is found between $Z = -4.0$ mm and $Z = -5.1$ mm. A deflection of the crack at the deepest point of the plane, indicating the onset of growth acceleration, has not been observed in this work.

The observations of the crack propagation path show the symmetry in the subsurface crack planes. Only minor differences in the orientation, length, and depth are present in both longitudinal directions. The equal shape and dimensions of both crack planes, and the initial high propagation plane angle, are notable differences from the observations in rails with unidirectional traffic.

3.3.3. CROSS-SECTION ANALYSIS

Cross-sections of the four facets are studied to identify local hardness variations, specific deformation characteristics, and local WEL formation.

Pearlitic rail steels are known for their strain-hardening behavior and the exceedance of the yield limit results in an increase of the hardness and strength [41]. Figure 3.7 shows the hardness distribution of the contact surface with in Figure 3.7A the measured hardness profiles in blue for facets 1 and 2, and in red for facets 3 and 4. Figure 3.7B presents the corresponding measurement positions on the cross-section.

The hardness in facets 1 and 2 is 301 ± 7 HV close to the surface and decreases gradually to the measured bulk hardness at a distance of 5 mm. The hardness at facets 3 and 4 only shows an increase at a distance 3 mm to 4 mm while close to the surface no increase in hardness is measured. The hardness variation in the running surface is an indication of uneven contact stress distribution in the running surface. The subsurface increase is most likely caused by the maximum subsurface stress from the wheel-rail contact patch [4].

Figures 3.8A-D show the cross-section of facets 1 to 3 to observe the surface, which is virtually free of corrosion, and the microstructure. Figure 3.8A presents the facet transition zone between facets 2 and 3. Locally no WEL is present at the surface. The WEL detachment, indicated in the figure, forms a damage initiation site that has been reported in the literature [25, 29, 42].

Figures 3.8B and 3.8C show the surface of facet 2. The lens-shaped WEL at the surface

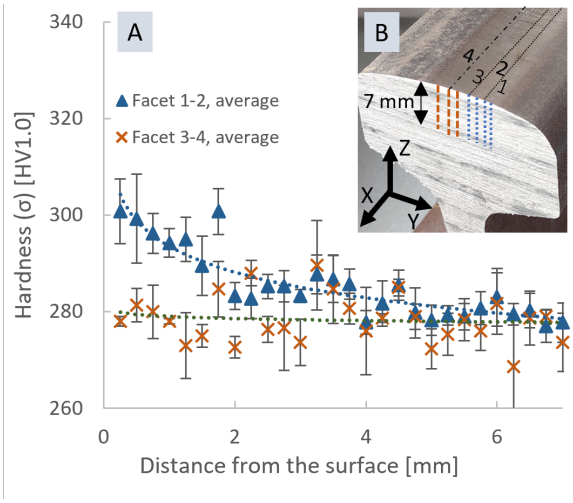

Figure 3.7: The hardness distribution below the running band. A) Graph presenting the hardness measured on the cross-section of facets 1 and 2 in blue and facets 3 and 4 in orange. The hardness is measured from a distance of 0.25 mm to the surface, until 7 mm distance. B) The location of the hardness indents on the cross-section. The colors correspond with the colors in the graph.

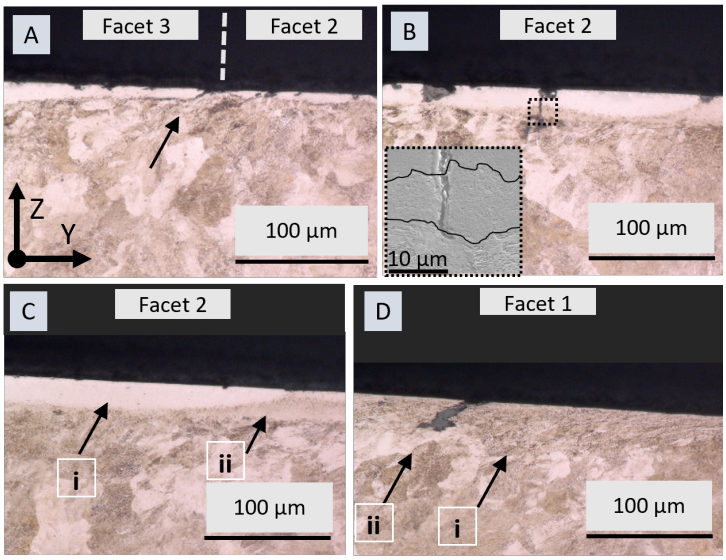

Figure 3.8: Cross-section of facets 1 to 3 observed in X-direction. A) At the facet transition zone between facets 2 and 3 is locally no WEL observed. WEL-detachment is indicated with the arrow. B) WEL is present at the surface of Facet 2. The observed crack does not propagate into the bulk. C) WEL is present, see i, and partly embedded in BEL, see ii. D) Unidirectional deformation is present beneath the surface of facet 1, see i, and a superficial crack is present, see ii.

is embedded in a BEL, evidencing a history of slip events. The crack in Figure 3.8B starts at a corrosion pit and propagates through these layers, but the stresses do not exceed the critical level to grow the crack into the bulk material. This is highlighted by the inserted SEM image in which the lines depict the WEL and BEL boundaries.

In facet 2, close to facet 1, the lens-shaped WEL is partly embedded in BEL, which is in Figure 3.8C indicated with i and ii, respectively.

Figure 3.8D shows the surface of facet 1. This surface is WEL free and subsurface deformation is present. The deformation orientation is in Y-direction, towards the gauge side of the rail, see i, and the maximum depth of deformation is ~50 µm. The orientation suggests the presence of a shear stress component in the wheel-rail contact that points in that direction. The superficial crack, indicated with ii, is one of the many cracks observed in facet 1.

3.3.4. LONGITUDINAL SECTION ANALYSIS

Figure 3.9 shows the micrograph of the surface condition in facet 2, closest to the transition to facet 3. Although the WEL surface is corroded, the presence of thick WEL and BEL indicates a history of wheel slip events. The total thickness of WEL and BEL is ~80 µm, allowing hardness measurements to be carried out. The hardness of the WEL is 828 HV, which increases to 859 HV at the WEL-BEL interface. The hardness of the BEL is significantly lower, between 650 HV and 700 HV. WEL and BEL layers are prone to crack initiation [24, 32, 42]. In this micrograph a crack is present, which is one of a group of closely clustered cracks. None of these cracks propagates into the bulk material.

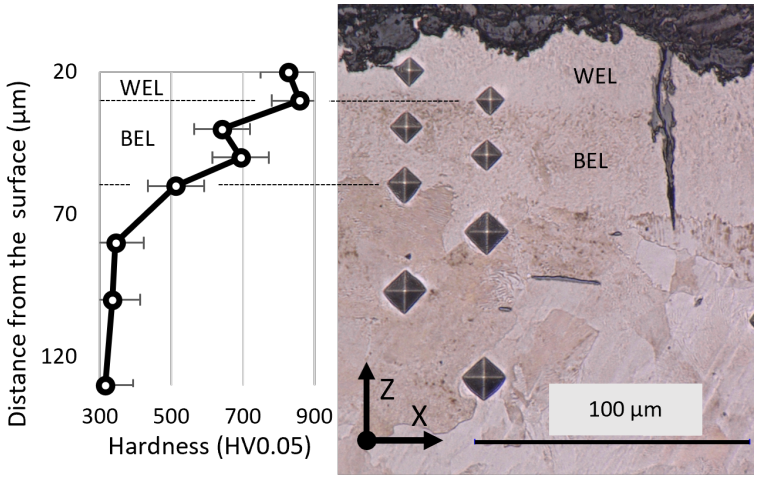

Figure 3.9: Longitudinal section of Facet 2, closest to the facet transition with facet 3. A 80 µm corroded WEL and BEL is present at the surface. The graph presents the measurement results at the corresponding measurement positions.

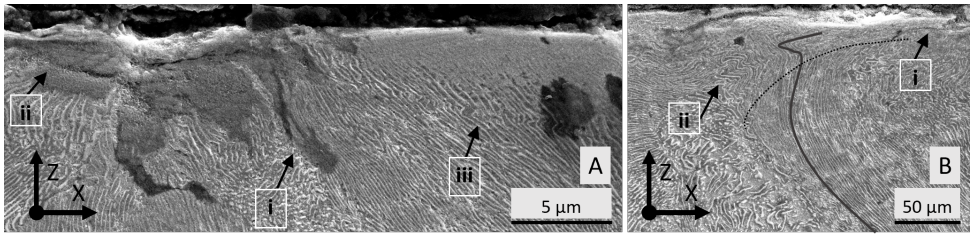

Figure 3.10: Longitudinal section of Facet 2, closest to the facet transition with facet 3. The observations are made using high-magnification SEM. A) Damage initiates, see *i*, between the oxide-filled irregularity, see *ii*, and the WEL patch at the contact surface. Wrinkled pearlite lamellae are present at the edge of the WEL, see *iii*. B) A wear tongue and s-shaped deformation patterns, associated with the bi-directional use of the railway line, are present, see *i*. Wrinkled pearlite lamellae evidences multiple deflection occurrences, see *ii*.

Figure 3.10 shows micrographs from the same specimen as shown in Figure 3.9. Figure 3.10A presents the surface which is defined by a rough zone next to a WEL. The WEL has a smooth surface and is ~3 µm thick. The pearlite lamellae at the edge of the layer, indicated with *iii*, are wrinkled. The rough zone is filled with debris and detached layers, see *ii*, which is an indication of the absence of wheel contact. Two cracks are observed, although some over-etching limits the observation clarity. The first crack initiates at the bottom of the irregularity, and the second at the edge of the WEL patch, which is indicated with *i*.

It is known that the dominant direction of the tangential shear forces defines the deformation orientation [25, 28, 32] and also that, in this study, the shear stress direction reverses after almost every train passage. Figure 3.10B shows the microstructure close to the surface.

A 10 µm refined surface layer is present which is the result of intense plastic deformation [1, 7]. Wear tongues are pointing in the X-direction, see *i*. The full black line highlights the long C-shaped deformation with a sharp S-shaped pattern, closer to the surface. This pattern is concentrated in a band which is marked by a dotted line. Wrinkled lamellae are sometimes observed in pearlite as a result of compression or thermal contraction. The wrinkled lamellae, indicated with *ii*, show evidence of multiple deflection occurrences and it is concluded from the sharp bending and amplitude variations that these are the result of external shear stress reversal. This specific pattern was also observed by Tyfour and Beynon [10] in rolling direction reversal experiments.

3.4. DISCUSSION

The contact surface condition that is characteristic of this railway line is the result of the rail maintenance and the single-stock and bi-directional use. In this section the observed inhomogeneous wear, surface hardening, and damage initiation mechanisms are discussed with respect to the low axle load, low traffic density and observed damage.

3.4.1. INHOMOGENEOUS WEAR AND LOADING

Preventive maintenance grinding was performed in 2017 and ~5 Mt of train traffic has rolled over the ground surface until the rail sections are extracted in 2020. The grinding maintenance has introduced facets on the surface which are recognizable by the presence of grinding grooves having similar orientations. Figure 3.4 shows that the surfaces of the transition zones between the facets are relatively smooth. At the surface of facets 1 and especially 2, some remains of the grinding-related roughness are present, whereas at facets 3 and 4, transverse grooves are still shown and surrounded by a rougher surface. These differences in surface condition are the result of local differences in the contact conditions and rail wear.

With the simple wear law of Archard, $Q = AF_N\gamma_D / H$ [43], the wear volume Q is predicted from the loading conditions, normal force F_N and sliding distance γ_D, and H the surface hardness. A is a constant. The wear mechanism described by Archard is the formation of wear slivers during asperity encounter and plastically deform, under the influence of applied load and slip.

The normal load and the micro-slip in the wheel-rail contact are not homogeneously distributed as a result of the conical wheel tread and the rail-head curvature, resulting in hardness differences of that surface. Although the wear rate changes with the increase in surface hardness, locations with highest deformation and wear are assumed the locations with highest value of $F_N\gamma_D$ in the wheel-rail-contact, no increase in hardness is expected when $F_N\gamma_D$ is low.

Figure 3.7 shows the hardness distribution along the contact surface. The bulk hardness of the R260Mn rail steel is 278 ± 8 HV 1 and it is observed that the same hardness is present at facets 3 and 4. But in facets 1 and 2 , the hardness is higher. From the observed differences in hardness, and the observed microstructure deformation in facets 1 and 2, it is concluded that WL is higher in facets 1 and 2 compared to 3 and 4, which explains the observed differences in surface wear.

Tyfour and Beynon [8] observed that the unidirectionally strained pearlite starts to realign with the new shear stress direction after reversal of the rolling direction. It is therefore expected that the bi-directional traffic conditions result in the reorientation in the microstructure. More importantly, Tyfour and Beynon [8] also observed a temporary but significant reduction in wear rate after rolling direction reversal, which only raised to the former level when the realigning was completed.

The uniform straining of the pearlite lamellae in the microstructure at facets 1 and 2 is directed towards the gauge side of the rail. This deformation orientation is the result of the running-direction independent lateral slip, which is always directed towards the track center. The slip forces in the wheel-rail contact play an important role in the guidance and stable running of trains [4]. Johnson [4] has made a distinction in slip directions. Longitudinal micro-slip, in X-direction, lateral micro-slip, in Y-direction, and

spin. Longitudinal micro-slip is the result of traction and braking. The lateral micro-slip results from small yaw angles between the plane of the wheel and the rail and contributes to the self-centering of the wheelset. Spin is the angular velocity relative to the rail, which occurs when the plane of the contact is not parallel to the wheelset axis of rotation, i.e. the axle. Spin is typically strongest at the gauge corner and the gauge face.

The deformation beneath the surface at the contact extreme at the gauge side can be explained as follows. With the change in running direction, it is evident that the traction direction changes as well, and, as a result, the longitudinal micro-slip direction. The self-centering forces, in Y-direction, balance the train, supported by conical wheels mounted on a rigid axle, between the two rails. The lateral slip direction is therefore independent of the running direction and causes the deformation orientation as observed at facets 1 and 2.

The frequent reversal provides a reliable explanation for lower wear in the contact center while the higher load and the unidirectional share in the slip cause a relatively high wear rate. These different loading conditions on the top of the rail and in facets 1 and 2 explain the observed inhomogeneous wear of the rail surface.

3.4.2. WAVINESS AND WEL FORMATION

Waviness is observed at both sides of the running surface, indicating a variation in the contact surface width. This variation in width is, in itself, a result of a periodic irregularity in the longitudinal rail profile, a surface topography with ripples [44]. The highest points are indicated as 'hill' and the lowest as 'valley'. The presence of these ripples cause differential wheel-rail contact conditions.

The periodic deep residual grinding grooves in facet 4 indicate that this is the characteristic length of the preventive grinding. Between both grooves in facet 4, in adjacent facet 3, a sharp notch is present, indicating a pattern shift between both facets. This pattern shift in single-pass grinding is caused by the longitudinal placement of the multiple grinding motors in the grinding train. The wavelength at the gauge side of the rail, being 49 ± 2 mm, is shorter. This wavelength might be caused by prior grinding maintenance. However, the absence of repetitive grinding grooves could also point to short-pitch corrugation as the cause.

Short-pitch corrugation is a differential rail wear mechanism resulting in a periodic irregularity of the contact surface. Grassie and Kalousek [45] showed rail corrugation wavelengths from 500 mm to 1500 mm for light-rail railway lines. These wavelengths are caused by P2-resonance which occurs when the unsprung mass of the train excites the track. Li et al. [46] observed that the wavelength is best explained by the pinned-pinned frequency of the rail itself, which is 400 Hz to 1200 Hz. This frequency range corresponds, at the line speed of 130 km h^{-1}, with a wavelength of 30 mm to 90 mm. Short-pitch corrugation is generally observed to have a pitch of 25 mm to 80 mm [46, 47].

When a periodicity in the longitudinal profile is present, the resulting contact stress variations will also cause differences in the rail surface. Wild et al. [44] studied the rail surface with severe, 35 mm wavelength, short-pitch corrugation. They observed WEL to be present at the hill of the ripple, while in the valley strong plastic deformation is observed. The WEL observed by Wild et al. [44], is lens-shaped, shows an abrupt transition to the bulk and has a hardness between 767 HV and 915 HV. Steenbergen and Dollevoet

[24] and Pan et al. [28] have attributed these characteristics to WEL that is wheel-slip induced.

Crack initiation at the 'hill' of the rail corrugation is observed in high-speed railway lines, and is named 'belgrospi' after Belz, Grohmann, and Spiegel [48]. It is in this study shown that WEL is present at hill parts of the running surface, which is in agreement with the observations by Wild et al. [44]. Although several researchers [25, 29, 37, 49], associate the presence of the hard and brittle WEL in itself with defect initiation, the cracks in the WEL and BEL layers in this work are not observed to penetrate into the bulk material. Therefore, it is concluded that a different mechanism takes place.

The incipient crack has initiated in the valley of the corrugation wave at the running surface, as shown in Figure 3.4. Wild et al. [44] showed that wheel-rail contact in the valley zones results in lamellae that are strained parallel to the surface. Rolling contact fatigue cracks tend to initiate between these elongated lamellae. Simon et al. [7] studied the strain orientation within the rail steel to explain the incipient squat initiation position. They observed that the deformation underneath the contact surface is not uniform as a result of the shear orientation distribution in the wheel contact. Squats are found to initiate preferentially at positions where bands with opposing deformation orientations meet.

Observations on the metallographic cross-sections have shown that, as a result of the bi-directional traffic conditions, different deformation orientations meet at the initiation position of the incipient crack in facet 2, closest to facet 3. The deformation in the lateral direction, as observed in Figure 3.8, is reinforced with every train passage, independent of the running direction. This deformation is also evidenced by the local increase in hardness, as shown in Figure 3.7. In the longitudinal direction only shallow C-shaped deformation is present.

3.4.3. DAMAGE MECHANISM

At the rail surface a global and a local damage mechanism are observed. In the previous section the focus was on short-pitch corrugation and the associated WEL and deformation, which are collectively considered the global mechanism facilitating damage initiation.

The specific local surface conditions, at the damage initiation position of the incipient crack, are examined in more detail. This is of interest since the cracks like the symmetric squat defect presented in Figure 3.6 appear to have initiated at a similar position.

Local damage formation has been explained by different researchers based on different aspects of surface conditions. Steenbergen and Dollevoet [24] and Mojumder et al. [29] observed damage to initiate at, or close to the interface between the WEL patch that is formed at the surface, and the deformed material that is surrounding it. Deng et al. [40] observed that defects may initiate due to the local contact stress concentration at the edge of a depression when present on the running surface.

The surface condition after grinding was studied by various researchers to explain grinding-related damage initiations. Fau et al. [23] and Mesaritis et al. [22] observed that contact stress concentrations in the facet transition zone may result in damage initiation. The differences in shear stress orientation at the surface, as previously mentioned, cause different strain orientations. Simon et al. [7] observed squats to initiate at

the interface of bands having opposing deformation orientations.

The damage initiation position in facet 2, closest to facet 3, may be considered as the transition zone between the surface condition formed under the influence of rolling direction reversal and the surface state resulting from lateral slip. Tyfour and Beynon [8] experimentally observed a reduction in the wear rate directly after rolling direction reversal, which may contribute to the formation of the surface condition.

Although the surface at facet 2 is relatively smooth, residuals of the grinding roughness are still locally present. These residual grinding grooves are surrounded by WEL-coated contact surfaces.

The local damage mechanism is related to the surface condition that arises after grinding. Under the specific loading conditions, wear is insufficient to remove the grinding roughness completely. And when there is a build-up of WEL in a region of residual grinding grooves, it is observed that cracks typically initiate at the root of the groove close to the facet transition. The surface crack subsequently follows the edge of the grinding groove.

3.4.4. CRACK PROPAGATION

The low-axle load and bi-directional traffic influence the crack propagation in two ways. First, under the bi-directional traffic conditions no dominant running direction is present. Second, a crack plane orientation, due to the presence of only shallow wrinkled lamellae, is not evident.

Zerbst et al. [5] observed that, at shallow depth, the crack propagation plane is mostly defined by the shear stress orientation and is therefore expected to propagate in the running direction first. In most cases the propagation is at a 10° to 20° angle with the surface, and deflects at a limited depth to follow an approximately 35° propagation angle. Also Grassie et al. [50] and Steenbergen and Dollevoet [37] observed, under uni-directional traffic conditions, a shallow angle crack propagation plane close to the surface.

Although both the preventive grinding maintenance and wear have changed the surface and removed the actual damage initiation conditions, the 3D-representation of the crack plane in Figure 3.6B shows that the crack propagation angle, directly beneath the surface, is relatively high. No deflection of the crack plane occurs until a crack depth of ~2 mm is reached. Tyfour and Beynon [10] observed that, after rolling direction reversal, cracks re-initiated and branched to align with the reversed stress orientation. Re-initiation takes time and may not occur due to the frequent reversal of the shear stress. Under these conditions, a relatively steep crack orientation may occur. The subsurface propagation is not guided by the deformed lamella orientation as a consequence of the limited microstructural deformation but by the principal stresses only.

At the railway line the passenger trains are symmetrically distributed in number and weight, only the freight trains running to Zutphen have a significantly higher axle load. The crack plane orientations pointing in both running directions are fairly symmetric, although the increased traction forces may explain the observed difference in propagation plane angle, as, provided uni-directional rolling conditions, a leading crack plane of a squat rail defect, pointing in the running direction, is longer and deeper compared to the steep trailing crack plane, propagating against the running direction [37, 38, 39, 50].

The observed crack plane in Figure 3.6, propagating in Y-direction, towards the field

side of the running surface, shows an angle of 11° with respect to the horizontal plane and reaches a depth of 3.1 mm. The cracks that propagate beyond that depth do not longer form a continuous contour, and the crack planes in both longitudinal directions are not connected anymore. The crack plane branches to a more shallow propagation angle of 30° in $+X$-direction, the direction of Hengelo and $-24°$ in $-X$-direction, towards Zutphen. It is known that the increase in traction, and therefore in tangential shear stress, moves the principal shear stress to the surface [4], and in these situations, the subsurface cracks tend to propagate at a shallow angle, although with depth the influence of shear stress and contact stress diminishes. Bending and mode II shear become more important [5].

Tyfour and Beynon [10] observed cracks to branch, in rolling-direction reversal experiments, aligning with the new shear stress orientation. In this study no crack path re-orientation is observed which may be caused by the frequent reversions and the limited number of load cycles to re-initiate a new crack path. The crack plane being steep-angled may nevertheless be explained by the crack path re-orientation mechanism.

3.5. CONCLUSIONS

The main purpose of the present work is to identify the reasons for damage initiation in rails of single-track railway lines. It is concluded that:

- The running surface sees differential wear rates. Facets and grinding grooves of preventive grinding maintenance are still present at the center of the contact surface after ~5 Mt of train load, but are worn off at the gauge side. S-shaped deformation of the lamellae underneath the contact surface is caused by the reversal of the shear stress. The hardness increase below the center of the contact surface is small, and the thick WEL indicates the presence of strong wheel slip. The pearlite lamellae show unidirectional strain deformation close to the gauge side which is explained by the rolling-direction independent lateral slip in the wheel-rail contact.

- At the contact surface of the rail a global and a local damage mechanism are observed. The global damage mechanism is caused by corrugation. Corrugation was not entirely removed during the last preventive maintenance grinding cycle. As a consequence of the longitudinal waviness in the rail surface, WEL patches emerge at the hill part of the ripple. A novel observation is the damage initiation in the valley part of the rail corrugation.

- The local damage mechanism is related to the surface condition that arises after grinding. Under the specific loading conditions, wear is insufficient to remove the grinding roughness completely. Before the roughness is removed, WEL builds up around the grinding grooves and damage may initiate as a result of stress concentration at the facet transition and WEL interface.

- The symmetric squat defect mapped in Figure 3.6 develops a subsurface saddle shape, displaying crack propagation in lateral and both longitudinal directions. The 'crack saddle' reaches a depth of 3.1 mm, and bends upwards at the field side. Beyond that depth, independent crack propagation takes place in both running directions. The observed close similarity in crack plane lengths and angles is explained by the bi-directional traffic, causing crack growth under reversing shear stresses of equivalent magnitudes.

- The preventive grinding maintenance specifications for regional railway lines must be improved based on the observations in this study. Stringent requirements on surface roughness and the minimum number of facets will reduce the number of potential crack initiation sites. These specifications should also include directions for the removal of short-pitch corrugation. Moreover, the presence of corrugation requires additional material removal to avoid damage to initiate in the ripple valley.

BIBLIOGRAPHY

[1] F.A.M. Alwahdi, A. Kapoor, and F.J. Franklin. "Subsurface microstructural analysis and mechanical properties of pearlitic rail steels in service". In: *Wear* 302.1-2 (Apr. 2013), pp. 1453–1460. ISSN: 00431648. DOI: 10.1016/j.wear.2012.12.058.

[2] W.R. Tyfour, J.H. Beynon, and A. Kapoor. "Deterioration of rolling contact fatigue life of pearlitic rail steel due to dry-wet rolling-sliding line contact". In: *Wear* 197 (1996), pp. 255–265.

[3] B. Dylewski, M. Risbet, and S. Bouvier. "The tridimensional gradient of microstructure in worn rails – Experimental characterization of plastic deformation accumulated by RCF". In: *Wear* 392-393 (2017), pp. 50–59. ISSN: 00431648. DOI: 10.1016/j.wear.2017.09.001.

[4] K.L. Johnson. *Contact Mechanics*. Cambridge University Press, May 1985. ISBN: 9780521255769. DOI: 10.1017/CBO9781139171731.

[5] U. Zerbst et al. "Introduction to the damage tolerance behaviour of railway rails - a review". In: *Engineering Fracture Mechanics* 76.17 (Nov. 2009), pp. 2563–2601. ISSN: 00137944. DOI: 10.1016/j.engfracmech.2009.09.003.

[6] J.E. Garnham and C.L. Davis. "Very early stage rolling contact fatigue crack growth in pearlitic rail steels". In: *Wear* 271.1-2 (May 2011), pp. 100–112. ISSN: 00431648. DOI: 10.1016/j.wear.2010.10.004.

[7] S. Simon et al. "Tribological characterization of rail squat defects". In: *Wear* 297.1-2 (Jan. 2013), pp. 926–942. ISSN: 00431648. DOI: 10.1016/j.wear.2012.11.011.

[8] W.R. Tyfour and J.H. Beynon. "The effect of rolling direction reversal on the wear rate and wear mechanism of pearlitic rail steel". In: *Tribology International* 27.6 (Dec. 1994), pp. 401–412. ISSN: 0301679X. DOI: 10.1016/0301-679X(94)90017-5.

[9] D. Zeng et al. "Effect of bi-directional operation on rolling-sliding wear of wheel steel under variable amplitude loading". In: *Proceedings of the Institution of Mechanical Engineers, Part J: Journal of Engineering Tribology* 230.2 (Feb. 2016), pp. 186–195. ISSN: 1350-6501. DOI: 10.1177/1350650115594955.

[10] W.R. Tyfour and J.H. Beynon. "The effect of rolling direction reversal on fatigue crack morphology and propagation". In: *Tribology International* 27.4 (Aug. 1994), pp. 273–282. ISSN: 0301679X. DOI: 10.1016/0301-679X(94)90007-8.

[11] E. Magel, J. Kalousek, and P. Sroba. "Chasing the magic wear rate". In: *Civil-Comp Proceedings*. Vol. 104. Civil-Comp Press, 2014. DOI: 10.4203/ccp.104.116.

[12] R. de Vries, P. Sroba, and E. Magel. "Preventive Grinding Moves into the 21 st Century on Canadian Pacific Railway". In: *Proceedings from the AREMA Annual Conference, Chicago, IL*. 2001.

[13] E. Magel et al. “The blending of theory and practice in modern rail grinding”. In: *Fatigue and Fracture of Engineering Materials and Structures* 26.10 (2003), pp. 921–929. ISSN: 8756758X. DOI: 10.1046/j.1460-2695.2003.00669.x.

[14] S.L. Grassie. “Rolling contact fatigue on the British railway system: Treatment”. In: *Wear*. Vol. 258. 7-8. Mar. 2005, pp. 1310–1318. DOI: 10.1016/j.wear.2004.03.065.

[15] CEN. *EN13231-2 - Railway application - Track - Acceptance of works - Part 2: Acceptance of reprofiling rails in plain line, switches, crossings and expansion devices*. 2020.

[16] S. Kalpakjian, S.R. Schmid, and K.S. Vijay Sekar. *Manufacturing Engineering and Technology*. 7th SI Edition. Pearson, 2014, pp. 1–1224. ISBN: 9780133128741.

[17] A. Darafon, A. Warkentin, and R. Bauer. “3D metal removal simulation to determine uncut chip thickness, contact length, and surface finish in grinding”. In: *International Journal of Advanced Manufacturing Technology* 66.9-12 (June 2013), pp. 1715–1724. ISSN: 02683768. DOI: 10.1007/s00170-012-4452-1.

[18] S. Malkin and C. Guo. “Thermal Analysis of Grinding”. In: *CIRP Annals* 56.2 (2007), pp. 760–782. ISSN: 00078506. DOI: 10.1016/j.cirp.2007.10.005.

[19] B. Lin et al. “Influence of grinding parameters on surface temperature and burn behaviors of grinding rail”. In: *Tribology International* 122 (June 2018), pp. 151–162. ISSN: 0301679X. DOI: 10.1016/j.triboint.2018.02.017.

[20] E. Uhlmann et al. “Influence of rail grinding process parameters on rail surface roughness and surface layer hardness”. In: *Wear* 366-367 (Nov. 2016), pp. 287–293. ISSN: 00431648. DOI: 10.1016/j.wear.2016.03.023.

[21] J. Wu et al. “Laboratory simulation of martensite formation of white etching layer in rail steel”. In: *International Journal of Fatigue* 91 (Oct. 2016), pp. 11–20. ISSN: 01421123. DOI: 10.1016/j.ijfatigue.2016.05.016.

[22] M. Mesaritis et al. “Post-field grinding evaluation of different rail grades in full-scale wheel/rail laboratory tests”. In: *Tribology International* 177 (Jan. 2023). ISSN: 0301679X. DOI: 10.1016/j.triboint.2022.107980.

[23] F. Fau et al. “Effect of grinding quality, lubrication quality and rail hardness on flaking defect initiation on high rails”. In: *Proc. 10 th Int. Conf. Contact Mech. Wear Rail/Wheel Systems CM2015, Colorado, USA*. Vol. 30. 2015.

[24] M. Steenbergen and R. Dollevoet. “On the mechanism of squat formation on train rails - Part I: Origination”. In: *International Journal of Fatigue* 47 (Feb. 2013), pp. 361–372. ISSN: 01421123. DOI: 10.1016/j.ijfatigue.2012.04.023.

[25] Q. Lian et al. “Crack propagation behavior in white etching layer on rail steel surface”. In: *Engineering Failure Analysis* 104 (Oct. 2019), pp. 816–829. ISSN: 13506307. DOI: 10.1016/j.engfailanal.2019.06.067.

[26] C.J. Rasmussen et al. “Surface crack formation on rails at grinding induced martensite white etching layers”. In: *Wear* 384-385 (Aug. 2017), pp. 8–14. ISSN: 00431648. DOI: 10.1016/j.wear.2017.04.014.

[27] J. Wu et al. “Micro and Nanoscale Characterization of Complex Multilayer-Structured White Etching Layer in Rails”. In: *Metals* 8.10 (Sept. 2018), p. 749. ISSN: 2075-4701. DOI: 10.3390/met8100749.

[28] R. Pan et al. “Investigation into the microstructure evolution and damage on rail at curved tracks”. In: *Wear* 504-505 (Sept. 2022). ISSN: 00431648. DOI: 10.1016/j.wear.2022.204420.

[29] S. Mojumder et al. “Effect of track curvature on the microstructure evolution and cracking in the longitudinal section of lower gauge corner flow lips formed in rails”. In: *Engineering Failure Analysis* 135 (May 2022). ISSN: 13506307. DOI: 10.1016/j.engfailanal.2022.106117.

[30] S. Li et al. “"Brown etching layer": A possible new insight into the crack initiation of rolling contact fatigue in rail steels?” In: *Engineering Failure Analysis* 66 (Aug. 2016), pp. 8–18. ISSN: 13506307. DOI: 10.1016/j.engfailanal.2016.03.019.

[31] M. Messaadi and M. Steenbergen. “Stratified surface layers on rails”. In: *Wear* 414-415 (2018), pp. 151–162. ISSN: 00431648. DOI: 10.1016/j.wear.2018.07.019.

[32] A. Al-Juboori et al. “Characterisation of White Etching Layers formed on rails subjected to different traffic conditions”. In: *Wear* 436-437 (Oct. 2019). ISSN: 00431648. DOI: 10.1016/j.wear.2019.202998.

[33] V. Mattos Ferreira. “Microstructural phenomena in pearlitic railway steels”. PhD thesis. Delft University of Technology, 2024. DOI: 10.4233/uuid:facb282f-74a1-446d-bbc6-5ed294602ed2.

[34] M. Mesaritis et al. “A laboratory demonstration of rail grinding and analysis of running roughness and wear”. In: *Wear* 456-457 (Sept. 2020). ISSN: 00431648. DOI: 10.1016/j.wear.2020.203379.

[35] M. Steenbergen. “Rolling contact fatigue in relation to rail grinding”. In: *Wear* 356-357 (June 2016), pp. 110–121. ISSN: 00431648. DOI: 10.1016/j.wear.2016.03.015.

[36] CEN. *prEN13674-1 - Railway applications - Rail - Part 1: Vignole railway rails 46 kg/m and above*. European Committee for Standardization, 2023, pp. 1–112.

[37] M. Steenbergen and R. Dollevoet. “On the mechanism of squat formation on train rails - Part II: Growth”. In: *International Journal of Fatigue* 47 (Feb. 2013), pp. 373–381. ISSN: 01421123. DOI: 10.1016/j.ijfatigue.2012.04.019.

[38] M. Steenbergen. “Rolling contact fatigue: Spalling versus transverse fracture of rails”. In: *Wear* 380-381 (2017), pp. 96–105. ISSN: 00431648. DOI: 10.1016/j.wear.2017.03.003.

[39] S.L. Wong et al. “A branch criterion for shallow angled rolling contact fatigue cracks in rails”. In: *Wear* 191.1-2 (Jan. 1996), pp. 45–53. ISSN: 00431648. DOI: 10.1016/0043-1648(95)06621-7.

[40] X. Deng et al. “Investigation of the formation of corrugation-induced rail squats based on extensive field monitoring”. In: *International Journal of Fatigue* 112 (2018), pp. 94–105. ISSN: 01421123. DOI: 10.1016/j.ijfatigue.2018.03.002.

[41] R. Masoudi Nejad, K. Farhangdoost, and M. Shariati. “Microstructural analysis and fatigue fracture behavior of rail steel”. In: *Mechanics of Advanced Materials and Structures* 27.2 (Jan. 2020), pp. 152–164. ISSN: 1537-6494. DOI: 10.1080/15376494.2018.1472339.

[42] R.I. Carroll and J.H. Beynon. “Rolling contact fatigue of white etching layer: Part 1. Crack morphology”. In: *Wear* 262.9-10 (Apr. 2007), pp. 1253–1266. ISSN: 00431648. DOI: 10.1016/j.wear.2007.01.003.

[43] J.F. Archard and W. Hirst. “The wear of metals under unlubricated conditions”. In: *Proceedings of the Royal Society of London. Series A. Mathematical and Physical Sciences* 236.1206 (Aug. 1956), pp. 397–410. ISSN: 0080-4630. DOI: 10.1098/rspa.1956.0144.

[44] E. Wild et al. “Microstructure alterations at the surface of a heavily corrugated rail with strong ripple formation”. In: *Wear* 254.9 (2003), pp. 876–883. ISSN: 00431648. DOI: 10.1016/s0043-1648(03)00239-4.

[45] S.L. Grassie and J. Kalousek. “Rail corrugation : characteristics, causes and treatments”. In: *Proceedings of the Institution of Mechanical Engineers, Part F: Journal of Rail and Rapid Transit*. 1993, pp. 57–68.

[46] Z. Li et al. “Mechanism of short pitch rail corrugation: initial excitation and frequency selection for consistent initiation and growth”. In: *International Journal of Rail Transportation* (2022). ISSN: 23248386. DOI: 10.1080/23248378.2022.2156402.

[47] K.H. Oostermeijer. “Review on short pitch rail corrugation studies”. In: *Wear* 265.9-10 (Oct. 2008), pp. 1231–1237. ISSN: 00431648. DOI: 10.1016/j.wear.2008.01.037.

[48] K.-O. Edel. *Aus der Rollkontaktermüdung resultierende Lebensdauer von Eisenbahnschienen*. 2017.

[49] R.I. Carroll and J.H. Beynon. “Rolling contact fatigue of white etching layer. Part 2. Numerical results”. In: *Wear* 262.9-10 (Apr. 2007), pp. 1267–1273. ISSN: 00431648. DOI: 10.1016/j.wear.2007.01.002.

[50] S.L. Grassie et al. “Studs: a squat-type defect in rails”. In: *Proceedings of the Institution of Mechanical Engineers, Part F: Journal of Rail and Rapid Transit* 226.3 (2011), pp. 243–256. ISSN: 0954-4097 2041-3017. DOI: 10.1177/0954409711421462.

4

A TWIN-DISC STUDY ON SURFACE FRICTION AND SURFACE CONDITIONS OF RAILWAY STEEL UNDERGOING ROLLING CONTACT FATIGUE

Resurfacing of rails in railway tracks is a recurring maintenance activity to prevent rail damages from developing. The surface condition after resurfacing is completely different from the initial state. As soon as the first train wheels roll over, a breaking-in process begins during which geometric conformity and a stable coefficient of friction between train wheel and railway rail are achieved. This experimental study aims to compare the breaking-in behavior of five different surface conditions, which may be present after rail maintenance. For that purpose a twin-disc experiment was performed. The results show that the instantaneous coefficient of friction between the test disk and the counter disk, the load cycles until the first increase in the coefficient of friction and the levels reached, depending on the surface condition after resurfacing, show large differences. It is observed that deformation of surface roughness asperities facilitates fast contact surface formation and when wear of machined feed marks or strain-hardened material is required to achieve conformal contact, it takes much longer. Additionally, if the breaking-in process takes more load cycles, the risk of spall formation and the formation of a thick oxide layers increases. This study is a first exploration of the consequences of repetitive resurfacing and the subsequent breaking-in on the durability of the resulting contact surface that is formed.

This chapter is based on: B. Schotsman, M.J. Santofimia, R.H. Petrov, J. Sietsma, "A twin-disc study on the surface friction and surface conditions of railway steel undergoing rolling contact fatigue", submitted.

4.1. INTRODUCTION

Resurfacing of rails in railway tracks is a recurring maintenance activity to prevent rail damages to develop. This resurfacing is part of a planned preventive maintenance program designed to reprofile rails, to remove small dents and shallow damages, in order to avoid of rolling contact fatigue cracks to propagate. The typical technology employed for preventive maintenance is rail grinding, although the share of milling is rising. Milling is, for rail maintenance, a newer technology, typically used to remove larger damages, like cracks.

The resurfacing of rails, either by grinding or milling, results in a fresh rail surface of which the surface characteristics vary with the material removal, choice of abrasives, tool design, and tool wear.

With the first train wheels rolling over the freshly resurfaced rail, a process of breaking-in starts [1]. Breaking-in consists of simultaneously occurring processes to form a contact surface able to transfer traction forces of trains. During breaking-in the conformity of surfaces increases and a stable coefficient of friction between wheel and rail is reached [1, 2].

Processes at work to achieve geometric conformity are wear and deformation [1]. An important step in this is to reduce the surface roughness that has arisen during resurfacing. Akagai and Kato [3] have shown that one of the processes that causes roughness reduction is the plastic deformation of the asperities, named 'filmy wear'. Kapoor [4] has shown that slivers can be formed due to the presence of a contact stress concentration at the contact edges. Before Akagai and Kato [3] and Kapoor [4], Blau [5] already presented a cyclical deterioration model for unlubricated contacts, which describes the recurring processes at the surface. First plastic deformation of the surface and near subsurface takes place under ongoing deformation, causing the formation of flakes. Subsequently, the flakes are removed, and, as the remaining plateaus have to bear the load, these start to fracture as well.

The resurfaced rail may be partially coated with a hard and brittle white etching layer (WEL), which is the result of frictional heat generation at the tool tip or in friction zones of abrasives, and subsequent fast cooling [6, 7]. The presence of a WEL may retard contact surface formation, although evidence is limited and inconclusive. Mesaritis et al. [8] showed that most WEL fractures as a result of deformation in the wheel contact, and is subsequently removed. Nevertheless, it was also observed that the remaining WEL is enclosed in the contact surface, causing local stress concentrations [9, 10, 11].

The rise of the coefficient of friction requires removal of surface contamination and hydroxides before a protective oxide layer can form at the surface. This layer typically consists of hematite, α-Fe_2O_3 [12, 13]. Strain hardening associated with wear processes accelerates the formation of this surface oxide [14]. During the formation of the oxide layer, small, powdery wear particles are oxidized, while larger wear particles remain passive and are removed from the contact surface [14]. If contact conditions are such that the oxide layer is not formed or is fractured and removed, the surface may exhibit a high coefficient of friction resulting in catastrophic wear. [15].

Under specific conditions the oxide layer can develop into a 'marble cake', a mixture of oxides and partially oxidized wear debris [16] which contributes to the reduction in wear and friction coefficient [17]. Fretting, adhesive wear under small oscillatory move-

ments, which has a limited ability to remove wear debris, is such a condition [12].

Due to cyclic resurfacing, the contact surface must, after each maintenance cycle, be formed again. Although in the literature little evidence is found, it is expected that the load cycles required to form the contact surface will depend on the type of resurfacing operation and the typical surface condition.

To study the formation process of the contact surface under controlled conditions a twin-disc test setup is used. The use of frequency-controlled motor drives in the test setup allows for well-controlled, low-speed differences between the test discs, actually approaching the in-track conditions [18], and allow the assessment of the temporary friction coefficient between the two discs [2].

Several test setups have been developed and presented in the literature. These setups vary in test disc size, the geometry of the contact between the discs, and the option to introduce controlled lateral speed differences. Fletcher and Beynon [18] introduced the Sheffield University ROlling Sliding (SUROS) twin disc test setup. Ishida and Satoh [19] developed a test setup to reproduce specific shelling defects that have been observed in the Shinkansen lines, the Japanese high speed lines. In the current study the Dekra Rail test setup is used, which was constructed for research on wheel-rail-squeal noise control [20] and was later upgraded and modernized to study rolling contact fatigue development in rail steels [2]. With this setup it is possible to adjust the angle of attack, which introduces, similar to wheel-rail contact in curved track sections, lateral speed differences into the contact.

Twin disc tests machines are typically scaled models, and, for validly of the results, the physical laws involved need to be considered [2]. For test results to be representative of the full-scale situation, Jaschinsky [21] has determined that, for Hertz contacts and low speed differences, a similar ellipse ratio, a/b, with a being half of the contact width, and b half of the contact length of the contact ellipse, must appear in the contact in the full-scale test and the scaled test.

The research objective of this experimental study is to evaluate differences in breaking-in behavior between surface conditions that may initially be present as a result of recurring rail maintenance. The formation of the contact surface starting from the different surface conditions, the resulting surfaces and subsurface deformation, are studied. Representative contact stresses and speed differences for curved track sections were calculated using multibody simulations, and are applied.

4.2. MATERIALS AND METHODS

4.2.1. MATERIALS

Table 4.1 shows the chemical composition and mechanical properties of R370CrHT rail steel, as specified by the rail producer. This steel type was selected because it is the standard for curved track sections in The Netherlands. The combined carbon and manganese content of the steel results in a hypereutectoid composition [22]. To suppress the undesirable formation of pro-eutectoid cementite, silicon is added, which also contributes to the reduction of lamellar thickness.

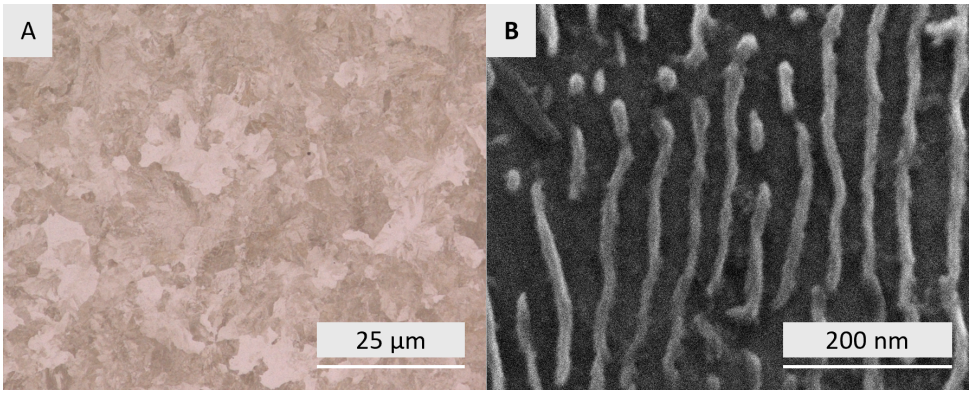

Figure 4.1: Pearlite microstructure of R370CrHT steel. A) Optical micrograph showing the equi-axed grains. B) Secondary-electron micrograph presenting the lamellar structure. The cementite lamellae appear light, the ferrite is dark.

Table 4.1: Chemical composition (in wt%) and mechanical properties as shown on the 3.1-materials certificate. The hardness is measured on the centerline of the rail head surface, as prescribed in the EN13674-1-standard [26].

	C	Mn	Si	Cr	Fe
Composition [wt%]	0.76	0.92	0.62	0.51	bal.
	R_m [MPa]	R_e [MPa]	ε [%]	Z [%]	Hardness [HBw]
Mechanical properties	1314	876	13.7	42.5	394

The rails were formed by hot-rolling, and were then air-cooled below the austenitic temperature, re-austenitized, and controlled accelerated-cooled to refine the lamellar thickness. The chromium addition influences the transformation kinetics, reduces the prior austenite grain size [23], and promotes α-formation in the steel, which results in a low subsurface hardness gradient. The hardness of the rail steel is 387 ± 3 HV1.

Figure 4.1 presents micrographs of the microstructure. Figure 4.1A shows the equi-axed grains and Figure 4.1B shows the lamellae in the pearlite microstructure. The pearlite colony size and lamellar thickness were determind using a mean linear intercept method [24, 25], and are 4.4 ± 0.5 µm and 81 ± 4 nm respectively.

The mechanical properties as presented in Table 4.1 were determined by the rail producer in a monotonic tensile test as prescribed by the EN13674-1-standard [26]. The ultimate tensile strength, R_m, was determined by dividing the maximum force by the undeformed transverse area of the tensile specimen. The 0.2%-offset yield strength, R_e, is the stress at which the 0.2% offset elastic strain intersects the stress-strain curve. The plastic elongation at fracture, ε, is calculated from the measured increase in length of the parallel section of the specimens, and the area reduction, Z, is calculated from the measured diameter in the necked area. The hardness is measured at the centerline of the rail head after removing 0.5 mm from the surface [26].

4.2.2. EXPERIMENTAL PROCEDURE

The objective of the experiment is to study the course of breaking-in of various initial surface conditions. For this purpose, an experiment was designed in which, using a conditioned test setup with two discs, and a predefined contact pressure and tractive shear stress are exerted on the disc surface, which are representative of the conditions on track.

First, the contact pressure is calculated. Hiensch and Steenbergen [27] performed multibody simulations to determine the mean contact pressure and slip for passenger trains rolling through a 1200 m radius curve. The simulation showed that a mean contact pressure of 1050 MPa, a 2 mrad yaw angle, and a a/b-ratio of 2.7 are expected. The 2 mrad yaw angle causes a lateral slip of $\gamma_y = \tan\phi = v_Y / v_X = 0.20\,\%$ in the contact zone [28], with v_Y the speed of the wheel in Y-direction, and v_X the speed in X-direction.

Schotsman [29] performed similar multibody simulations for a case study, using the actual track design and train speeds. The track section has a curve radius $r = 2257$ m and a 2‰ slope. The calculated mean pressure, p_m, on the new UIC 54E5-profile [26] is $p_m = 1265$ MPa and on the measured profile is $p_m = 643$ MPa. The calculated a/b-ratios were 1.66 and 0.83 for the new and measured profiles, respectively.

Table 4.2 presents the material and the geometry of the test disc and the contra disc. The geometry is defined by the disc radius, r_x, and the radius of outer surface, r_y. The normal force, exerted on the disc, $F_N = 900$ N, results in a mean contact pressure of $p_m = 0.93$ MPa.

Table 4.2: The design of the test disc and the contra disc, the normal load, and the resulting contact pressure for the selected disc geometries.

	Material	Disc geometry	Loading conditions	
Test disc	R370CrHT	$r_{x1} = 78.5$ mm	F_N	900 N
		$r_{y1} = 10$ mm	Mean contact pressure	0.93 MPa
Contra disc	C45-steel	$r_{x2} = 240$ mm	Von Mises stress (max)	0.82 MPa
	(material nr. 1.0503)	$r_{y2} = \infty$		

Tractive wheels of trains, rolling over rails, rotate, as a result of the applied driving force, slightly faster than expected given the train's forward speed. A traction curve describes the relation between the level of slip, and the traction coefficient, defined as the traction force, F_M, divided by the normal force, F_N [30]. During breaking-in, traction curves typically shift to lower levels of slip. Low levels of slip are associated with a low wear rate and low heat generation, whereas situations with slip saturation, the wear rate and heat generation may be high.

Because of the aforementioned characteristics, the experimental procedure is divided into two stages. During the first stage, until the coefficient of friction between the discs has increased and a steady state is reached, the traction force F_M is controlled and the slip velocity is regulated to be below 0.6 %.

In the second stage, the procedure developed by Hiensch and Burgelman [2] is applied. Hiensch and Burgelman used Burstow's wear function to determine the traction forces. Burstow [31, 32] introduced an empirically determined function consisting of shear force, here represented as F_C, and slip, γ, in the wheel-rail-contact.

$$F_C\gamma = F_{Cx}\gamma_x + F_{Cy}\gamma_y + F_C\psi, \tag{4.1}$$

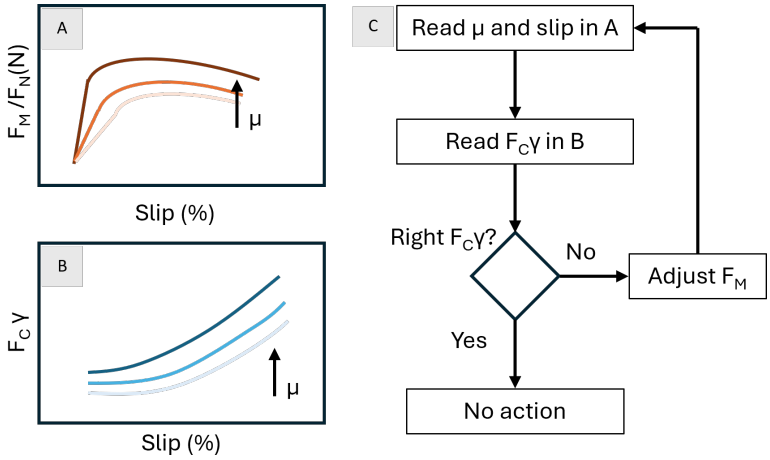

Figure 4.2: Scheme to control the test condition $F_C\gamma$ in the second stage of the test. A) The Kalker Fastsim simulation provided the relation between the traction coefficient, F_M/F_N, and longitudinal slip for various values of μ. B) The Kalker Fastsim simulation also provided the relation between $F_C\gamma$ and longitudinal slip for various values of μ, provided the 2 mrad yaw angle. C) Procedure to regulate $F_C\gamma$ within the predefined value ranges.

with F_C being the creep force, γ_x the longitudinal slip, γ_y the lateral slip, and ψ the spin. The function was developed for R220-rail steel and is widely used in the railway industry to predict the number of load cycles until rolling contact fatigue crack initiation. It has recently been calibrated for R370CrHT rail steel by Hiensch and Steenbergen [27].

Kalker Fastsim wheel-rail simulations [33] were made for the experiment to establish the relations of tractive force relative to the normal force, F_x/F_N, $F_C\gamma$ and slip for coefficients of friction between both discs ranging from $\mu = 0.10$ to 0.40.

Figure 4.2 shows the schematic representation of the procedure for this second stage, to regulate $F_C\gamma$-value once the coefficient of friction is stabilized and $F_C\gamma$ is expected to fluctuate only mildly. Figure 4.2A shows that first the coefficient is read from the graph. Then the actual $F_C\gamma$ can be read from Figure 4.2B. F_M is adjusted to bring $F_C\gamma$ to the predefined level.

The test performance is divided into separate runs of 3000 to 6000 load cycles. Before and after each run, the disc surface is cleaned using a degreasing agent. Prior to the test start a calibration run is performed to set the differential circumferential speed readings of both discs to zero. This calibration run of much less than 1500 cycles, is short. The roughness of the contact surface is measured without removing the disc from the test setup. Measurements were performed according to the EN-ISO4287-standard [34] using a Mitutoyo SJ210 portable surface roughness tester on a fixed support. A magnifier is used to observe the contact surface of the test disc and to take photographs using a 64-megapixel camera. Before stopping a run, within the last 500 load cycles, the actual normal force, F_N, torque, M, and slip were recorded.

4.2.3. TEST SPECIMENS

Figure 4.3 presents the rail profile and the extraction position of the test discs. Figure 4.3A shows the rail profile in cross-section containing a test disc that covers the full height. A larger disc radius results in a larger contact surface and the results are therefore less sensitive to wear [2, 35]. The test discs were produced by hard turning after the removal of both sides of the rail foot and rail head.

Figure 4.3B presents the resulting disc. The hub is welded onto the disc before finish turning to obtain the required dimensional tolerances and proper fitting in the test setup.

Different cooling rates, a result of the section area differences within flat bottomed rail profiles, results in hardness differences. These hardness differences, by the choice in disc design, are present at the disc surface. It is assumed that, due to the low slip rate and short test duration, any wear differences will not affect the test result. An assumption that was also made by Hiensch and Burgelman [2].

To avoid assessing the contact surface containing impurities, which are more frequently present in the rail web, only observations from the rail head section of the disc are presented in this study.

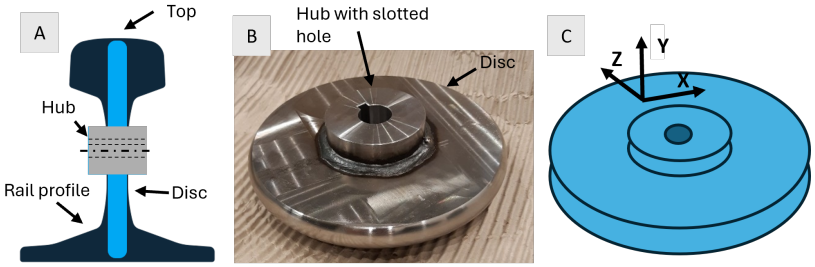

Figure 4.3: Schematic representation of the rail profile and test disc. A) Test disk made from the full height of the rail profile, shown in the rail profile with a slotted hole hub, which is welded onto the disk to mount it in the test frame. B) A test disc with a hub with slotted hole. C) The local coordinate system that is used in this study.

4.2.4. TWIN-DISC TEST SETUP

Figure 4.4 shows the schematic representation of the test setup, the free body diagram of both discs, and the mechanically enforced angle of attack. Figure 4.4A presents the main elements and controls. The test disc and contra disc are mounted on drive shafts of separate AC-motor drives. The rotational velocity of both motors is measured using encoders mounted on the driveshafts and independently regulated by variable frequency AC motor speed controllers. The motor torque is measured using torque transducers on the driveshafts.

Figure 4.4B presents the free-body diagram of the discs. The test disc is mounted on a movable latch, to allow for the movement to introduce normal force, F_N. The tractive force exerted on the contact surface is generated by braking of the test disc motor.

Figure 4.4C presents the mechanically enforced disc alignment. The test motor frame is rotated to introduce the necessary angle between the discs.

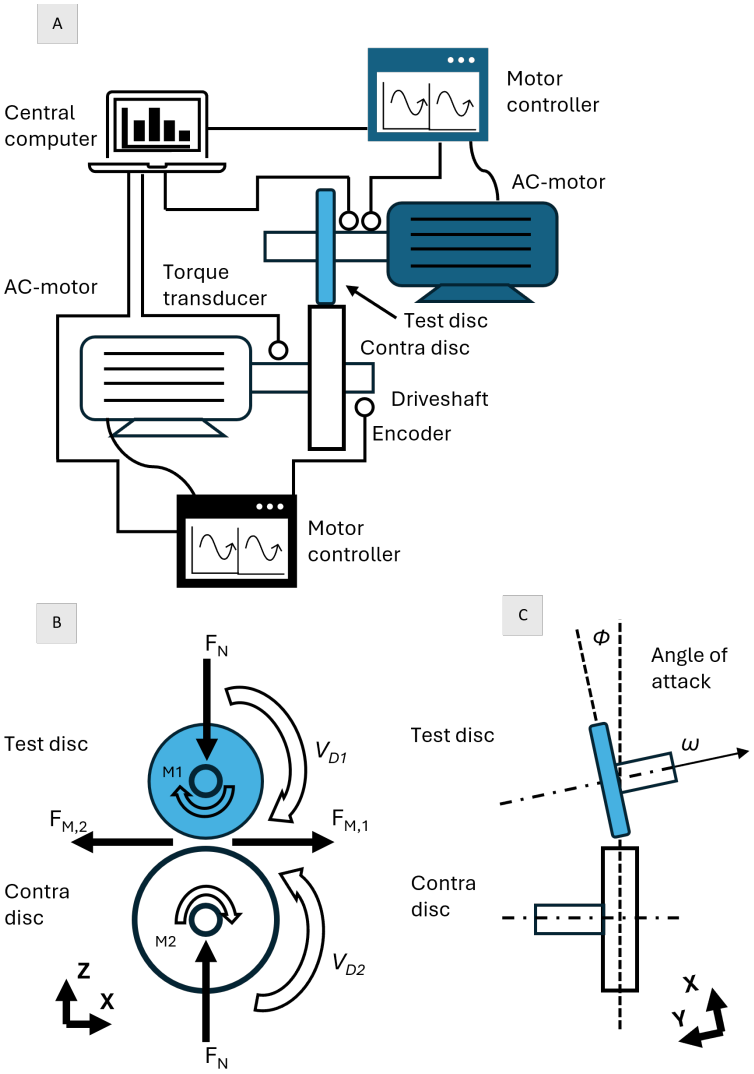

Figure 4.4: Schematic representation of the twin-disc test setup. A) Test setup with the test disc in blue and the contra-disc in white. Both AC-motors are independently frequency-controlled, and the rotational velocity and torque are measured at both drive shafts. B) Representation of the test disc, 1, and contra disc, 2, with normal force, F_N, torque, M, resulting traction force, F_M, and rotational velocities of the discs, V_D. C) The 2 mrad misorientation causes lateral speed difference representative for the angle of attack of a vehicle bogey in a R = 1200 m radius curve.

4.2.5. APPLYING DISTINCT SURFACE CONDITIONS FOR INVESTIGATION

Resurfacing the rail using different maintenance methods and strategies will result in different surface characteristics. The five surface conditions, representing different rail maintenance procedures, evaluated in this study are:

- The hard turned, HT, surface condition. This is the surface condition of the as produced test disc.
- The transversely, in the Y-direction, brushed, TB, and longitudinally, in the X-direction, brushed, LB, surface condition. These surfaces were prepared by brushing the disc surface using a grit size #60 sanding belt on the discs mounted on a turning lath.
- The machined surfaces, M and AM. The surfaces were prepared using a cutting tool made of HSS-C05-steel. The cutting tool has a relief angle of 7° and a 3° back rake angle. The disc curvature was ground in the tool to introduce a machined surface without changing the disc geometry. A cutting speed of 100 m/minute has been used. The M surface was prepared by applying hard turning. From the AM surface, which was annealed at 500°C for 4 hours, and after annealing straightness deviations were removed by the machining. The subsurface deformation of surface AM has not been assessed.

Table 4.3 shows characteristic aspects of the surface conditions. The surface roughness is measured in the X-direction of the surface using a Mitutoyo SJ210 surface roughness tester. The WEL thickness and the deformation depth were measured on the transversely sectioned specimens, outside the area affected by the contact, using a Keyence VHX5000 microscope. The depth of deformation is defined as the maximum distance to the surface at which unidirectionally sheared lamellae were observed.

Table 4.3: Characteristic aspects of the surface conditions that were evaluated in this experimental study.

Surface condition	Abbr	Visual appearance	Surface roughness R_a (µm)	Deformation depth (µm)	White layer (µm)
As produced	HT	Shiny surface Repetitive pattern of feed marks	0.12 ± 0.01	15	1.5
Brushed, transverse	TB		1.1 ± 0.1	15	1.5 (flakes)
Brushed, longitudinal	LB		0.37 ± 0.05	15	1.5 (flakes)
Machined	M	Dull surface Ridges as a result of tool vibration.	2.3 ± 0.3	19-33	0
Annealed, Machined	AM		1.7 ± 0.1	Not measured	Not measured

4.2.6. PROCEDURE FOR THE CHARACTERIZATION OF THE SURFACE AND MICROSTRUCTURE AFTER TESTING

Specimens for detailed surface and microstructure analysis were cut from the test discs using a Struers Discotom-6 cut-off machine equipped with a ceramic blade. All specimens were mounted with Struers Polyfast and heated and pressed according to the specification of the producer. The surfaces were then prepared using SiC-paper with #80-#4000 grit size and polished with 3 µm and 1 µm diamond polishing fluid.

To determine the hardness of the microstructure a Struers Durascan 70 hardness tester was used, before etching with nitric acid diluted with ethanol to 2 vol% (Nital), for 10 seconds.

The microscopic observations were made using a Keyence VHX5000 microscope and a Jeol JSM 6500F scanning electron microscope, with an acceleration voltage of 15 kV and 9.5 mm working distance, in secondary electron imaging detection mode.

The Energy-dispersive spectroscopy (EDS) observations of oxides that were formed at the running surface, were made using a 10 mm^2 SSD detector from Thermo Fisher mounted on the Jeol microscope.

X-Ray diffraction analyses (XRD) were performed to analyze the crystallographic structure at the contact surface. For these observations a D8 Discover diffractometer, with a Incoatec Microfocus Source (IμS), at 50 kV, 1000 µA, producing Cu Kα radiation, is used. The system is further equipped with Montel Optics ELM32 with parallel beam and a UBC collimator of 1 mm.

4.3. RESULTS

4.3.1. BREAKING-IN

Table 4.4 present the summarized results for the five surface conditions of the experiment. The second column shows the number of load cycles at which the contact surface has developed to the point where the coefficient of friction increases noticeably. A rapid increase, from its instantaneous level to its initial peak, is observed for all surfaces once the rise sets in. This initial peak value is defined as the maximum coefficient of friction, μ, that is observed in the test run in which the rise takes place.

From this transient phase onward test control shifts to the second phase. The test is performed in the linear section of the traction curve, where an increase in F_M results in a small increase in slip. Columns 4 and 5 show the observed maximum and the average value of the coefficient of friction during the test. The standard deviation of the average shows that the variation in friction is small.

The test duration in column 6, expressed as the total number of cycles, is different for each surface condition, and, especially for AM and LB surface conditions, longer. The short runs and low total number of cycles in the test of the HT, TB, and M surface conditions better serve the objective to study the surface condition-specific contact surface formation, whereas the longer test durations are better suited to study rolling contact fatigue damage initiation.

The correlations in the small data set resulting from the experiment were determined to explore the relationships. The number of cycles until the shift in the traction curve takes place and the initial rise of the coefficient of friction sets in, and the maximum

friction coefficient has a correlation value of −0.78. This correlation suggests that the faster after the start of the test the friction increases, the higher it will become. A correlation value of −0.81 is calculated for the relation between the measured valley depth, R_v, when the rise of the coefficient of friction sets in, and the level that is achieved. R_v has a stronger relation with the coefficient of friction than R_a and the correlation suggests that a larger valley depth results in a lower value.

Table 4.4: The summarized results of the experiment with different surface conditions.

Condition	Initial rise (cycles x10^3)	Initial peak value of μ	Maximum μ (at cycles x10^3)	Average μ (st dev)	Total cycles (x10^3)
HT	18	0.27	0.30 (27)	0.29 ± 0.09	27
TB	from start	0.40	0.40 (3)	0.29 ± 0.09	12
LB	9	0.19	0.30 (328)	0.23 ± 0.05	378
M	27*	0.16	0.18 (43)	0.17 ± 0.01	83*
AM	7.5	0.23	0.27 (100)	0.24 ± 0.02	150

* Which includes 12000 cycles of rolling to generate a coefficient of friction sufficient to start the test.

4.3.2. SURFACE EVOLUTION OF THE HARD TURNED SURFACE (HT)

This section presents the contact surface formation and subsurface deformation of the HT surface condition. Therefore Figure 4.5 shows the surface roughness evolution and the development of the coefficient of friction during the test, with optical micrographs of the fresh surface condition before the test at one side and the surface condition at 24×10^3 load cycles at the other.

The fresh surface in Figure 4.5A shows the characteristic parallel feed marks of hard turning. The feed mark depth ranges from 1.5 µm to 4 µm and the width from 119 µm to 129 µm. The average surface roughness, measured in X-direction, is $R_a = 0.119$ µm.

The contact surface in Figure 4.5B after 24×10^3 load cycles consists of two bands with different surface characteristics. A band with a smooth surface, see i, and one with a rough surface, see ii. Darker areas on the rough surface are valleys where material was spalled off, lighter areas are probably wear slivers that are still attached to the surface. The fact that the different surface characteristics are visible next to each other is the result of the 2 mrad angle of attack causing a parallel stick zone and slip zone in the contact.

The graphs in Figure 4.5C present the evolution of surface roughness and coefficient of friction as a function of the number of load cycles. Each dot in the graph represents a stop between runs to characterize the transient surface condition. The surface roughness decreases slightly at first, as a result of contact surface formation, while the coefficient of friction is constant. The latter starts to rise at 18×10^3 load cycles and the increase continues into the next test run, but the rate of increase slows down. The surface roughness also increases, but unlike the coefficient of friction, the roughness increase accelerates.

Figure 4.6 presents a micrograph of the HT contact surface condition for the detailed observation of the contact surface after the test. The test duration was kept short at 27×10^3 load cycles to avoid losing interesting features due to wear. The contact width is

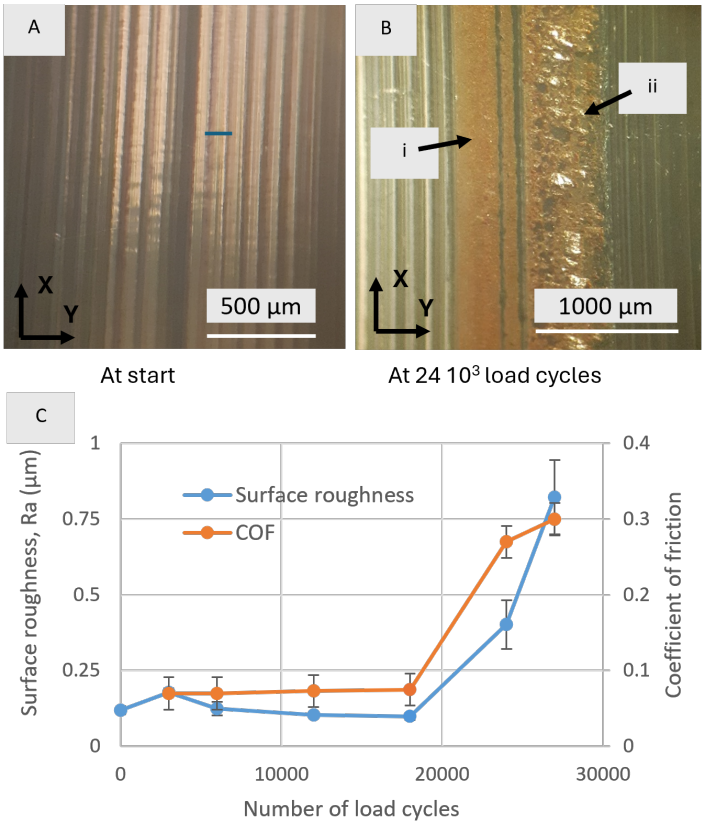

Figure 4.5: The contact surface formation at the HT surface condition. A) The fresh HT surface with characteristic feed marks and ridges on both sides. B) The surface condition at 24×10^3 load cycles, consisting of a smooth band, see i, and a rough band, see ii. Both bands are separated by remaining feed mark valleys. C) The evolution of the surface roughness and the coefficient of friction as a function of the number of load cycles.

~960 µm and divided into two bands. The $-Y$-side of the contact surface is characterized by a straight side, caused by the feed mark, a reddish surface, an indication of ferro-oxide presence, and spallation of material. The larger spallations have a ~30° angle to the Y-axis, and the smaller spallations align with the parallel wear scars having a ~48° angle to the Y-axis. The band at the right, the Y-side, the contact surface is darker, and material spallations are localized.

Until this point, only surface observations have been presented. Figure 4.7 shows the HT surface in cross-section to study the contact surface characteristics and compare these with the fresh surface condition outside the contact surface. The feed mark in Figure 4.7A has a semi-elliptical shape and is bordered by ridges on both sides. Material is strained as a result of rubbing of the cutting tool. The heat generation caused a 1.5 µm WEL on the top of the ridges. The maximum depth of deformation is 15 µm and the feed mark is filled with oxidation products.

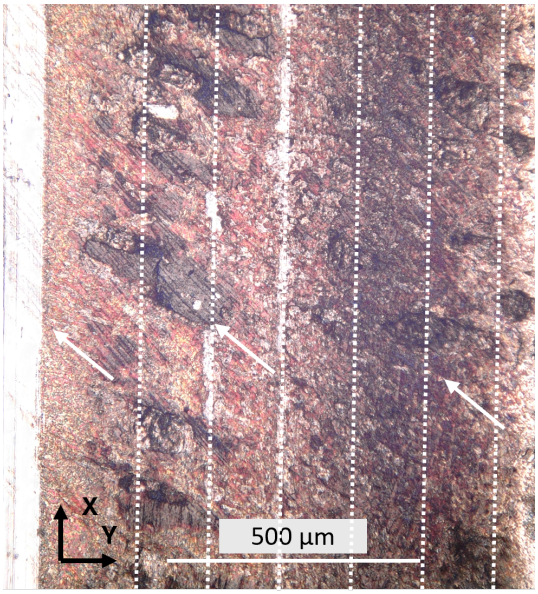

Figure 4.6: The contact surface, that was formed on the HT surface condition, after the test. The white arrows indicate the sharp edge of the contact surface and spallation of material. Spallation takes place at a ~30° angle and a ~48° angle. This second orientation coincides with the wear scratches at the surface. The ridges in the cavities, the result of material spallation, might be propagation marks. The dashed vertical lines indicate the former feed mark positions.

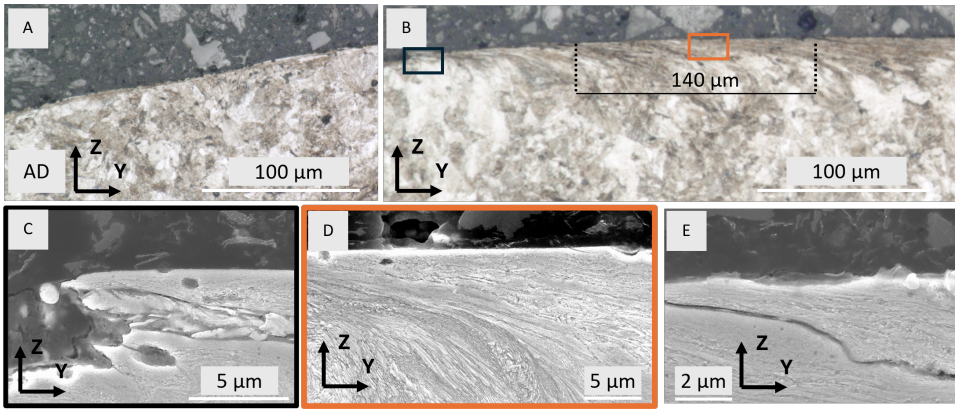

Figure 4.7: The characteristics of the HT surface condition before and after the test in cross-section. A) The feed mark at the hard turned surface with ridges on both sides. B) The contact surface with surface-initiated damages at mutual distances of 100 µm to 140 µm. C) Material deformation and fragmentation at the contact extreme. D) Deformation below the contact surface. E) Damage initiation between strained lamellae at the center of the contact surface.

Figure 4.7B shows the $-Y$-side of the contact surface, which is flattened by deformation and wear. The maximum depth of deformation close to the contact extreme is 35 µm. Surface-initiated damages, with a mutual distance of 100 µm to 140 µm, are present.

Figure 4.7C shows the strained and detached material at the contact extreme. Fractured fragments are still present.

Figure 4.7D presents the contact surface and the subsurface deformation. Lamellae are strained to become parallel to the surface. The deformation orientation, in $-Y$-direction, is determined by the shear orientation at the surface. At the center of the contact surface, several damages are observed to have initiated within the strained lamellar structure. An example of such an initiation is shown in Figure 4.7E.

4.3.3. SURFACE EVOLUTION OF THE BRUSHED SURFACES (TB AND LB)

The results for both brushed surface conditions are considered in the same section and presented in a similar manner to the HT surface condition. Therefore Figure 4.8 shows the development of the coefficient of friction and the roughness evolution of both surface conditions, with optical micrographs of the surface conditions on both sides.

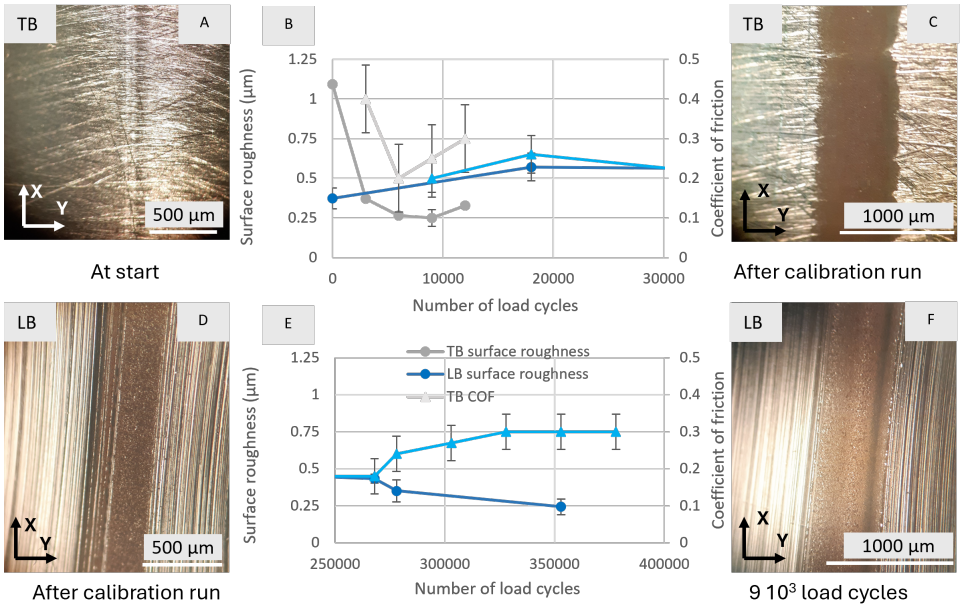

Figure 4.8: The contact surface formation at the TB and LB surface conditions. A) The freshly brushed TB surface. B) The evolution of surface roughness and coefficient of friction as a function of the number of load cycles. C) The contact surface on the TB surface condition after the calibration run. D) The contact surface at the LB surface condition. E) The evolution of surface roughness and coefficient of friction during the last part of the test. F) The contact surface at the LB surface condition at 9×10^3 load cycles.

The freshly brushed TB surface in Figure 4.8A is characterized by the transverse grooves applied by brushing, removing most of the feed marks, some of which are still present at the centerline of the disc. The average surface roughness of the surface is $R_a = 1.1 \pm 0.1\,\mu m$.

The instantaneously high coefficient of friction, shown in Figure 4.8B, is a specific characteristic of the TB surface condition. This coefficient decreases and starts to rise again, but not to the initial level within the duration of the test. The roughness measurements show a fast reduction at first and a slight increase towards the end of the test.

The brown-colored contact surface in Figure 4.8C is immediately formed, already during the short calibration run and is slightly darker at the Y-side, but no clear bands are present.

Figure 4.8D presents the LB surface condition which is characterized by fine parallel grooves and remaining feed marks in the X-direction. The surface roughness before the start of the test is $R_a = 0.37 \pm 0.05\,\mu m$.

Figure 4.8B shows that the surface roughness of LB increases slightly during contact surface formation until 18×10^3 load cycles are reached. The coefficient of friction starts to rise at 9×10^3 cycles its first peak is lower than for the TB surface condition.

The contact surface on LB in Figure 4.8F has straight sides and, at the Y-side of the contact, wear slivers are present. The coloration varies. A darker zone is present in the center of the contact surface and an even darker zone with a small width at the Y-side. The LB test was extended to 378×10^3 load cycles, as is shown in Figure 4.8E. From 268×10^3 the friction coefficient starts to rise to 0.30, while at the same time the surface roughness continues to decrease.

Figure 4.9 shows the contact surfaces after the test formed at both TB and LB surface conditions. Three characteristic aspects of the TB contact surface in Figure 4.9A are briefly mentioned. First, the contact surface has an average width of ~1070 µm and the contact width variation is still present. The locations with small width are accompanied by the presence of deep grooves adjacent to them, which are also visible in the contact surface itself. Both observations evidence that material deformation contributes to the fast formation of the load-carrying surface. Second, several damages are present, some of which are highlighted in the Figure. Finally, the contact surface is divided into two bands; a small red to brown band with a smooth surface and a wide darker brown band. Differences in color and texture indicate differences in contact conditions.

The LB contact in Figure 4.9B, as a result of the test duration and associated wear and deformation, is wider than the contact on TB. Four bands are indicated with i to iv. The surface indicated with i is only lightly touched and longitudinal grooves are still present. The central part of the contact surface is ~ 1000 µm wide and has a red-brown, see ii, to brown, see iii, surface. Specific for iv is the visually observable higher roughness. The blueish temper color outside the contact surface, evidences the temperature that is reached during brushing.

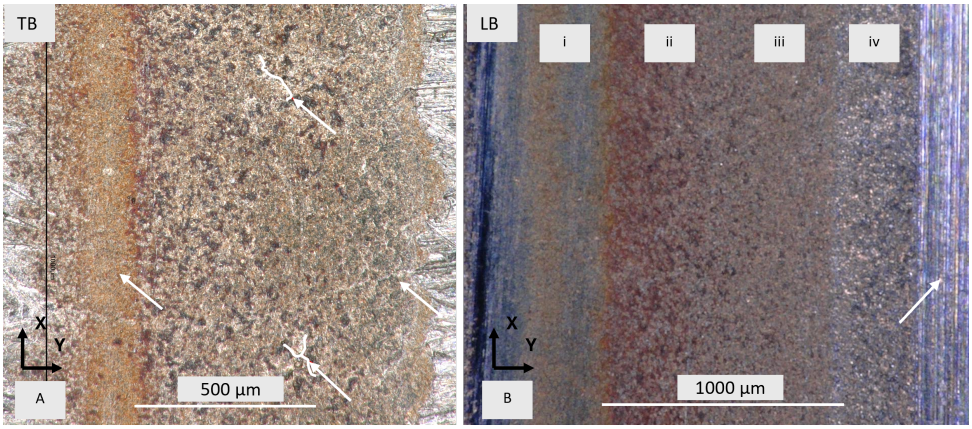

Figure 4.9: The contact surfaces that were formed. A) The contact surface on the TB surface condition, after 12×10^3 load cycles. At the contact surface two bands are observed. The deep grooves next to the contact surface are also visible in the contact. Several damages are present. B) The contact surface on the LB surface condition, after 378×10^3 load cycles. Four bands are indicated with i to iv, having different surface characteristics. The brushed surface shows blueing.

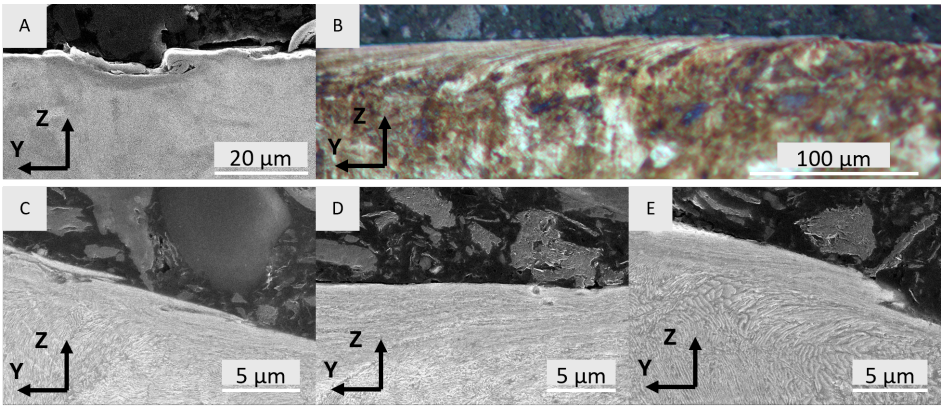

Figure 4.10: The characteristics of the TB surface before and after the test. A) The fresh surface with a furrow, formed by transverse brushing. B) The contact surface, C) The fresh surface outside the contact, with deformed and submerged material. D) Deformation of the running surface, E) Contact surface widening by the deformation of material at the contact extreme.

Cross-sections of the TB surface condition were made to evaluate the initial surface condition and the characteristics of the contact surface after the test. Figure 4.10A presents, outside the influence of the wheel contact, a furrow that was formed during brushing. Chips of material are removed but some of the slivers stay attached.

Figure 4.10B shows an optical micrograph of the transition between the contact surface and the freshly brushed surface. The depth of deformation is 37 and damages are present with a maximum depth and length of 8 and 37, respectively.

Figure 4.10C presents a second micrograph of the surface outside the contact zone showing that material is folded and deformed during brushing which caused deformation to a depth of ~ 3 µm.

In the contact area lamellae are strained to become parallel to the contact surface even after 12×10^3 load cycles, the lowest number of all tests, Figure 4.10D.

Figure 4.10E presents a detail of the contact surface extreme in cross-section. The ~2 µm thick severely deformed layer of material is pushed towards the side, widening the contact. The frayed edges evidence the rupture of lamellae.

4.3.4. SURFACE EVOLUTION OF THE MACHINED SURFACES (M AND AM)

Figure 4.11 shows the contact surface of both machined surface conditions, M and AM. The graph presents the evolution of the surface roughness and coefficient of friction, and micrographs at both sides present the surface condition at the start of the test and after 27×10^3 and 7.5×10^3 load cycles, respectively.

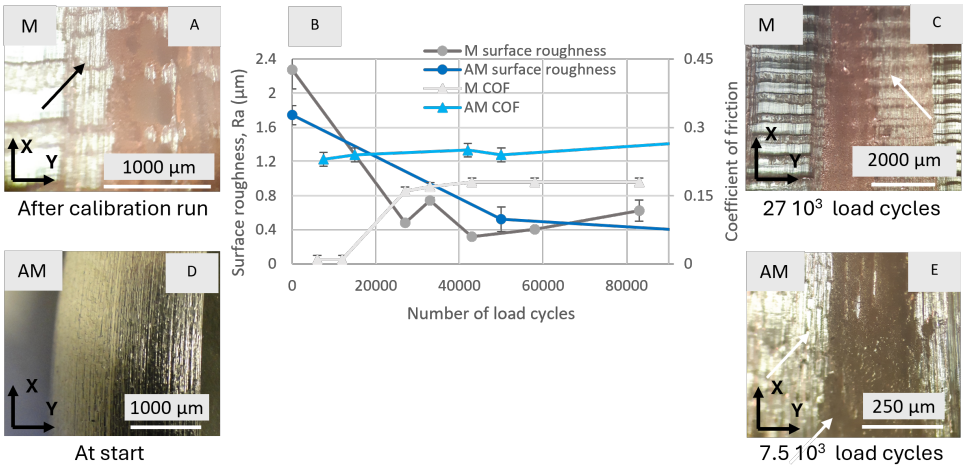

Figure 4.11: The contact surface formation at the AM and M surface conditions. A) The M surface condition after the calibration run. The wear scars are present between the repetitive surface pattern and the, partly formed, brown-colored patches. B) The evolution of the surface roughness and the coefficient of friction of both the M and AM surface condition as a function of the number of load cycles. C) The contact surface that is formed on the M surface, at 27×10^3 load cycles. D) Optical micrograph of the freshly machined AM surface condition. E) The contact surface that is formed on the AM surface at 7.5×10^3 load cycles. At the contact surface are bands and wear slivers visible.

Figure 4.11A shows the surface of the M surface after the calibration run. The repetitive pattern has a ~600 µm peak-to-peak distance, caused by tool vibration during application of the surface condition. The surface roughness is R_a = 2.28 ± 0.22 µm. The contact surface consists of non-connected, brown-colored patches with partially worn ridges at the side.

The coefficient of friction between the M surface and the contra disc is initially low, lower than for the other surface conditions, and it takes 24 × 10^3 load cycles to rise. To form a contact surface, 12 × 10^3 load cycles were performed without the application of traction forces. This was because transmission of traction forces was not possible without causing excessive slip between the discs. The coefficient of friction reaches a plateau of 0.18 after 43 × 10^3 cycles, as shown in Figure 4.11B.

Figure 4.11C presents the contact surface which forms a, virtually, continuous brown band. Ridges are still present and the contact surface between these ridges is wider. Next to the brown contact band, at the Y-side, wear scars are present, evidencing contact with the contra-disc.

The optical micrograph of the AM surface in Figure 4.11D shows the general surface condition resulting from machining. The surface is characterized by feed marks, deformation, and roughening. The surface roughness is R_a = 1.74 ± 0.11 µm.

The coefficient of friction rises earlier and reaches a higher value compared to the M-surface condition, as is shown in Figure 4.11B, The contact surface is dark brown in color, and, typical for the AM surface, consists of longitudinal bands with wear slivers. The bands are separated by deeper ridges, as shown in Figure 4.11E.

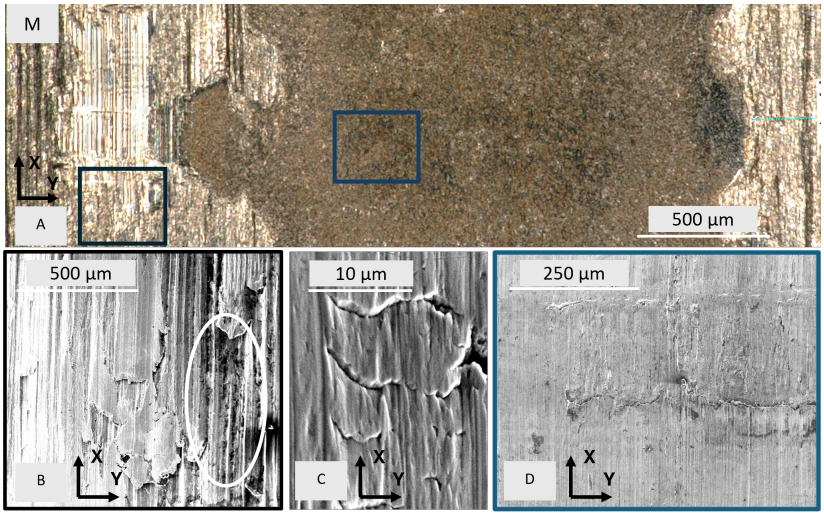

Figure 4.12: The surface characteristics of the contact surface formed from the M surface condition, at 83 × 10^3 load cycles, after the test. A) Contact surface with the machined surface at both sides. The colored frames are locations of detailed observations. B) SEM observation of the freshly machined surface showing sliver formation, which is the result of cutting and rubbing. Oxidation products are observed on the cutting ridges, highlighted by a white ellipse. C) SEM observation of the machined surface in detail. D) SEM observation of the contact surface developing damage at the remaining transitions in height.

Figure 4.12 shows the surface of the M surface after the test to evaluate the fresh surface and the contact surface that was formed. No detailed analysis of the AM surface condition, such as analysis of the contact surface that was formed and metallographic examination, was made.

The average width of the brownish contact surface in Figure 4.12A is ~1600 µm. Both sides show a repetitive wavy pattern with a ~600 µm peak-to-peak distance, corresponding with the ridge distances.

Figure 4.12B presents the characteristics of the freshly machined surface in the black-framed area in Figure 4.12A. The machining resulted in extruded sliver formation on the surface. The ~130 µm wide feed marks are remnants of the initial surface, showing oxidation.

Figure 4.12C presents the side of the contact where slivers have formed separated blocks of deformed material.

The repetitive patterns appear to have worn away from the contact surface. However, in SEM images, as shown in Figure 4.12D, these valleys and hills are still visible. Damage initiates at the transitions between the locally remaining height differences.

Figure 4.13 presents the M surface condition in cross-section with in Figure 4.13A the surface condition outside the influence of contact. Extruded slivers appear as localized patches of strained material in the cross-section.

Figures 4.13B-E show the contact surface and details thereof. The pearlite lamellae are strained to become parallel to that surface and, at the extreme of the contact, material covers the ridge that is present, as is shown in Figure 4.13B. The maximum depth of deformation is 50 µm. The detail in Figure 4.13C presents the contact extreme which shows that the material is deformed and fractured and that some of the detached particles are still present.

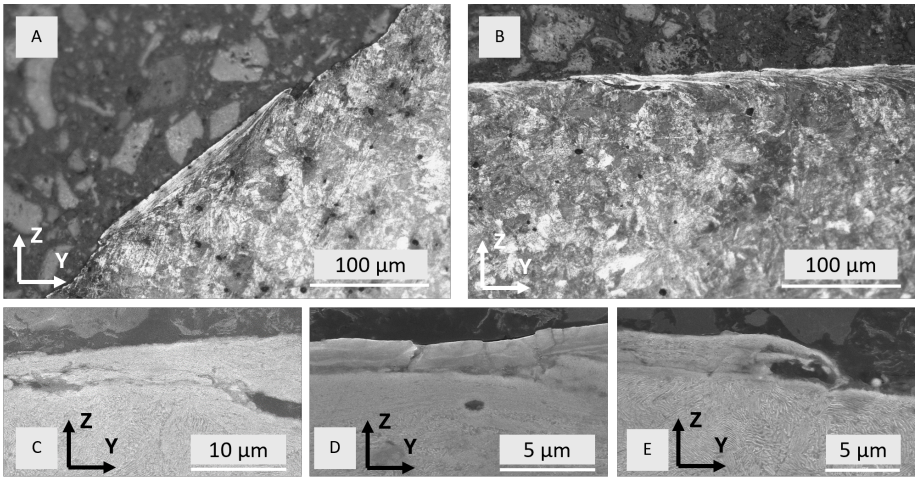

Figure 4.13: The characteristics of the M surface before and after the test in cross-section. A) The fresh M surface with deformation caused by machining. B) The contact surface. C) Material extruded at the contact surface covering a groove. D) Oxide presence in the contact surface. E) Widening of the contact surface by material deformation at the contact surface extreme.

Figure 4.13D shows that oxidized particles are formed. The formation of a 2 µm to 5 µm thick iron-oxide-layer is confirmed by EDS-analysis and is specifically different from the other surface conditions that were tested. At the contact extreme, similar to the other surface conditions, is material extruded, as is shown Figure 4.13E.

Red to brown coloration of the contact surface is associated with iron-oxide formation. XRD-characterization was performed to determine the oxide configuration. Figure 4.14A shows the specimen on the samples stage and Figures 4.14B and 4.14C the observation positions at the brown colored part of the contact surface and at the dull part, where wear tracks are present. The analyses of the diffraction patterns, see Figure 4.14D, confirmed the presence of oxides in the brown area. The oxides were identified as hematite, α-Fe_2O_3. WEL was not observed in the cross-sectional analysis, however the diffraction pattern of the XRD scan was examined for the present of residual austenite, to see whether it could still be present. The analysis did not reveal such presence at both positions.

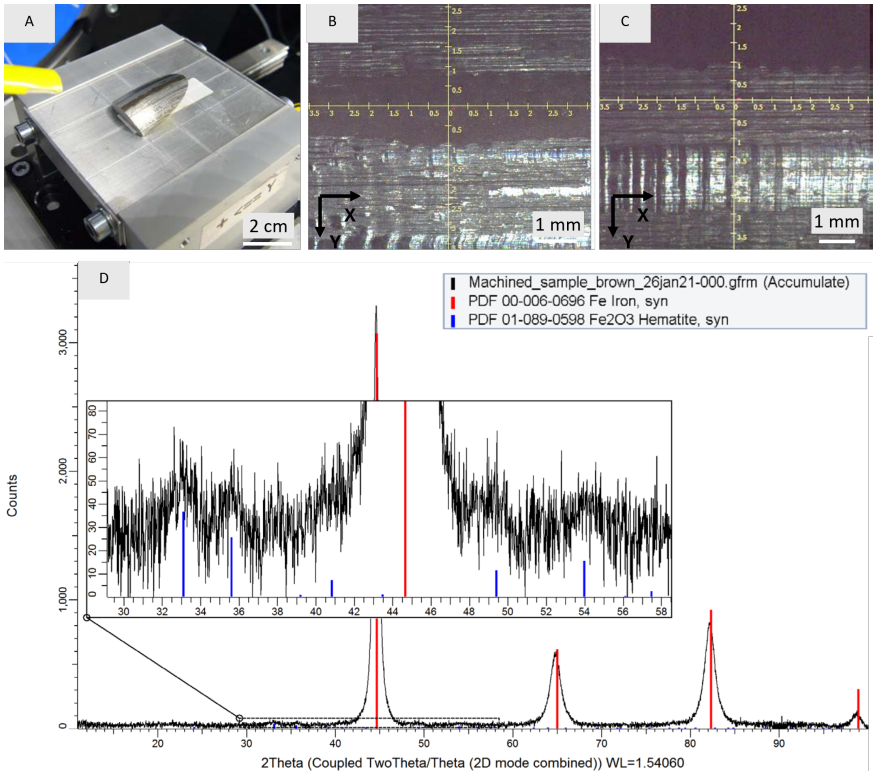

Figure 4.14: XRD analysis of the contact surface at M surface. A) The specimen at the sample stage. B) Observation position at the brown part of the contact surface. C) The observation position at the dull part of the contact surface. D) The diffraction pattern with in red the expected peaks for Fe and in blue for α-Fe_2O_3, hematite.

4.4. DISCUSSION

The formation of the contact surface of five different surface conditions was studied to determine the differences in the breaking-in process of freshly resurfaced rail surfaces. Surface oxide layer formation, transient behavior of the coefficient of friction between both the test disc surface and the surface of the contra disc, and the differences between the contact surfaces that are formed, are discussed.

4.4.1. OXIDE FORMATION AT THE CONTACT SURFACE

The contact area of the test disc immediately turns red-to-brown, independent of the initial surface condition and even before the coefficient of friction rises. This coloration is the result of oxide formation at the surface.

The dominant iron-oxide that is formed at ambient temperatures is hematite, α-Fe_2O_3, [12, 13, 36]. The presence of which was confirmed for the M-surface condition.

When the test lasts longer, the surface coloration becomes paler or locally brighter which is a result of changes in the wear rate once the contact surface has formed. Kortüm [37] found that the coloration of oxide layers is predominantly determined by particle size and Torrent & Barrón [36] showed that oxide coloration becomes paler with oxide particle size reduction.

Surface wear and the rate of deformation, at start of the test, are high and wear debris is formed. A reduction in wear rate, as a result of the reduction of asperity contact and the built-up of a protective oxide layer, results in smaller wear particle size and therefore oxide particle size.

A concise evaluation of the HT, TB and M surface conditions shows that:

- The contact surface at the HT surface initially turns red to brown and develops to a paler coloration, as observed during the test performance.
- The TB surface condition is initially dark brown and gradually becomes pale. A distinct band with a different color develops at the contact surface, and, based on the results by Torrent & Barrón oxide particles are locally larger [36].
- The contact areas at the ridge tops of the M surface are, initially, red. Once the contact surface is formed, these develop to brown.

The surface condition formed at the M surface is, at the micro-scale, different compared to the HT and TB surfaces. Specifically at the M contact surface a 2 µm to 5 µm oxide layer is formed. The formation is the result of an enduring wear process and insufficient removal of wear debris from the contact, which might be facilitated by the presence of the repetitive ridges.

Stott & Wood [38] showed that oxides and wear debris sinter and develop a compacted layer of crystalline particles. This is a process usually associated with insufficient removal of wear debris, like for instance fretting wear. The M-surfaced disc developed contacts with a brownish appearance, but it takes long before these develop into a continuous longitudinal band. To form a continuous contact surface, the ridges must be worn away. Once formed, wear marks are still present next to the contact surface, which indicate the presence of locally persistent wear, which also contributes to the presence of wear debris.

It was not anticipated in the experimental design that wear would play a significant role. On the other hand, no major adjustments due to test disc radius reduction, were necessary. Where TB and HT tend to converge to a coefficient of friction of 0.3, the M surface develops a significantly lower level of friction. Nevertheless, further research is needed to substantiate the results and explain wear debris removal with respect to the initial surface condition.

4.4.2. THE DIFFERENCES IN BREAKING-IN

During breaking-in the contact surface is formed and, before the coefficient of friction rises, different processes take place:

- Surface roughness reduction and strengthening;
- Deformation and wear to align both surfaces and to increase conformity;
- The removal of contaminants and the formation of a protective oxide layer [1, 16], as was discussed in the previous section.

With the number of load cycles to the rise in coefficient of friction between the test disc surface and the contra disc as the indicative measure of the duration to complete these different processes, the rate of contact surface formation is ordered and evaluated.

The TB surface condition is immediately able to transfer traction forces and has a high coefficient of friction. This high instantaneous level is associated with the removal of initial oxides [15, 38], the consecutive reduction and rise to a new level with the formation of an protective oxide layer.

The straining of the asperities, next to asperity truncation, allows fast surface roughness reduction and increase of conformity. The TB surface mimics the ground surfaces and Schotsman et al. [11], chapter 2, and Mesaritis et al. [10] showed that such processes contribute to the formation of contact surfaces at ground rail surfaces.

The instantaneous coefficient of friction for the HT surface is with 0.07 low, until it starts to rise at 18×10^3 load cycles.

Conformity is not easily achieved for the HT surface condition. During test performance it was observed that the first contact surface wears away and some of the feed marks become visible again. At 24×10^3 load cycles the left part of the contact surface is smooth, while at the right part small spallations and wear slivers are present. Typical for the HT surface condition is the presence of WEL. Mesaritis [8] showed that the WEL delaminates and therefore the presence of WEL is not expected to slow down the break-in process.

The instantaneous coefficient of friction for the M surface condition is lowest of all tested surface conditions. Well-defined ridges are present at the surface and the initial total height of the roughness profile, R_t, is $R_t = 16.2 \pm 4.8\,\mu m$. By the time the coefficient of friction increases, the contact surface has formed a continuous band and R_t has decreased to $4.3 \pm 0.8\,\mu m$.

In summary, the TB surface condition shows the highest instantaneous coefficient of friction, which is best explained by asperity deformation facilitating the fast contact surface formation. The other surface conditions require, next to deformation and strengthening, significant wear to reach conformity between contact surfaces.

4.4.3. DIFFERENT CONTACT SURFACE FORMATION PROCESSES

The formation process of the contact surface from the five surface surface conditions results in a smooth surface with the exception of the HT surface condition. In the HT surface condition, material spallation occurs.

Figure 4.5B shows a gradual decrease in surface roughness as feed mark ridges were deformed and removed. However, after 18×10^3 load cycles, the average roughness started to increase, indicating the onset of material removal from the surface. The total height of the roughness profile R_t, that probably approximates the spalling depth best, develops as follows; $1.04 \pm 0.13\,\mu m$, $4.2 \pm 0.8\,\mu m$, and $7.2 \pm 1.4\,\mu m$, at 18×10^3 , 24×10^3 , and 27×10^3 load cycles, respectively.

The material spallation of the HT surface condition is explained by the stress concentration at the feed mark ridges and local, subsurface yielding. Once a steady state coefficient of friction was reached, the test control switched to stage two and traction forces applied to the surface were increased. With the increase in traction forces, also the shear stresses at the surface rise, and the subsurface position of the maximum stress moves closer to the surface [28]. Presumably, the propagation rate of the subsurface-initiated damages, that were already present, increases. The ongoing increase in R_t might therefore be explained by the longer crack path for deeper damages, taking more load cycles to produce a spall.

To substantiate this assumption a geometric correspondence between the location of the spallation of material and the feed mark positions must be present. Therefore the dashed vertical lines in Figure 4.6 schematically indicate the feed marks. The highest stresses are expected at the feed mark ridges. The Figure shows that in the $-Y$-part of the contact surface the spalls form in rows. The deepest points of the spalls are positioned between the dotted lines and associated with the former feed mark ridge position. In the Y-part of the contact surface the spalls also form rows. These observations support the assumption that the spalling is associated with long-lasting local stress concentration during breaking-in.

4.5. CONCLUSIONS

The breaking-in and contact surface formation of surface conditions representative for various rail maintenance procedures were evaluated. From the observations the following conclusions were drawn.

- The number of load cycles until a steady state coefficient of friction is reached and the contact surface is formed varies significantly for the different surface conditions tested. The transversely brushed surface is instantaneously able to transfer traction forces and the coefficient of friction is high, whereas for the machined surface, which is characterized by heavily sheared material at the surface and a high surface roughness, it takes 27×10^3 load cycles to rise.
- The differences in number of load cycles to reach a steady state are explained by the wear volume required for surface to form a contact surface with a sufficiently large contact area, and by the extent to which deformation replaces wear in the initial contact surface formation.
- Typical for the HT surface is the spallation of material. The development of subsurface initiated material spallations are explained by stress concentrations during the breaking-in phase as a result of the presence of longitudinal ridges at the surface.
- A gradual contact surface widening is observed during the test. This is the result of wear and deformation caused by contact stress concentrations in the contact extremes.
- All contact surfaces develop a red to brown color. This coloration is typically the result of oxide formation, which is confirmed by EDS and XRD analyses. When a high wear volume is required to reach conformity, a protective oxide layer might develop into a thicker layer consisting of oxides and partly oxidized wear debris.
- The experimental results indicate that, for rail maintenance, tool wear management to prevent a low initial coefficient of friction and a long breaking-in phase, is important.

BIBLIOGRAPHY

[1] P.J. Blau. "On the nature of running-in". In: *Tribology International* 38.11-12 (2005), pp. 1007–1012. ISSN: 0301679X. DOI: 10.1016/j.triboint.2005.07.020.

[2] M. Hiensch and N. Burgelman. "Rolling contact fatigue: Damage function development from two-disc test data". In: *Wear* 430-431 (2019), pp. 376–382. ISSN: 0043-1648. DOI: https://doi.org/10.1016/j.wear.2019.05.028. URL: https://www.sciencedirect.com/science/article/pii/S0043164818313991.

[3] T. Akagaki and K. Kato. "Plastic flow process of surface layers in flow wear under boundary lubricated conditions". In: *Wear* 117.2 (June 1987), pp. 179–196. ISSN: 00431648. DOI: 10.1016/0043-1648(87)90254-7.

[4] A. Kapoor. "Wear by plastic ratchetting". In: *Wear* 212.1 (Nov. 1997), pp. 119–130. ISSN: 00431648. DOI: 10.1016/S0043-1648(97)00083-5.

[5] P.J. Blau. "Mechanisms for transitional friction and wear behavior of sliding metals". In: *Wear* 72.1 (1981), pp. 55–66. ISSN: 0043-1648. DOI: https://doi.org/10.1016/0043-1648(81)90283-0. URL: https://www.sciencedirect.com/science/article/pii/0043164881902830.

[6] S. Kalpakjian, S.R. Schmid, and K.S. Vijay Sekar. *Manufacturing Engineering and Technology*. 7th SI Edition. Pearson, 2014, pp. 1–1224. ISBN: 9780133128741.

[7] Z.B. Hou and R. Komanduri. "On the mechanics of the grinding process, Part II - Thermal analysis of fine grinding". In: *International Journal of Machine Tools and Manufacture* 44.2-3 (Feb. 2004), pp. 247–270. ISSN: 08906955. DOI: 10.1016/j.ijmachtools.2003.09.008.

[8] M. Mesaritis et al. "Post-field grinding evaluation of different rail grades in full-scale wheel/rail laboratory tests". In: *Tribology International* 177 (Jan. 2023). ISSN: 0301679X. DOI: 10.1016/j.triboint.2022.107980.

[9] M. Steenbergen. "Rolling contact fatigue in relation to rail grinding". In: *Wear* 356-357 (June 2016), pp. 110–121. ISSN: 00431648. DOI: 10.1016/j.wear.2016.03.015.

[10] M. Mesaritis et al. "A laboratory demonstration of rail grinding and analysis of running roughness and wear". In: *Wear* 456-457 (Sept. 2020). ISSN: 00431648. DOI: 10.1016/j.wear.2020.203379.

[11] B. Schotsman et al. "Surface characterization and microstructural evolution of railway rails in a medium-wide curve after preventive grinding". In: *Wear* 580-581 (Oct. 2025). ISSN: 00431648. DOI: 10.1016/j.wear.2025.206237.

[12] S.R. Pearson et al. "The effect of temperature on wear and friction of a high strength steel in fretting". In: *Wear* 303.1-2 (June 2013), pp. 622–631. ISSN: 00431648. DOI: 10.1016/j.wear.2013.03.048.

[13] T. Kayaba and A. Iwabuchi. “The fretting wear of 0.45% C steel and austenitic stainless steel from 20 to 650 °C in air”. In: *Wear* 74.2 (1981), pp. 229–245. ISSN: 0043-1648. DOI: https://doi.org/10.1016/0043-1648(81)90165-4. URL: https://www.sciencedirect.com/science/article/pii/0043164881901654.

[14] H. Krause. “Tribochemical reactions in the friction and wearing process of iron”. In: *Wear* 18.5 (1971), pp. 403–412.

[15] P.J. Blau and C.E. Devore. “Interpretations of the sliding friction break-in curves of alumina-aluminum couples”. In: *Wear* 129.1 (1989), pp. 81–92. ISSN: 0043-1648. DOI: https://doi.org/10.1016/0043-1648(89)90281-0. URL: https://www.sciencedirect.com/science/article/pii/0043164889902810.

[16] P.J. Blau. “Interpretations of the friction and wear break-in behavior of metals in sliding contact”. In: *Wear* 71.1 (1981), pp. 29–43. ISSN: 0043-1648. DOI: https://doi.org/10.1016/0043-1648(81)90137-X. URL: https://www.sciencedirect.com/science/article/pii/004316488190137X.

[17] F.H. Stott. *High-temperature sliding wear of metals*. Tech. rep. 2002, pp. 489–495. URL: www.elsevier.com/locate/triboint.

[18] D.I. Fletcher and J.H. Beynon’. “Development of a Machine for Closely Controlled Rolling Contact Fatigue and Wear Testing”. In: *Journal of Testing and Evaluation* 28.4 (2000).

[19] M. Ishida. “Development of rail/wheel high speed contact fatigue testing machine and experimental results”. In: *RTRI report* 2.5 (1988), pp. 2–7.

[20] M. Hiensch et al. “Rail head optimisation to reach a sustainable solution preventing Railway Squeal Noise”. In: *INTER-NOISE and NOISE-CON Congress and Conference Proceedings*. Vol. 2007. 5. 2007, pp. 2355–2364.

[21] A. Jaschinski. “On the application of similarity laws to a scaled railway bogie model.” PhD thesis. Delft University of Technology, 1991.

[22] J.J. Boesten. *Study of degradation and damage in a pearlitic steel rail during cyclic grinding maintenance and subsequent wheel-rail contacts*. Tech. rep. Delft University of Technology, 2019.

[23] M.A. Razzak. *Heat treatment and effects of Cr and Ni in low alloy steel*. Tech. rep. 7. 2011, pp. 1439–1445.

[24] ASTM. *E112-24 Standard test methods for determining average grain size*. ASTM, 2004.

[25] G.F. Vander Voort and A.M. Gokhale. “Comments on “grain size measurements using the point-sampled intercept technique””. In: *Scripta metallurgica et materialia* 26.10 (1992), pp. 1655–1660.

[26] CEN. *prEN13674-1 - Railway applications - Rail - Part 1: Vignole railway rails 46 kg/m and above*. European Committee for Standardization, 2023, pp. 1–112.

[27] M. Hiensch and M. Steenbergen. “Rolling Contact Fatigue on premium rail grades: Damage function development from field data”. In: *Wear* 394-395 (2018), pp. 187–194. ISSN: 00431648. DOI: 10.1016/j.wear.2017.10.018.

[28] K.L. Johnson. *Contact Mechanics*. Cambridge University Press, May 1985. ISBN: 9780521255769. DOI: 10.1017/CBO9781139171731.

[29] B. Schotsman. *Spalling defects in MHH steel rails, a study on the defect initiation and spalling after aggressive grinding*. Tech. rep. Utrecht: ProRail, Oct. 2017.

[30] Hirofumi Itagaki, Kazumasa Ohama, and Aravindh Nammalvar Raja Rajan. "Method for estimating traction curves under practical operating conditions". In: *Tribology International* 149 (Sept. 2020). ISSN: 0301679X. DOI: 10.1016/j.triboint.2019.02.047.

[31] M.C. Burstow. "A model to predict and understand rolling contact fatigue in wheels and rails". In: *Proceedings of the 7th World Congress on Railway Research (WCRR 2006), Montreal, Canada*. 2006.

[32] M.C. Burstow. *VTAC calculator: Guidance note for determining Tgamma values*. Tech. rep. London: Network Rail, 2012.

[33] J.J. Kalker. "A Fast Algorithm for the Simplified Theory of Rolling Contact". In: *Vehicle System Dynamics* 11.1 (1982), pp. 1–13. DOI: 10.1080/00423118208968684. URL: https://doi.org/10.1080/00423118208968684.

[34] CEN. *ISO4287:1997 - Geometrical Product Specification - Surface texture: Profile method - Terms, definitions and surface texture parameters*. 1997.

[35] M. Kráčalík, G. Trummer, and W. Daves. "Application of 2D finite element analysis to compare cracking behaviour in twin-disc tests and full scale wheel/rail experiments". In: *Wear* 346 (2016), pp. 140–147.

[36] J. Torrent and V. Barrón. *Diffuse Reflectance Spectroscopy of Iron Oxides*. Ed. by Marcel Dekker. 2002. URL: https://www.researchgate.net/publication/264869284.

[37] G. Kortüm. "Regular and diffuse reflection". In: *Reflectance Spectroscopy: Principles, Methods, Applications* (1969), pp. 5–71.

[38] F.H. Stott and G.C. Wood. "The influence of oxides on the friction and wear of alloys". In: *Tribology International* 11.4 (1978), pp. 211–218. ISSN: 0301-679X. DOI: https://doi.org/10.1016/0301-679X(78)90178-0. URL: https://www.sciencedirect.com/science/article/pii/0301679X78901780.

5

EXPERIMENTAL INVESTIGATION ON THE FATIGUE AND FRACTURE TOUGHNESS PROPERTIES OF HYPEREUTECTOID RAIL STEEL

Increasing train speeds and the reduction of maintenance slots places high demands on the railway rails. To meet the challenging demands, producers regularly introduce new steel types. In this experimental investigation the mechanical behavior of an air-cooled vanadium-alloyed hypereutectoid rail steel is presented. The rail is produced by applying conventional hot rolling of a reheated bloom and is then cooled on a cooling bed. The mechanical behavior is determined by performing standardized linear elastic fracture mechanics tests. The necessary specimens are extracted from new rails that are made in series production. Monotonic tensile test results have shown that the strain-hardenability of the steel is comparable to standard-grade eutectoid rail steel and is higher than that of an accelerated-cooled eutectoid rail grade. The fracture toughness test results showed, statistically, no difference when compared with the fracture toughness values of the accelerated-cooled eutectoid rail grade. The tests were performed at room temperature. The fatigue crack growth rates in the linear Paris-regime, are higher than in the previously mentioned steels. At a load ratio of 0.1 the fatigue crack growth is comparable to the referenced steels at a load ratio of 0.5. The results are explained considering the distinct microstructural characteristics of the air-cooled vanadium-alloyed hypereutectoid steel and the fractured surfaces of the specimens. This experimental investigation contributes to selecting railway steels and predicting the actual in-service behavior.

This chapter is based on: B. Schotsman, V. Mattos Ferreira, D. Leonetti, R.H. Petrov, M.J. Santofimia, J. Sietsma, "Experimental investigation on the fatigue and fracture toughness properties of hypereutectoid rail steel", Engineering Fracture Mechanics, Volume 313, 2025, 110657, ISSN 0013-7944, https://doi.org/10.1016/j.engfracmech.2024.110657.

5.1. INTRODUCTION

The increasing train speeds and wheel loads in modern railway operations impose additional requirements on the railway track substructure, and more specifically on the rails. Moreover, the increasingly busy traffic limits the inspection and maintenance options, in both duration and frequency. Therefore infrastructure managers have introduced a damage-tolerant maintenance methodology. In addition, a reduction in rail wear is preferred since material consumption, like steel rails, is the major contributor to the carbon emissions of the railroad [1]. To enable further progress of railways, development of the rail steels is required.

As rails are hot rolled from continuously casted blooms, rail producers can choose to improve the strength and wear resistance by changing the steel composition or by introducing a post-rolling heat treatment, depending on the rolling mill facilities.

The design of the post-rolling heat treatment of rails is generally simple and consists of controlled accelerated cooling to approximately 500 °C followed by air-cooling. Accelerated cooling limits carbon diffusion between cementite and ferrite in the typically pearlitic steels, resulting in a smaller lamellar thickness and an increase in yield strength. Between lamellar thickness and yield strength a Hall-Petch relationship is obeyed [2, 3, 4].

In terms of steel composition, traditionally, the carbon content was increased to improve wear resistance and strength. However, this practice introduces the risk of undesired grain boundary embrittlement because of the formation of a cementite network on the prior austenite grain boundaries. In hyper-eutectoid steels, silicon is often added to suppress cementite formation at prior austenite grain boundaries. Furthermore, vanadium is added to increase the wear resistance [5, 6]. Wilby et al. [6], as an example, reported better wear properties for the air-cooled vanadium-alloyed steel compared to the accelerated-cooled pearlitic steel, having approximately the same hardness. Additionally, vanadium-carbide formation consumes carbon, effectively reducing the local carbon content. However this is not sufficient to prevent coarse cementite particles from precipitating in the thin pro-eutectic ferrite layer [7].

Minimum values for fracture toughness of rail steels are common requirements for quality control and material acceptance. High fracture toughness promotes easier inspectability of the rails due to the larger allowable crack size. To explain the microstructure characteristic and fracture toughness relationship in pearlitic steels studies focus on the prior-austenite grain size and lamellar thickness.

The size of prior-austenite grains (PAGs), in which the pearlite colonies have nucleated, is found to control the fracture toughness [8, 9, 10]. Crack path analysis showed that the cleavage fracture propagates through the (100)-crystallographic plane of the ferrite following low-angle grain boundaries between pearlite colonies, i.e. between colonies with a comparable crystallographic orientation. An analysis of the angles between colonies in large and small PAGs steels further showed that large PAGs are associated with the majority of colony misorientations being below 5°, whereas in small-PAGs steels misorientations are uniformly distributed over the classes below 5°, below 10°, and over 10° misorientation [10]. These PAGs related size of 'orientation units', consisting of adjacent pearlite colonies of common parentage and therefore common orientation, control the fracture toughness [10].

Other researchers point at lamellar thickness as the microstructure property explaining the fracture toughness [4, 11, 12]. The highest fracture toughness values were found for steels with the highest lamellar thickness. Kavishe and Baker [4] explained the result by the actual size of the fracture process zone, which is small compared to the yielding area at the crack tip, and always smaller than the prior-austenite grain.

Fatigue crack growth has also been studied with respect to the pearlite microstructure characteristics and the fracture mechanism, but with inconclusive results [13]. Gray et al. [14] and Daeubler et al. [15] independently performed crack growth tests on American ISO1080 eutectic railway steel. Using C(T)-specimens, it was concluded by Gray et al. that coarsening the prior austenite grain structure reduces the fatigue crack growth rate [14]. Using a tensile-tensile test setup and a stress ratio between $0 < R < 1$, Daeubler et al. concluded the opposite; fine PAG size and small lamellar thickness result in the lowest crack propagation rate [15]. A complicating factor explaining crack growth is that both the orientation of the crack as well as the mechanism of crack growth change with the increase of stress-intensity factor range, ΔK, consequently affecting the crack path at the mesoscale. At low ΔK, the crack propagates in the ferrite between the cementite lamellae [13, 14]. The cementite lamellae act as a boundary for local yielding and therefore a smaller lamellar distance retards the crack propagation [13, 14, 15]. In the stable crack-propagation stage, the Paris-regime, the crack propagation is stress-controlled, causing a staircase morphology at the fractured surface, of which the size is related to the lamellar thickness. At a further increase of ΔK, such that the maximum stress intensity approaches its critical value, and the crack growth is close to being unstable, the staircase features are replaced by cleavage planes and the surface gradually becomes similar to a cleavage fracture surface [13, 16].

In the present study, the fatigue crack growth rate and fracture toughness of an air-cooled hypereutectoid rail steel are evaluated using linear elastic fracture mechanics tests. The test procedure for the determination of fatigue crack growth rate in steels is regulated by relevant international standards, such as the ASTM E647 [17]. The test procedure in the ASTM E399 standard [18] has been developed and standardized to measure plane-strain fracture toughness of metallic materials under Mode-I loading. The objective of this procedure is to determine the size-independent material property K_{IC}, defined in terms of the stress intensity factor, K [19]. In practice, the material is tested on specimens containing a crack that nucleates from a starter notch due to fatigue. The plane-strain fracture toughness under other modes of opening has been correlated to K_{IC} [20]. One of the challenges of railway operations is the control of rolling contact fatigue in the rails. Due to the occurrence of cyclic loading, cracks initiate and propagate at an angle of 20° - 30° with respect to the rolling surface [21]. At these initial stages, the fatigue crack growth is driven by mixed-mode conditions. At a later stage of crack propagation, it was observed that rolling contact fatigue cracks, outside the volume affected by the presence of the rail-wheel contact stresses, tend to grow downwards, i.e. in the vertical plane [21, 22]. For these reasons, fracture toughness and fatigue crack growth rate under mode-I loading will, besides serving as a benchmark, also provide insight into the microstructural behavior of rail steel.

The objective of the experimental study is therefore to determine the mechanical behavior of the air-cooled hypereutectoid rail steel using linear elastic fracture mechanics

(LEFM) tests. A fractographic analysis of the fatigue crack growth, fracture toughness, and tensile specimens, is made to study the crack path and relation with the microstructure characteristics of this steel, in line with a previous study by Mattos Ferreira [7]. The results are further benchmarked with results on accelerated-cooled eutectoid rail steel, using the same test setup [23, 24], and eutectoid rail steels [9, 25] from the literature.

5.2. MATERIALS AND METHODS

5.2.1. MATERIALS

Table 5.1 shows the chemical composition of the air-cooled hypereutectoid rail steel, R335V, together with the accelerated-cooled eutectoid rail steel, R350HT, and the eutectoid rail steels, Ref1 and Ref2. Specific for R335V is the 0.10 wt.% vanadium and ~0.9 wt.% silicon addition. The composition is within the composition ranges as provided by the EN13674-1-standard [26].

The microstructure is further defined by the production route. The R335V rail is hot rolled from a reheated bloom and subjected to air-cooling. The typical temperature at the last rolling step is $T \approx 1050\,^{\circ}\text{C}$. The cooling rate during transportation to the cooling bed is ~1 °C/s and the temperature when arriving there is ~800 °C. The typical cooling rate on a cooling bed is ~0.1 °C/s [27].

The composition of R350HT accounts for a lower carbon and silicon content, and a higher manganese content when compared with R335V steel. During production, R350HT steel rail is hot rolled followed by controlled accelerated cooling to ~500 °C and is then air-cooled, resulting in a smaller lamellar thickness.

The chemical composition of both eutectoid rail steel grades, Ref1 [9] and Ref2 [25], are included in the bottom section of Table 5.1.

Table 5.1: Chemical composition (in wt.%) of air-cooled hypereutectoid steel, R335V, the referenced accelerated-cooled eutectoid rail steel, R350HT, and eutectoid rail steels, Ref1 and Ref2.

Steel	Element concentration (wt.%)				Steel grade
	C	Mn	Si	V	
R335V [7, 24]	0.91	0.88	0.87	0.10	HP335
R335V [23]	0.91	0.86	0.88	0.10	HP335
R350HT [23]	0.77	1.10	0.39	-	R350HT
Ref1 [9]	0.74	1.06	0.27	-	R260
Ref2 [25]	0.68	1.11	0.35	-	900A

5.2.2. FRACTURE MECHANICS TESTS

TENSILE TESTS

Figure 5.1 presents the position of the cylindrical tensile specimens extracted from the rail head. This position is in accordance with the EN13674-1-standard [26]. The tensile test specimens are produced, using a turning process, from a strip which was cut from both sides of the rail profile. The test specimens are positioned in the center of the strip.

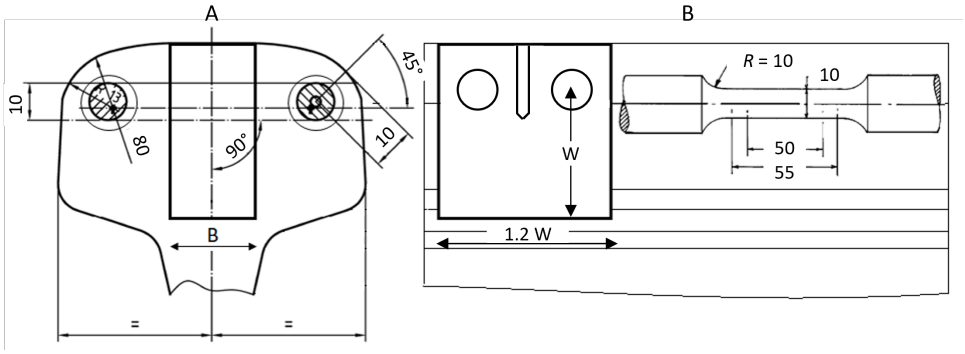

Figure 5.1: Location, orientation, and dimensions (mm) of C(T)- and tensile-specimens in the rail profile. A) The rail head cross-section. B) The longitudinal section.

The monotonic tensile tests were performed using an Instron 5985 universal testing system equipped with a self-aligning wedge grip fixture and a 250 kN load cell. The elongation was measured with an Instron AVE 2 non-contacting video extensometer. A constant crosshead separation speed of 0.75 mm/min is chosen which corresponds to a strain rate $\dot{\epsilon_L} = 0.25 \times 10^{-3}\,\mathrm{s}^{-1}$ according to the EN-ISO6892-1-standard [28]. The specimens were maintained at 200 °C for 6 h before performing the tests, to relax near-surface stresses due to specimen production as prescribed in the EN13674-1-standard [26].

FATIGUE CRACK GROWTH AND FRACTURE TOUGHNESS TESTS

Table 5.2: Linear elastic fracture mechanics tests on R335V rail steel; references, specimen type, dimensions, and number of tests.

Test	Reference	Specimen type	Dimensions (mm)	Number
Fatigue crack growth	ASTM E647 [17]	C(T)	$W = 40$, $B = 10$	4
Fracture toughness	ASTM E399 [18]	C(T)	$W = 40$, $B = 18$*	4
			$W = 40$, $B = 20$**	3

* Specimens extracted from a UIC56-rail profile [26]; the rail head dimensions limits the thickness to $B = 18$ mm; specimens 1-4.

** Specimens extracted from a UIC60-rail profile [26]; specimens 5-7.

Table 5.2 presents the relevant information on the C(T)-specimens used to quantify the fatigue crack growth rate and plane-strain fracture toughness. Figure 5.1 presents the specimen position in the rail head section, which is the center of the rail head with the straight notch pointing downwards, aligning with the crack propagation orientation in in-service rail [21, 22]. The C(T)-specimens are produced by face milling. The holes are drilled and reamed on the same machine before polishing the surfaces. The straight notch is cut by electric discharge milling.

The test performance and analyses follow the ASTM-E647 [17] and ASTM-E399- standards [18]. Specifically for fracture toughness determination the requirements for static testing are followed. Both fatigue crack growth and plane-strain fracture toughness tests have been performed in a test frame equipped with a hydraulic actuator and a load cell with a nominal capacity of 125 kN, using closed-loop control and force feedback. The data acquisition system from National Instruments has a sampling frequency of 300 Hz. The specimens were loaded through a clevis and pin, designed according to the aforementioned standards. Both clevises are connected to the load line using spherical hinges to minimize secondary bending moments. The loading frequency is 10 Hz and has a sinusoid waveform. At the selected frequency self-heating is limited [29, 30], has a negligible influence on the results and is not further included in the analysis.

Fatigue crack growth is monitored using a dual cantilever clip-on displacement transducer - model UB-5A from TML - mounted directly on the integral knife edges at the crack mouth. The fatigue crack growth, $\mathrm{d}a/\mathrm{d}n$, is presented as a function of ΔK at a double logarithmic scale. The $\mathrm{d}a/\mathrm{d}n$ is the average over a fixed ΔK-step size. Table 5.3 presents the cyclic loading conditions.

The plane-strain fracture toughness is the material property that describes the critical condition for the onset of unstable crack growth under plane-strain. It is expressed as the critical stress intensity factor, K_{IC}. The scalar K_I represents the stress field close to the tip of a crack [31], and is calculated as:

$$K_I = \alpha\sigma(\pi a)^{1/2}, \tag{5.1}$$

with α being the geometrical factor for test specimens of finite size provided in ASTM E399 [18], σ the stress in the nominal cross section (without considering the presence of the crack) and a the crack length.

To determine the fracture toughness first a fatigue pre-crack was induced in the specimens by applying constant amplitude loading characterized by a load ratio $R < 0.1$ and a maximum force $P_{max} \leq 10$ kN, as presented in Table 5.5, section 5.3. During pre-cracking, the crack size was monitored using compliance measurement based on crack mouth opening displacement, v. The compliance, u, is calculated as [17]:

$$u = \left[\left(\frac{EvB}{P}\right)^{1/2} + 1\right]^{-1}, \tag{5.2}$$

where E is the Young's Modulus and P the applied load. To minimize the effect of crack closure on compliance reading, Equation 5.2 is evaluated at 90% of the load, at the descending part of the constant amplitude loading cycle [32].

The normalized crack length is, for C(T)-specimens, calculated as [18]:

$$\frac{a}{W} = 1.0010 - 4.6695u + 18.460u^2 - 236.82u^3 + 1214.9u^4 - 2143.6u^5, \tag{5.3}$$

with a being the crack length and W the specimen width.

Secondly are the fracture toughness tests performed by applying an increasing load at a constant rate up to fracture, and such that the increase of the stress intensity factor is between 0.55 and 2.75 MPa $\mathrm{m}^{1/2}$/s for quasi-static testing in accordance with ASTM-E399 [18].

Table 5.3: Loading conditions of the specimens in the fatigue crack growth tests

Specimen	P_{max} [kN]	Load ratio, R	Specimen	P_{max} [kN]	Load ratio, R
1	4.0	0.1	3	3.5	0.1
2	4.0	0.5	4	6.0	0.5

The load-displacement plot is analyzed following the procedure for determination of fracture toughness, reported in Annex X of ASTM E399 [18]. In this procedure, the slope of the secant to the load-displacement curve, used to identify the load for fracture toughness determination, is dependent on the ligament and not fixed to 95%. This waives the condition that the maximum load should not be larger than 1.1 P_Q for a test to be valid, which is defined as the load at pop-in or the intersection with the secant line, depending on the principal type of the load-displacement record [18]. The secant offset percentage, S_Q, is a function of the ligament of the crack, defined as W - a, and is related to a constant crack extension. The 95% offset secant is based on a crack extension that is a constant fraction of the final pre-crack size [33].

The same test setup and analysis procedure was employed by Leonetti and Schotsman [23] and Leonetti et al. [24] to determine plane-strain fracture toughness and fatigue crack growth rate of the R350HT rail steel.

The length of the fatigue pre-crack in the fracture toughness specimens is the sum of the notch depth and the length of the fatigue crack emanating from that notch. The notch depth is measured on both sides of the fractured specimens using an Olympus Stereo SZX9 microscope, and averaged. The length of the fatigue crack is then measured using a Keyence VX5000 optical microscope. The measurement positions are provided by ASTM E399, i.e. at the intersection with the free surfaces, at 25%, 50%, and 75% of the thickness, resulting in a total of 5 measurements per specimen. The average of the measurements conducted at 25%, 50%, and 75% is used as the fatigue crack length [18].

5.2.3. METALLOGRAPHIC PREPARATION AND OBSERVATIONS

The observations for fractographic analysis of the tensile, crack growth, and fracture toughness specimens are made after 30 minutes of ultrasonic cleaning in isopropanol, using a Jeol IT100 Scanning Electron Microscope (SEM), with a 15 kV acceleration voltage and 10 mm working distance in secondary electron imaging mode.

Higher magnification micrographs of the microstructure were obtained with a Helios G4 PFIB UXe SEM using a 10 kV accelerating voltage, 0.1 nA current, in secondary electron imaging detection mode.

For the characterization of the tensile test specimens cross-section samples were made and embedded in conductive resin. Standard metallographic sample preparation was performed followed by chemical etching with Nital diluted to 2% for 10 s. Three lines of Vickers microhardness measurements were made at the specimen center and close to the free surface using a Durascan 70 hardness tester by applying a load of 10 N for 10 s. As a reference, 5 lines of hardness measurements were made on the rail head center of the unused rail. Successively, high-magnification images of the microstructure were made using a SEM model Jeol 6500F, with a working distance of 10 mm, and an acceleration voltage of 20 kV.

5.3. RESULTS

5.3.1. MICROSTRUCTURE

Figure 5.2A presents the micrograph of the as-received R335V steel grade evidencing the pearlitic microstructure and the presence of localized boundary ferrite. The presence of a ferrite layer was also observed in other hypereutectoid steels [34, 35] and is a result of silicon alloying and vanadium carbide formation [7, 36]. However, coarse cementite particles are present at these boundaries. In a study on microstructural characterization of R335V Mattos Ferreira [7] observed the presence of randomly distributed vanadium carbide-precipitates strengthening the cementite.

Figure 5.2B presents the microstructure of R350HT rail steel as a reference. A wider pro-eutectoid ferrite network is present.

High-magnification SEM images, Figures 5.2C and D, qualitatively show the lamellar thickness. For R335V this is larger when compared to R350HT. The observations were made on a sectioning plane perpendicular to the lamellae.

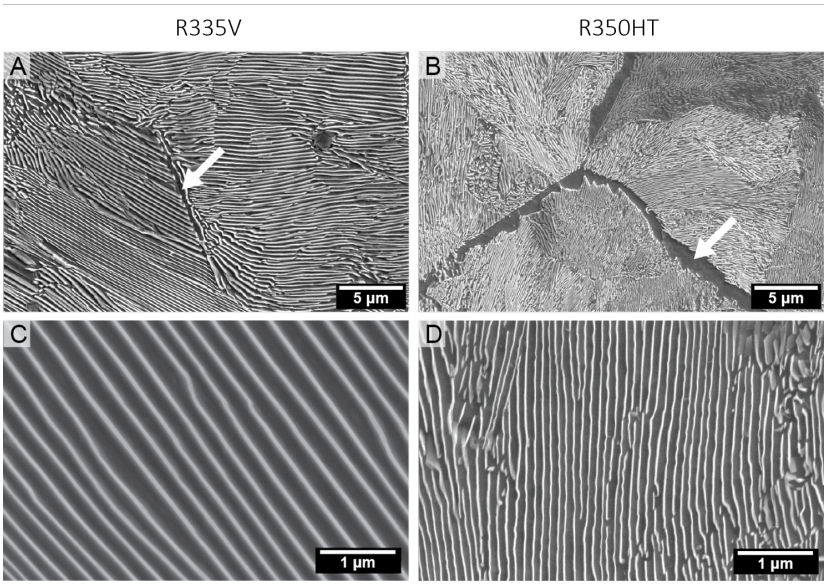

Figure 5.2: Scanning electron micrographs of the as-received R335V (A, C) and R350HT (B, D) steels (respectively). (A, B) The pearlitic microstructure with white arrows indicating the presence of smaller and wider boundary ferrite networks. (C, D) The greater respectively smaller lamellar thickness, as is visually observed on the SEM images.

Figure 5.3 shows the hardness measured at the rail head center starting 0.5 mm from the surface. R335V rail steel has an average hardness of 351 ± 12 HV, while R350HT steel has an average hardness of 379 ± 9 HV. The hardness of standard grade Ref1, which has a similar carbon content as R350HT, is 288 ± 2 HV [9].

The absence of a continuous network suggests a larger volume fraction of cementite to be present in the pearlite [37]. Both the VC-precipitation and the increased cementite fraction contribute to hardness.

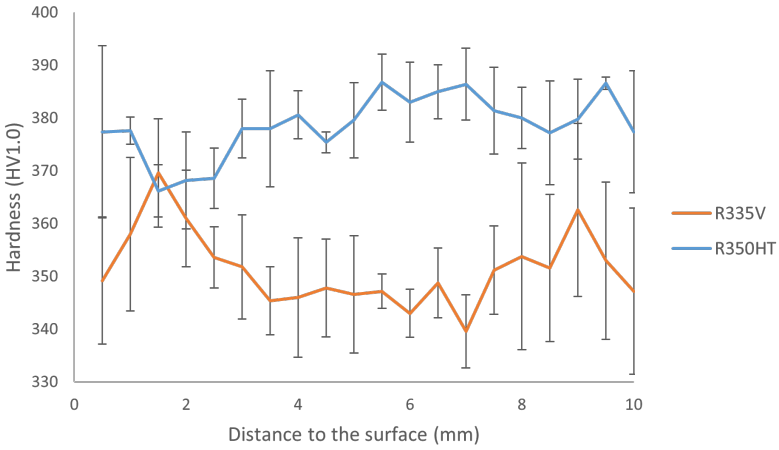

Figure 5.3: Hardness of R335V and R350HT, measured on a transverse section of the rail head, at the centerline of the rail profile.

5.3.2. RESULTS OF THE LINEAR ELASTIC FRACTURE MECHANICS TESTS

TENSILE BEHAVIOR

Performing monotonic tensile tests is a pre-requisite to determine the settings of the LEFM-tests. Additionally, the interpretation of the shape of the stress-strain curve delivers valuable information about the response of the steel, whereas the fractography provides insight into the crack path and the microstructure relationship.

Table 5.4 shows the tensile test results with the standard deviation of the average for the tests on R335V [7] and R350HT [23]. In the same table the results for standard grades Ref1 [9] and Ref2 [25] are presented. The ultimate tensile stress, σ_{UTS} [MPa], is defined as the maximum load, [N], divided by the undeformed area of the specimens, [m^2], σ_y [MPa] as the 0.2%-offset yield strength, and ε as the plastic elongation at fracture, measured over the parallel length of the specimens.

Table 5.4: Tensile test results of R335V, R350HT and Ref1 and Ref2.

Steel	E (GPa)	σ_y [MPa]	σ_{UTS} [MPa]	ε(%)	n
R335V [7]	210 ± 5	700 ± 11	1161 ± 12	8.2 ± 0.2	0.253 ± 0.003
R350HT [23]	219 ± 6	839 ± 8	1232 ± 8	10.4 ± 0.5	0.196 ± 0.002
Ref1 [9]		731	951	15.5	
Ref2 [25]		533	924	12	0.249

The strain hardening capacity of the steels is presented as the strain hardening exponent n, the exponent of the true stress as a function of true strain for the uniform plastic deformation, which is used to compare the strain hardenability of steels [38]. The results for R335V and R350HT are calculated from the tensile test results [7, 23]. For Ref2 n is presented in the literature [25].

Figure 5.4 presents the monotonic stress-strain curves that were obtained for R335V, in orange, in blue the R350HT results, and in black results for standard grade Ref2 [25]. The lines parallel to the elastic part of the curve indicate the average total plastic elongation at fracture. Two additional aspects of the material response to the increasing tensile stress are considered. First the strain during the elastic-plastic transition, an indication of how the yielding starts, and secondly the non-uniform material deformation, after necking.

For R335V the yielding evolution is sudden and limited necking takes place as such a very limited stress reduction is observed. Figure 5.4 shows a gradual transition from elastic to plastic elongation in the tensile curves of R350HT steel. After reaching σ_{UTS} non-uniform deformation sets in, until fracture, at a, compared to R335V, larger plastic strain. Also Ref2 steel shows a gradual transition to plasticity and even more plastic strain at fracture.

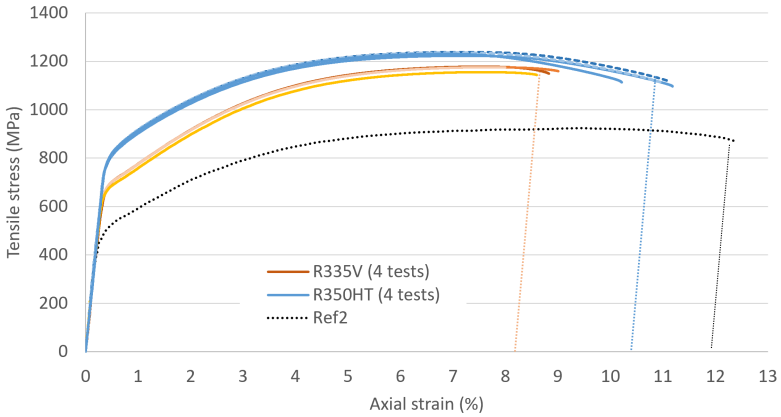

Figure 5.4: Engineering stress-strain curves of the four tests of R335V [7]. The four test curves of R350HT [23] and Ref2 [25] are presented as a reference.

DEFORMATION AND FRACTOGRAPHY OF TENSILE SPECIMENS

Figure 5.5 presents the microstructural observations on the transverse plane of the tensile specimens. Limited non-uniform deformation is observed in R335V which is also evidenced by the parallel specimen sides and small shear lips in Figure 5.5A. Secondary cracks cut through the ferrite between the cementite lamellae and the crack tip blunting within the pearlite colony is an indication of local yielding, Figure 5.5B. The coloration of the specimen is the result of maintaining the specimen at 200 °C, Figure 5.5C [39].

In R350HT steel, Figure 5.5D, the deformation results in necking and large shear lips. Secondary cracks are predominantly present in the grain boundary ferrite, Figure 5.5E.

The strain-hardening properties of the steel and non-uniform deformation during the tensile tests result in the hardness trend over the cross-section as presented in Figure 5.5F. In R335V the hardness is virtually independent of the distance to the fracture surface, whereas the measured hardness in the R350HT tensile specimen close to the fractured surface, is high and decreases gradually with increasing distance.

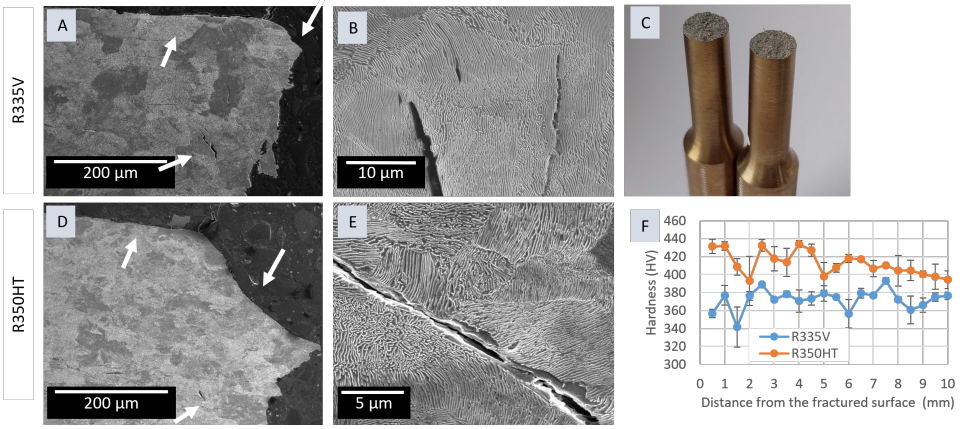

Figure 5.5: Deformation observed in the transverse plane of the tensile specimens. A) Cross-section of R335V tensile specimen. The arrows point the small shear lip and secondary cracks. B) Secondary cracking in R335V. C) The fractured R335V-specimens. D) Cross-section of R350HT. The arrows indicate the shear-lip size and secondary cracking. E) Secondary crack in R350HT. F) Hardness measurement results on the cross-section.

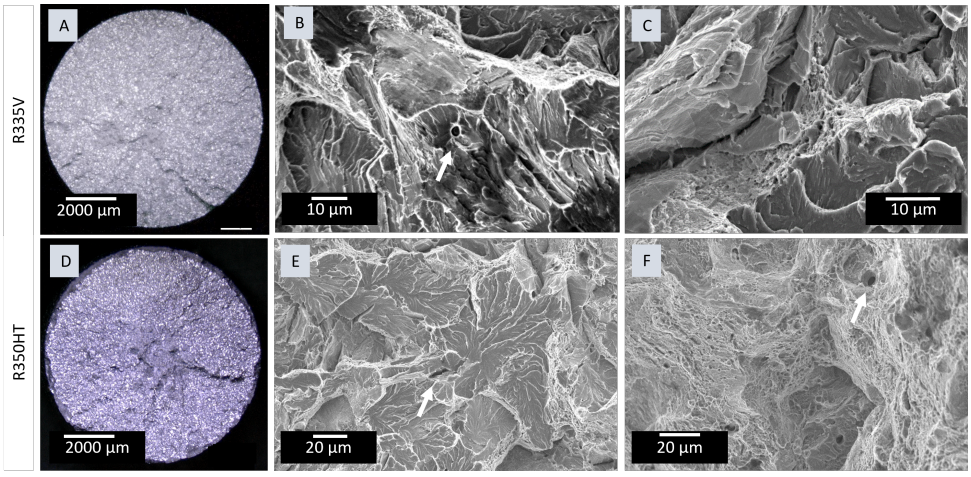

Figure 5.6: Fractography of R335V (A-C) and R350HT (D-F) tensile specimen. The arrows indicate inclusion sites in areas showing cleavage and ductile fracture.

Figure 5.6 shows the fractographic images of the tensile specimens. In Figure 5.6A the presence of a circular wavy pattern of ridges at the R335V surface is shown. Figure 5.6B and C show SEM images of representative locations on the central part of the fractured surface. The presence of clean cleavage-fracture facets is shown in Figure 5.6B. In the center of the micrograph a grain boundary is observed that encloses an area of brittle rupture. Only very limited ductile tearing patches are present and dimples are shallow, Figure 5.6C.

In R350HT a limited number of ridges is present and at the outer region a small cup-and-cone fracture is observed, Figure 5.6D. At the fracture surface, cleavage fracture areas are interspersed with areas showing ductile fracture features. The arrow in Figure 5.6E points at an inclusion site, typically present at the center of the cleavage plane. At several positions patches with equiaxed dimples are observed. The arrow in Figure 5.6F points at a larger inclusion site in the ductile fracture zone.

PLANE-STRAIN FRACTURE TOUGHNESS

The fracture toughness test results of R335V steel are presented in Table 5.5. Columns $P_{max,p}$, the maximum force during the pre-crack procedure, and a, crack length, contain the test information concerning the propagation of the fatigue pre-crack. To limit the influence of the crack-tip plastic zone on the fracture toughness results, the maximum force during final stage of the pre-cracking is limited to $P_{max,p} > 0.6P_{Qsi}$. Also, the fatigue pre-crack length is limited to $0.45 \leq a/W \leq 0.55$, with a/W the ratio of crack length and specimen width [18].

The last four columns contain the test results. P_{Qsi} is the intersect of the force-displacement-curve with the secant line. P_{max}, the maximum force in the force-displacement-curve, and K_Q the conditional result. If the K_I-test satisfies the conditions for plane-strain, K_Q can be considered K_{ISi}. In Table 5.5 the invalid results are indicated with an asterisk.

The test results of R350HT are shown as well [23, 24]. At the bottom rows the fracture toughness of Ref1, tested on samples having the same orientation [9] and Ref2 [25] are presented. To summarize the results, statistically no difference between the K_{Isi} of R335V and R350HT is observed.

FRACTOGRAPHY OF THE FRACTURE TOUGHNESS SPECIMENS

Figure 5.7 shows the fracture surface of R335V fracture toughness specimens with in Figure 5.7A the specimen with knife-edge and straight notch. Details of the surface, typical for R335V, are presented in Figures 5.7B-F. The frames in Figure 5.7A present the indicative observation locations.

The cleavage planes in Figure 5.7B are observed at a crack length $a = 32\,\text{mm}$. It is shown that from each cleavage plane a successive cleavage fracture initiates. The crack front then waves out within the plane, in the direction indicated by the river lines. Outside that area it is observed that several cleavage planes exhibit a ~90° angle. This angle is associated with the ferrite cubic BCC crystal structure [9]. The cleavage tends to advance along the (100)-plane [10].

Ductile patches are present but are only small, ranging from 20 µm to 50 µm in size. A detail of the ductile fracture characteristics is presented in Figure 5.7C. The typical hole-joining features, like dimples, are superficial, not fully developed, even at this relatively

Table 5.5: Linear elastic plane-strain fracture toughness test results.

		Precracking		Fracture Toughness Test			
	Specimen	$P_{max,p}$ [kN]	a [mm]	P_{Qsi} [kN]	P_{max} [kN]	K_Q [MPa m$^{0.5}$]	K_{Isi} [MPa m$^{0.5}$]
R335V	1	10	18.9	14.8	16.1	36.7	*
	2	10	18.7	13.4	16.5	32.7	*
	3	9.0	19.2	13.7	15.7	34.7	*
	4	9.0	18.9	12.6	15.7	31.1	*
	5	8.0	20.1	14.8	17.6	36.1	36.1
	6	8.0	20.4	14.4	17.3	35.9	35.9
	7	8.0	20.2	14.0	18.2	37.5	37.5
						34.9 ± 0.9	36.5 ± 0.5
R350HT [23, 24]	1	11.0	21.1	14.4	16.8	37.8	*
	2	10.5	20.5	15.6	20.0	39.0	*
	3	9.45	19.1	14.9	16.9	33.7	33.7
	4	10.5	18.7	15.5	18.0	34.0	*
	5	10.5	18.8	15.9	19.2	35.3	*
	6	8.6	19.3	17.1	20.6	39.1	39.1
	7	8.6	20.2	15.8	18.7	38.6	38.6
	8	8.6	20.0	15.4	19.3	37.1	37.1
						36.8 ± 0.8	37.1 ± 1.2
Ref1 (L-S) [9]							38.6
Ref2 [25]							32.5 ± 2.3

* Invalid: $P_{max,p} > 0.6 P_{Qsi}$

large crack length. This might be caused by the thin and localized grain-boundary ferrite present in the microstructure. The shallow, vein-like patterns, and 'fluted' river lines are also associated with ductile separation [31, 40].

In Figure 5.7D a detail of the framed area in Figure 5.7B is shown. The coalescence of crack planes results in the river lines at the cleavage fracture plane [31]. The resulting step sizes vary in height and orientation.

In Figure 5.7E the transition zone between the fatigue pre-crack and cleavage fracture is presented. At the right the fatigue pre-crack with a fatigue-related staircase surface pattern is observed, with a sudden transition to the brittle cleavage fracture at the left. The arrows at the surface indicate the local propagation direction. In between both areas, a local stretch zone is present. The stretch zone is a zone of plastic deformation and fibrous hole-joining fractures that occur at the tip of the fatigue crack before unstable growth by cleavage sets in [31]. This is locally observed and shown in Figure 5.7F.

To summarize the observations on R335V, cleavage planes initiate and re-initiate, and ductile patches are small. Tear ridges at a ~90° angle are present, evidencing the cleavage propagation in the (100)-planes as predicted by Park and Bernstein [10] following a path through the effective grain, a concept that describes the composed unit of pearlitic colonies with low mutual misorientation.

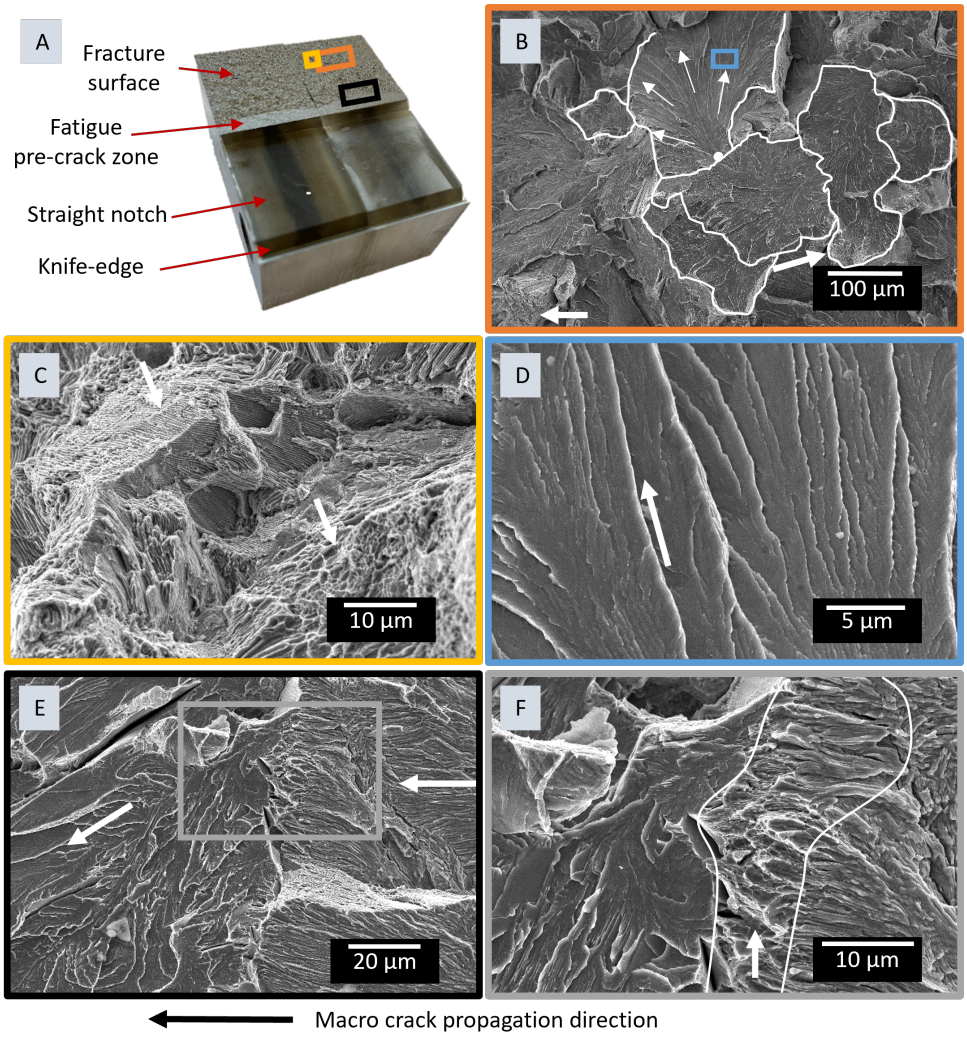

Figure 5.7: Fractographic micrographs of a R335V fracture toughness specimen. A) The fractured specimen with observation locations. B) The cleavage fracture zone with low mutual misorientation angle colonies. The re-initiation site with local propagation direction is indicated. C) An area with features of ductile fracture. Shallow dimples and a lamellar structure with fluted ductile fracture characteristics are indicated. D) River patterns in the cleavage fracture zone. E) The transition zone between fatigue pre-crack to cleavage fracture. F) Stretch zone.

FATIGUE CRACK GROWTH

In this study the crack growth of R335V steel is tested in a wide ΔK range and subsequently analyzed in the Paris-regime, as described by the Paris-Erdogan law:

$$\frac{\mathrm{d}a}{\mathrm{d}n} = C\Delta K^m, \tag{5.4}$$

with $\mathrm{d}a/\mathrm{d}n$ the crack growth rate in [m/cycle], ΔK the stress-intensity factor range [MPa$\sqrt{\mathrm{m}}$], and C [(m/cycle) /(MPa $\sqrt{\mathrm{m}})^m$] and m material parameters.

Table 5.6 presents the Paris-Erdogan material parameters for stress ratios $R = 0.1$ and $R = 0.5$, and also the test results for R350HT rail steel [23] and Ref2 [25], both using C(T)-specimens, and Ref1 steel [9] using SE(B) specimens.

Table 5.6: Paris-Erdogan crack growth parameters for R335V, R350HT, and referenced steel grades, for load ratios $R = 0.1$ and $R = 0.5$.

	$R = 0.1$		$R = 0.5$	
	C (m/cycle) /(MPa $\sqrt{\mathrm{m}})^m$	m	C (m/cycle) /(MPa $\sqrt{\mathrm{m}})^m$	m
R335V	3.47×10^{-13}	4.20	7.64×10^{-13}	4.31
R350HT [23]	4.11×10^{-13}	3.92	4.90×10^{-13}	4.09
Ref1 (L-S) [9]	2.30×10^{-13}	3.98		
Ref2 [25]	5.95×10^{-13}	3.86	1.14×10^{-12}	3.96

The fatigue crack growth rate curves for R335V rail steel are presented in Figure 5.8, in blue for the load ratio $R = 0.1$, and for $R = 0.5$ in orange. Figure 5.8 further shows the fatigue crack growth curves for R350HT [23] and the Paris curves for Ref1 [9] and Ref2 [25].

Fracture surfaces of equal crack growth rates are presented for R335V and R350HT. All micrographs shown have the same scale as is represented by the single scale bar, and the frame colors correspond with the graph colors.

The R335V graph for $R = 0.1$ is linear at the lower stress intensity factor range in this double-log graph. Scatter in the results increases from $\Delta K \sim 24$ MPa m$^{1/2}$. For stress ratio $R = 0.5$ it is observed that the crack growth accelerates, entering stage III crack growth at $\Delta K \sim 17$ MPa m$^{1/2}$.

In the fractographic images a staircase pattern, associated with fatigue crack growth, is observed at a stress ratio of $R = 0.1$ and $\sim \mathrm{d}a/\mathrm{d}n = 2.5 \times 10^{-8}$ m/cycle. The surface is almost flat. At $R = 0.5$, tear ridges are present and parallel cleavage planes are observed. Then, at the top row the crack growth is a factor 10 higher. At $R = 0.1$, still in stage II fatigue crack growth, cleavage planes with river lines are observed next to areas showing evidence of fatigue crack growth. The fracture surface of R335V tested at $R = 0.5$ is characterized by the cleavage planes at a high mutual angle. At the verge of these planes, crack arrest and re-initiation in fatigue crack growth takes place.

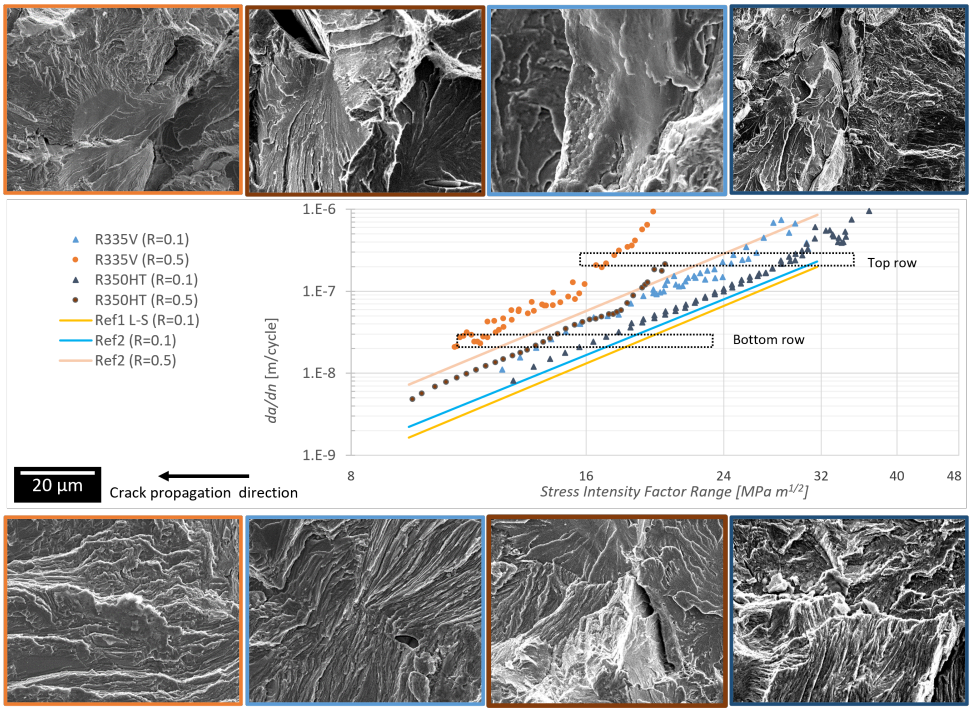

Figure 5.8: Fatigue crack growth graphs. The results for R335V and R350HT [23] are presented together with Paris-curves for Ref1 [9] and Ref2 [25]. Fractographic images at equal crack growth are shown; top row $\mathrm{d}a/\mathrm{d}n \sim 2.5 \times 10^{-7}$ m/cycle, bottom row $\mathrm{d}a/\mathrm{d}n \sim 2.5 \times 10^{-8}$ m/cycle. The image frame colors correspond with the graph colors.

The fatigue crack growth graphs for R350HT show similar characteristics as for R335V, although the crack growth rate is lower at the same stress intensity factor range. For $R = 0.1$, the graph is linear at low ΔK, and scatter increases at $\Delta K \sim 32\,\mathrm{MPa\,m^{1/2}}$. For stress ratio $R = 0.5$ the graph is linear at the lower ΔK range, and the crack growth rate accelerates, entering stage III crack growth at $\Delta K \sim 18\,\mathrm{MPa\,m^{1/2}}$.

The fractographic images of R350HT show a fine staircase pattern, which is associated with the small lamellar thickness, at $R = 0.1$ and $\mathrm{d}a/\mathrm{d}n \sim 2.5 \times 10^{-8}$ m/cycle. Increasing the stress ratio to $R = 0.5$ reveals several features such as cleavage planes, and crack arrest and re-initiation.

At the top row, at $R = 0.1$, small cleavage planes are observed showing high mutual angles and, in the micrograph, also signs of crack arrest and re-initiation are observed. The fracture surface of R350HT tested at $R = 0.5$ has different characteristics. Next to brittle cleavage facets, tear ridges are present at which ductile hole-joining features are observed.

Figure 5.9 presents fracture surface characteristics for fatigue crack growth in R335V tested at $R = 0.1$. The crack length presented in the figures is derived from the calibrated gauge opening displacement. Figure 5.9A shows a 5µm wide stretch zone between the straight crack starter notch in the specimen and a brittle cleavage crack start. In Figure 5.9B local growth directions are indicated with the arrows. The crack growth path follows microstructural features, like grain boundaries and ferrite laths, despite being in the Paris-regime [13, 15]. The observed changes in orientation might be related to a grain boundary, seen as the ridge in the figure. The small cleavage zone in the further fatigue growth-dominated surface in Figure 5.9C is interpreted as a step or bifurcation in the crack path. When the crack length increases, in Figure 5.9D, quasi-cleavage zones with crack arrest and re-initiation zones are observed. Upon further growth, fatigue crack growth and parallel cleavage planes are present at close distance, see Figure 5.9E. Figure 5.9F shows the surface close to the onset of unstable crack propagation. Cleavage planes increase in both density and size. Tear ridges between the planes are present, and some fatigue crack growth zones are still observed.

To summarize the observations regarding crack growth in R335V steel. At low fatigue crack growth rates the crack path clearly follows microstructural features. Fractography shows that fatigue crack growth characteristics are locally present even close to unstable fracture.

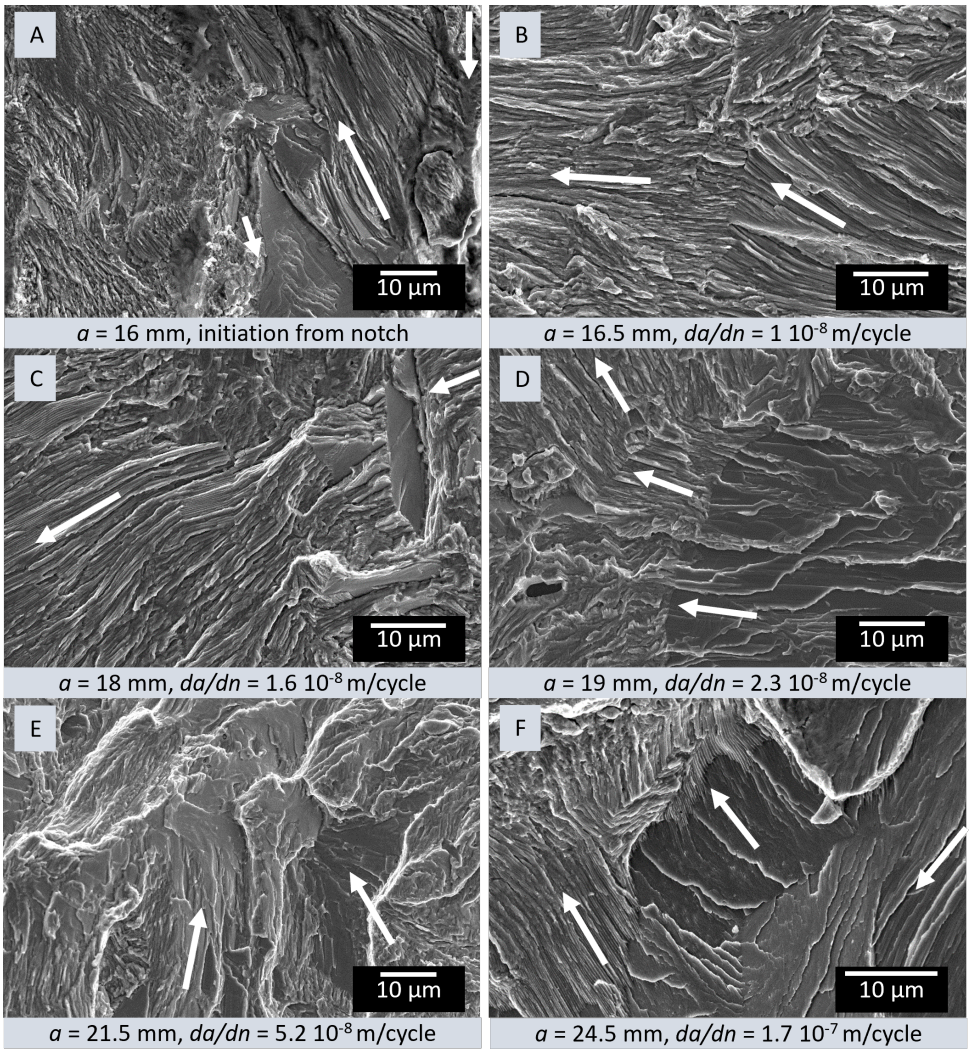

Figure 5.9: Fractography of fatigue crack growth in R335V, tested at $R = 0.1$. The images are ordered by crack length. The crack length and crack growth rate are indicated under each image. The white arrows indicate local crack propagation direction, whereas the macro crack growth is from right to left. A) Crack initiation at the straight notch. B) Fatigue crack propagation with microstructure-related crack path direction transition. C) Fatigue crack propagation with local cleavage zones. D) Crack arrest and re-initiation. E) Increase in area fraction of cleavage zones when the crack length increases. F) Quasi-cleavage crack propagation and fatigue crack propagation.

5.4. DISCUSSION

The tensile behavior, plane-strain fracture toughness, and fatigue crack growth rate results are discussed with respect to microstructure characteristics of R335V and compared with the results of R350HT [23].

5.4.1. TENSILE BEHAVIOR

The steel composition and production route of R335V result in a specific tensile behavior when compared to other rail steel grades mentioned in the EN13674-1 [26],

The strain hardening coefficient of R335V is high. In Table 5.4 is the coefficient, n = 0.253 ± 0.003, presented, together with values for the referenced steels [23, 25]. This value is higher compared to R350HT [23] and also higher than for standard grade Ref2 steel [25]. As a result, σ_{UTS} of R335V is only 6% lower than of R350HT whereas the 0.2%-offset yield strength is 17% lower.

Strain hardening is largely controlled by dislocation motion in the pearlitic ferrite, and it therefore increases with the lamellar thickness [3, 41, 42]. Measurement of the lamellar thickness is often performed in studies on the structure-property relation [43]. The difference in lamellar distance between the R335V and the R350HT rail steel can be observed by comparing Figures 5.2C and D, together with the presence of a small and wide (respectively) boundary ferrite network as shown in Figures 5.2A and B. The air-cooling after hot rolling of the R335V has resulted in a relatively larger lamellar thickness whereas accelerated cooling of R350HT resulted in the smaller lamellar thickness.

Hardness on the other hand, holds a Hall-Petch relation with the lamellar thickness [10, 16, 44]. The average hardness of R350HT, as measured at the centerline of the rail profile, is 379 ± 9 HV, which is higher than for the air-cooled standard grade Ref1. Ref1 has a similar carbon content and a hardness of 288 ± 2 HV [9]. The R335V rail steel has an overall hardness of 351 ± 12 HV. The vanadium carbide-precipitation is known to prevent the formation of a continuous pro-eutectoid cementite network [7, 21, 45], resulting, with silicon addition, in a higher cementite-ferrite ratio within the pearlite and higher hardness than can be expected from the lamellar thickness itself [37].

5.4.2. PLANE-STRAIN FRACTURE TOUGHNESS

Table 5.5 presents the results of the plane-strain fracture toughness tests. Despite the hypereutectoid composition of R335V, statistically no difference in fracture toughness between R335V and R350HT [23] is observed. These results are in line with results in other studies on rail steels [9, 11, 46].

Differences in the fracture toughness values of pearlitic rail steels are explained in the literature by two different microstructural features, the lamellar thickness [4, 11, 12] and the effective grain size, the size of clusters of pearlite colonies with small mutual misorientation [10, 9]. In deviation from the R335V steel, all rail steel grades in the referenced literature have a close to eutectoid composition [9, 11, 46], while the hyper-eutectoid composition is usually associated with lower fracture toughness [47].

Kavishe and Baker [4] conclude that a higher lamellar thickness results in a higher fracture toughness. This lamellar thickness-fracture toughness relation is not observed and therefore lamellar thickness is not the explaining factor in this experimental investigation. Figure 5.7 presents the fractured surface of an R335V specimen, and in the de-

tailed Figure 5.7B the area of parallel cleavage planes is encircled. In agreement with Park and Bernstein [10], the crack re-initiates at adjacent colonies when cleavage propagates. In steels with low mutual misorientation between colonies, little energy is consumed for this re-initiation, and as a result fracture toughness is low. Therefore, the fracture toughness of the steel is explained by the effective grain size.

To explain the similar fracture toughness values for R335V and R350HT, despite the differences in composition and lamellar thickness, the production route of both rails was observed. Reheating of the blooms, the consecutive hot rolling of rails, and recrystallization after each rolling step is the standard procedure for the production of rails. The present study indicates that this production route results in similar-sized effective grains, regardless of the cooling rate after hot rolling.

5.4.3. FATIGUE CRACK GROWTH

In Table 5.6 and Figure 5.8 the fatigue crack growth rate test results are presented. The fatigue crack growth in both R335V and R350HT [23] rail steels are determined using the same test setup, and similar sized C(T)-specimens.

Increasing the stress ratio increases the mean stress intensity factor, limits crack closure phenomena, and results in higher crack growth rate in R335V, R350HT [23] and Ref2 [25], as is observed in Figure 5.8. This is a well-known effect [9, 46, 48].

The fatigue crack growth curves in Figure 5.6 are parallel, although for R335V higher fatigue crack growth rates are observed. A small lamellar thickness is associated with a more ductile fracture behavior, with more secondary cracking [15], and with the best resistance to crack growth at low crack growth rates [13]. For small-scale yielding conditions this is explained by the radius of the plastic zone, r_y, which can be estimated as the squared ratio of the actual value of K_1 and the yield strength of the material [49], according to

$$r_y \approx \frac{1}{2\pi}\left(\frac{K_1}{\sigma_y}\right)^2. \tag{5.5}$$

A smaller lamellar thickness results in a higher resistance to yielding and retards crack growth [13].

Moreover, the composition of R335V steel is hypereutectoid with 0.91 wt% carbon content, as is presented in Table 5.1, whereas Daeubler et al. [15] used AISI1080 in their experimental investigation, with a carbon content of 0.8 wt%. Mishra et al. [13] used steel with a carbon content of 0.72 wt%. Therefore, besides lamellar thickness, a second aspect is discussed; the cementite network at the prior austenite grain boundary.

The composition of R335V is optimized with manganese, silicon and vanadium additions [5, 36, 50]. Manganese addition limits prior-austenite grain size, contributing to the toughness [8], whereas silicon prevents the formation of pro-eutectoid cementite [36]. Mattos Ferreira [7] observed the presence of a limited layer of grain boundary ferrite in the microstructure of R335V, in which also coarse cementite particles are present. This microstructure has been illustrated in Figure 5.2A.

A limited number of studies is available to reference fatigue crack growth in pearlitic hypereutectoid steels. However, despite the attention to the cementite network at the prior austenite grain boundary, Thao [37] concluded that the fatigue crack growth rate

in hypereutectoid steels is higher than in eutectoid steels. This is explained by the brittle fracture through the grain boundaries or the lower deformation capacity of the microstructure having a higher cementite content [37].

5.5. CONCLUSIONS

In this experimental investigation, the mechanical behavior of an air-cooled vanadium-alloyed hypereutectoid rail steel is characterized using standardized linear elastic fracture mechanics tests. The main conclusions are summarized below:

- Monotonic tensile test results show that the strain hardening capacity of R335V steel is higher than that of R350HT rail steel, a material property typically related to coarser pearlite. In the hypereutectoid steel non-uniform plastic elongation before fracture is virtually absent. Secondary cracks in R335V are at the ferrite-cementite interphase within the colony and crack tip blunting is observed at the extremes of the secondary interphase cracks.

- The fractography of the tensile specimens show the clear grain boundaries in the fracture region. Ductile fracture patches are present but small as a result of the thin grain boundary ferrite. Additionally, at the fracture surface of the R335V fracture toughness specimens, it is observed that ductile fracture features like dimples are shallow.

- Statistically no difference between the fracture toughness of R335V and R350HT rail steel was found. This result indicates that a damage-tolerant maintenance strategy for the railway rails can be applied when R335V steel rails are installed.

- The fatigue crack growth curve in the Paris-regime of the mode-I fatigue crack growth test is parallel to the Paris curves for R350HT and standard grade eutectoid rail steels. Although being parallel the fatigue crack growth resistance in the Paris regime is lower for R335V, such that at a load ratio of $R = 0.1$, the crack growth rate is comparable to the crack growth in referenced steel types at a $R = 0.5$. Despite the limited references available the lower crack growth resistance is explained by the hypereutectoid composition, and is, in the Paris regime, independent of the microstructure as optimized by the silicon, manganese, and vanadium additions.

- The fractography of the fatigue crack growth surfaces shows a coarse staircase pattern. At high ΔK it is observed that the cleavage facets cover a larger area fraction, but still fatigue crack growth is observed. This heterogeneity is believed to contribute to the substantial scatter in the fatigue crack growth results.

BIBLIOGRAPHY

[1] C.E. Sanches de Andrade and M. De Almeida D'Agosto. "Energy use and carbon dioxide emissions assessment in the lifecycle of passenger rail systems: The case of the Rio de Janeiro Metro". In: *Journal of Cleaner Production* 126 (July 2016), pp. 526–536. ISSN: 09596526. DOI: 10.1016/j.jclepro.2016.03.094.

[2] D.J. Alexander and I.M. Bernstein. "Cleavage Fracture in Pearlitic Eutectoid Steel". In: *Metallurgical Transactions A* 20A (1989), pp. 2321–2335. DOI: 10.1007/BF02666667.

[3] M. Dollar, I.M. Bernstein, and A.W. Thompson. "Influence of deformation substructure on flow and fracture of fully pearlitic steel". In: *Acta Metallurgica* 36.2 (1988), pp. 311–320. DOI: 10.1016/0001-6160(88)90008-9.

[4] F.P.L. Kavishe and T.J. Baker. "Effect of prior austenite grain size and pearlite interlamellar spacing on strength and fracture toughness of a eutectoid rail steel". In: *Materials Science and Technology* 2.8 (1986), pp. 816–822. DOI: 10.1179/mst.1986.2.8.816. URL: https://doi.org/10.1179/mst.1986.2.8.816.

[5] W. Solano-Alvarez, L. Fernandez Gonzalez, and H. K.D.H. Bhadeshia. "The effect of vanadium alloying on the wear resistance of pearlitic rails". In: *Wear* 436-437.August (2019), p. 203004. ISSN: 00431648. DOI: 10.1016/j.wear.2019.203004. URL: https://doi.org/10.1016/j.wear.2019.203004.

[6] A. Wilby et al. "Efficient laboratory test programme for characterising rail steel strain accumulation". In: 2022, pp. 4–7.

[7] V. Mattos Ferreira. "Microstructural phenomena in pearlitic railway steels". PhD thesis. Delft University of Technology, 2024. DOI: 10.4233/uuid:facb282f-74a1-446d-bbc6-5ed294602ed2.

[8] J. M. Hyzak and I. M. Bernstein. "The role of microstructure on the strength and toughness of fully pearlitic steels". In: *Metallurgical Transactions A* 7.8 (1976), pp. 1217–1224. ISSN: 03602133. DOI: 10.1007/BF02656606.

[9] S. Maya-Johnson, A. J. Ramirez, and A. Toro. "Fatigue crack growth rate of two pearlitic rail steels". In: *Engineering Fracture Mechanics* 138 (2015), pp. 63–72. ISSN: 00137944. DOI: 10.1016/j.engfracmech.2015.03.023. URL: http://dx.doi.org/10.1016/j.engfracmech.2015.03.023.

[10] Y.J. Park and I.M. Bernstein. "The Process of Crack Initiation and Grain Size for Cleavage Fracture in Eutectoid Steel Effective Pearlitic". In: *Metallurgical Transactions A* 10A (1979), pp. 1653–1664. DOI: 10.1007/BF02811698.

[11] L. Pessoa Moreira et al. “Effect of some microstructural characteristics on the fracture toughness and fatigue crack growth resistance of five different pearlitic steels for railroad application”. In: *Proceedings of the 23rd ABCM International Congress of Mechanical Engineering*. ABCM Brazilian Society of Mechanical Sciences and Engineering, 2015. DOI: 10.20906/cps/cob-2015-0895.

[12] L.B. Godefroid, A.T. Souza, and M.A. Pinto. “Fracture toughness, fatigue crack resistance and wear resistance of two railroad steels”. In: *Journal of Materials Research and Technology* 9.5 (2020), pp. 9588–9597. ISSN: 22387854. DOI: 10.1016/j.jmrt.2020.06.092. URL: https://doi.org/10.1016/j.jmrt.2020.06.092.

[13] K. Mishra, V. N. Khiratkar, and A. Singh. “Improvement of sub-critical fatigue crack growth life by nano-structuring of pearlite”. In: *International Journal of Fatigue* 122.January (2019), pp. 84–92. ISSN: 01421123. DOI: 10.1016/j.ijfatigue.2019.01.005. URL: https://doi.org/10.1016/j.ijfatigue.2019.01.005.

[14] G.T. Gray, J.C. Williams, and A.W. Thompson. “Roughness-Induced Crack Closure: An Explanation for Microstructurally Sensitive Fatigue Crack Growth”. In: *Metallurgical Transactions A* 14 (1983), pp. 421–433. DOI: 10.1007/BF02644220.

[15] M.A. Daeubler, A.W. Thompson, and I.M. Bernstein. “Influence of Microstructure on Fatigue Behavior and Surface Fatigue Crack Growth of Fully Pearlitic Steels”. In: *Metallurgical Transactions A* 21A (1990), pp. 925–933. DOI: 10.1007/BF02656577.

[16] J.J. Lewandowski and A.W. Thompson. “Microstructural Effects on the Cleavage Fracture Stress of Fully Pearlitic Eutectoid Steel”. In: *Metallurgical Transactions A* 17A (1986), pp. 1769–1786. DOI: 10.1007/BF02817275.

[17] ASTM. *E647-15 - Standard test method for measurement of fatigue crack growth rates*. American Society of Testing Materials, 2008.

[18] ASTM. *E399-20a - Standard Test Method for Linear-Elastic Plane-Strain Fracture Toughness of Metallic Materials*. American Society of Testing Materials, 2020.

[19] F. Ellyin. *Fatigue damage, crack growth and life prediction*. Springer Science & Business Media, 2012.

[20] H.A. Richard and M. Sander. *Fatigue crack growth*. Vol. 18. Springer, 2016.

[21] K. Han et al. “Effects of vanadium addition on nucleation and growth of pearlite in high carbon steel”. In: *Materials science and technology* 10.11 (1994), pp. 955–963.

[22] U. Zerbst et al. “Introduction to the damage tolerance behaviour of railway rails–a review”. In: *Engineering fracture mechanics* 76.17 (2009), pp. 2563–2601. DOI: 10.1016/j.engfracmech.2009.09.003.

[23] D. Leonetti and B. Schotsman. “Experimental investigation on the fatigue and fracture properties of a fine pearlitic rail steel”. In: *Frattura ed Integrità Strutturale* 18.69 (Apr. 2024), pp. 142–153. ISSN: 1971-8993. DOI: 10.3221/IGF-ESIS.69.11. URL: https://www.fracturae.com/index.php/fis/article/view/4836.

[24] D. Leonetti, V. Mattos Ferreira, and B. Schotsman. “Fracture behavior and mechanical characterization of R350HT rail steel”. In: *Procedia Structural Integrity* 47 (2023), pp. 219–226. ISSN: 24523216. DOI: 10.1016/j.prostr.2023.07.015.

5

[25] P.I. Christodoulou, A.T. Kermanidis, and G.N. Haidemenopoulos. “Fatigue and fracture behavior of pearlitic Grade 900A steel used in railway applications”. In: *Theoretical and Applied Fracture Mechanics* 83 (June 2016), pp. 51–59. ISSN: 01678442. DOI: 10.1016/j.tafmec.2015.12.017.

[26] CEN. *prEN13674-1 - Railway applications - Rail - Part 1: Vignole railway rails 46 kg/m and above*. European Committee for Standardization, 2023, pp. 1–112.

[27] F.D. Fischer, E. Hinteregger, and F.G. Rammerstorfer. “The influence of different geometrical and thermal boundary conditions and the phase transformation on the residual stress state in railroad rails after heat-treatment”. In: *International Conference on Residual Stresses: ICRS2*. 1989, pp. 467–472.

[28] ISO. *EN-ISO6892-1 - Metallic materials - Tensile testing - Part 1: Method of test at room temperature (Iso 6892-1:2019)*. International Organization for Standardization, 2019.

[29] Y. Balit et al. “Self-heating behavior during cyclic loadings of 316L stainless steel specimens manufactured or repaired by Directed Energy Deposition”. In: *Materials Science and Engineering: A* 786 (June 2020). ISSN: 09215093. DOI: 10.1016/j.msea.2020.139476.

[30] R. Munier et al. “Determination of high cycle fatigue properties of a wide range of steel sheet grades from self-heating measurements”. In: *International Journal of Fatigue* 63 (2014), pp. 46–61. ISSN: 01421123. DOI: 10.1016/j.ijfatigue.2014.01.004.

[31] D. Hull. *Fractography: observing, measuring and interpreting fracture surface topography*. Cambridge University Press, 1999.

[32] N. Fleck. “Compliance methods for measurement of crack length”. In: *Engineering Materials Advisory Services Ltd., Fatigue Crack Measurement: Techniques and Applications(UK), 1991,* (1991), pp. 69–93.

[33] D.N. Wells et al. “A review of the proposed KIsi offset-secant method for size-insensitive linear-elastic fracture toughness evaluation”. In: *Materials Performance and Characterization* 7.2 (2018).

[34] D.E. Parsons, T.F. Malis, and J.D. Boyd. “Microalloying and precipitation in Cr-V rail steels”. In: *Journal of Heat Treating* 3.3 (1984), pp. 213–219. DOI: 10.1007/BF02833263.

[35] W. Solano-Alvarez et al. “Synchrotron and neural network analysis of the influence of composition and heat treatment on the rolling contact fatigue of hypereutectoid pearlitic steels”. In: *Materials Science and Engineering: A* 707 (2017), pp. 259–269.

[36] K. Han, D. V. Edmonds, and G. D.W. Smith. “Optimization of mechanical properties of high-carbon pearlitic steels with Si and V additions”. In: *Metallurgical and Materials Transactions A: Physical Metallurgy and Materials Science* 32.6 (2001), pp. 1313–1324. ISSN: 10735623. DOI: 10.1007/s11661-001-0222-7.

[37] B. Phuong Thao. “Microstructural Factors Influencing Fatigue Crack Growth Mechanism in Low-Carbon and High-Carbon Steels”. PhD thesis. 2021.

[38] O. Hajizad et al. “Influence of microstructure on mechanical properties of bainitic steels in railway applications”. In: *Metals* 9.7 (July 2019). ISSN: 20754701. DOI: 10.3390/met9070778.

[39] F.T. Barwell et al. “The use of temper colors in ferrography”. In: *Wear* 44.1 (1977), pp. 163–171. ISSN: 0043-1648. DOI: https://doi.org/10.1016/0043-1648(77)90093-X. URL: https://www.sciencedirect.com/science/article/pii/004316487790093X.

[40] V. Bertolo et al. “Cleavage fracture micromechanisms in thick-section quenched and tempered S690 high-strength steels”. In: *Journal of Materials Science* 57.42 (Nov. 2022), pp. 20033–20055. ISSN: 15734803. DOI: 10.1007/s10853-022-07841-1.

[41] X. Hu et al. “Modeling work hardening of pearlitic steels by phenomenological and Taylor-type micromechanical models”. In: *Acta Materialia* 54.4 (2006), pp. 1029–1040. ISSN: 1359-6454. DOI: https://doi.org/10.1016/j.actamat.2005.10.030. URL: https://www.sciencedirect.com/science/article/pii/S1359645405006427.

[42] G. Langford. “Deformation of Pearlite”. In: *Metallurgical transactions A* 8A (1977), pp. 861–875. DOI: 10.1007/BF02661567.

[43] G.F. Vander Voort and A. Roósz. “Measurement of the interlamellar spacing of pearlite”. In: *Metallography* 17.1 (1984), pp. 1–17. ISSN: 0026-0800. DOI: https://doi.org/10.1016/0026-0800(84)90002-8. URL: https://www.sciencedirect.com/science/article/pii/0026080084900028.

[44] K. Mishra and A. Singh. “Effect of interlamellar spacing on fracture toughness of nano-structured pearlite”. In: *Materials Science and Engineering A* 706 (Oct. 2017), pp. 22–26. ISSN: 09215093. DOI: 10.1016/j.msea.2017.08.115.

[45] K. Han et al. “Effects of vanadium additions on microstructure and hardness of hypereutectoid pearlitic steels”. In: *Materials Science and Engineering: A* 190.1-2 (1995), pp. 207–214.

[46] L. B. Godefroid et al. “Effect of chemical composition and microstructure on the fatigue crack growth resistance of pearlitic steels for railroad application”. In: *International Journal of Fatigue* 120.July 2018 (2019), pp. 241–253. ISSN: 01421123. DOI: 10.1016/j.ijfatigue.2018.10.016. URL: https://doi.org/10.1016/j.ijfatigue.2018.10.016.

[47] G. Krauss. *Steels: processing, structure, and performance*. Asm International, 2015.

[48] R. Masoudi Nejad, K. Farhangdoost, and M. Shariati. “Microstructural analysis and fatigue fracture behavior of rail steel”. In: *Mechanics of Advanced Materials and Structures* 27.2 (2020), pp. 152–164. ISSN: 15376532. DOI: 10.1080/15376494.2018.1472339. URL: https://doi.org/10.1080/15376494.2018.1472339.

[49] S. Suresh and R.O. Ritchie. “Propagation of short fatigue cracks”. In: *International Metals Reviews* 29.6 (1984), pp. 445–475. DOI: 10.1179/imtr.1984.29.1.445.

[50] S.A. Parsons and D.V. Edmonds. “Microstructure and mechanical properties of medium-carbon ferrite–pearlite steel microalloyed with vanadium”. In: *Materials Science and Technology* 3.11 (Nov. 1987), pp. 894–904. ISSN: 0267-0836. DOI: 10.1179/mst.1987.3.11.894.

6

General discussion and Recommendations

This thesis presents research results of the investigations on rail surface conditions resulting from grinding and the durability of the contact surface that is formed. The main objective is to develop metallurgical understanding of the conditions under which damage may occur. For that purpose different research projects were designed and performed: track tests, laboratory tests, and case studies. The processes that take place at the rail surface were analyzed and the criticality of ground surface features was evaluated. Also the investigation of the fatigue and fracture toughness of a novel hypereutectoid railway steel is performed. The results of this study contribute to the development of knowledge on the relation between microstructure and mechanical behavior of pearlitic steel. In section 6.1, *discussion*, the main research findings are presented.

During the progress of these research projects future research objectives are formulated to fill knowledge gaps that were identified. These are presented in section 6.2, *Recommendations*.

6.1. Discussion

This discussion section presents the main findings of the research conducted within the framework of this project. The implications and possible adjustments to the surface condition of the freshly ground surface to improve surface durability are also discussed.

In Chapter 2 the surface roughness is presented as one of the characteristic features of the freshly ground rail surface. Vertical-axis grinding introduces a, typically, transverse lay on the applied facets. This roughness has a height profile resulting from abrasive particle size distribution and variations in degree of penetration.

The surface roughness is reduced by wear and deformation processes that are induced by rolling and sliding wheel-rail contact. It is observed that slivers are formed subsequently covering adjacent grinding grooves. Roughness asperities, which are subjected to high contact pressures, are deformed and slivers of material are progressively

extruded out of the wheel contact. This localized wear mechanism is generally indicated as *plastic ratchetting*.

In a grinding field test, Chapter 2, and a conditioned twin-disc experiment, Chapter 4, it is observed that deformation contributes to the rapid reduction in roughness and the formation of the contact surface, especially at the facet transitions. A disadvantageous aspect is that detrimental particles may not be removed during contact surface formation and get trapped. The study of micrographs in Chapter 2 confirmed that white etching layer (WEL) formed during grinding and residues of rail steel that is subjected to metallographic burn, are enclosed in the rail surface.

In the results of the research projects, performed to identify critical surface features, three grinding-related damage initiation mechanisms are identified.

Microscopic images of cross-sections of the rail samples taken during the field test (Chapter 2) revealed that damage initiates at deep grinding grooves, which typically show metallographic burn. These grinding grooves contain corroded WEL and are deformed, submerged, and still present after ~7 Mt of train load. The presence of deep grinding grooves prevents, either by the presence of geometric surface deviation or as a result of grinding burn, the uniform deformation of the surface due to wheel-rail contact. Strain concentrations, which act as preferential sites for damage initiations, appear.

The second mechanism for damage formation is identified in the case study on the railway line Zutphen-Hengelo in The Netherlands, using rails taken from this single-track line, Chapter 3. The case study shows that damage may occur when the grinding roughness does not wear off quickly enough during the formation of the contact surface. In that case, WEL starts to form on the contact surface surrounding the grinding grooves, further reducing wear. Finally, damage occurs at the bottom of the remaining grinding grooves surrounded by the WEL-coated contact surface.

The necessary surface conditions at which both observed mechanisms can lead to damage initiation can be avoided by controlling the variation in abrasive penetration depth and the height profile of the surface roughness. Allowable limits depend on site-specific conditions, especially concerning the wear rate and the wear resistance of the rail steel of the installed rail.

Incomplete removal of the short-pitch corrugation is the third mechanism identified. The results in Chapter 3 demonstrate that failure to remove the corrugation across the entire width of the wheel-rail contact surface may lead to the formation of new damage. Removal of corrugation is almost always demonstrated by performing longitudinal profile measurements at the highest point of the installed rail. However, it is important to perform measurements across the entire width of the contact surface. Special attention should be paid to this after the grinding work is completed.

Facet transition zones, the connection between facets created by vertical axis grinding, are identified in the literature as preferential zones for damage initiation, particularly under conditions of high stress and low wear, and in the presence of deep grinding grooves. The results of the field test in Chapter 2 show that contact surface formation in facet transition zones is faster than at the facet center, due to locally higher stresses. The aforementioned plastic ratcheting wear occurs, and sliver formation is accompanied by a temperature increase above A_{c3}, causing a WEL to be formed locally. The extent to which larger deformation below the facet transition surface, compared to the facet cen-

ter, occurs, decreases with increasing load cycles and the wear at the transition zones.

The introduction of frequent preventive grinding causes the formation of a new contact surface every time the rail is resurfaced. Therefore, the breaking-in behavior of different surface conditions is evaluated using a twin-disc setup, Chapter 4.

During breaking-in, surface contamination is removed, deformation and wear take place to align surfaces and to increase conformity, the contact surface gains strength and is able to transfer higher external forces. The experimental results show that the coefficient of friction between the test disc and contra disc rises shortly after the start of the cyclic loading when a contact surface is formed by the deformation of roughness asperities. But when wear is required to align surfaces, it takes longer, and higher slip speeds remain present.

Rail steels with increased wear resistance are introduced in the railways to increase grinding intervals. As part of this study a novel rail steel is characterized and the mechanical behavior is evaluated, Chapter 5. This novel air-cooled steel grade has a hypereutectoid carbon content with vanadium additions.

The experimental results show that the fatigue crack growth rate in the hypereutectoid steel is higher than in the benchmarked eutectoid steels, despite the micro-alloying with vanadium and silicon to limit the precipitation of grain boundary cementite. Due to the micro-alloying, no grain boundary embrittlement occurs. The increased crack growth is likely caused by the high cementite content in the pearlite.

The results of the experimental study contribute to the understanding of the relation between microstructure and mechanical behavior of pearlitic steels. It is concluded that, when applying this type of steel, a damage-tolerant maintenance method can be applied, but defect initiation must be closely monitored in practice to evaluate the crack growth rates in practice and to benefit from its wear-resistant properties.

6.2. RECOMMENDATIONS FOR FUTURE RESEARCH

The research presented in this thesis has extended metallurgical understanding of critical features of the freshly ground rail surfaces. Nevertheless, research on damage initiation conditions is still a *green field* and many aspects need further investigation. The area of research includes not only metallurgy but also wheel-rail interaction mechanics and process technology. During the progress of this research project, the following recommendations were formulated to fill the perceived knowledge gaps.

- It is observed that white etching layer formation and grinding burn in deeper grinding grooves may have a detrimental effect on the durability of the contact surface by an increased probability of grinding-related damage initiation. However, no quantification of the allowable grinding groove depth or white etching layer thickness is made yet. These observations lead to two recommendations for further research.

  - Perform experiments to determine whether roughness height (variations) of the freshly ground surface and surface wear can be balanced, allowing the roughness to be fully worn before a low wear rate sets in. If such roughness height (variation) exists it is expected to be different for different steel grades

and loading conditions. The assumption that was made, based on the observations in this study, is that a contact surface with lower roughness, and without the presence of locally deeper grinding grooves, has a better durability.

- The second recommendation is to invest in process development that allows cutting depths to be increased without developing detrimental surface features such as WEL, metallographic burn and incidental deep grinding grooves. In some industries experiments take place using new abrasives, for example cubic boron nitride (CBN) combined with cooling of the grinding wheel, resulting in a more favorable heat partitioning [1, 2].

- The vertical-axis grinding causes facets on the freshly ground surface. The effects of high local contact stresses in the facet-transition zones, as found in the literature, are also observed in the grinding field test. Although facet transitions were not indicated as specific damage initiation sites, it is not fully understood yet which facet transition characteristics are allowable. Three recommendations for further research were formulated.

  - Study the contact surface formation and quantify the evolution of the deformation beneath the surface using technologies that reveal microstructural details like electron backscatter diffraction (EBSD). The objective is to gain better understanding of the process and the critical aspects of the transition zone.
  - Design research experiments to determine the allowable facet plane angle ranges given a certain wheel load, to avoid damage initiation caused by localized stress concentrations. This allowable facet plane angle determines the minimum number of facets at the rail surface, and thus the minimum number of grinding wheels needed to finish the ground surface.
  - Design research experiments to determine allowable grinding groove depth variations at the facet transitions. This recommendation relates to the research recommendations on allowable surface roughness.

Once, by performing the above-mentioned research, quantitative relationships between surface properties, their limits, and the probability of damage initiation have been established, it can be implemented and applications can be developed.

When developing specifications and equipment, profile variations that are present in practice must be taken into account. These variations are the result of differences in wear and local rail replacements, and require different grinding depths for reprofiling.

As the grinding depth increases, the intensity of the friction between the abrasive particles and the surface also increases, and thus the heat production. To design a robust grinding process that minimizes the formation of damage promoting surface features, it is essential to study these variations.

[1] S. Malkin, C. Guo (2007), "Thermal analysis of grinding". In: CIRP Annals 56, pp 760-782.
[2] A.S. Lavine, S. Malkin, T.C. Jen (1989), "Thermal aspects of grinding with CBN wheels". CIRP Annals 38, pp 557-560.

Rail manufacturers have optimized the chemical composition of rail steel and introduced controlled, accelerated cooling after hot rolling to improve mechanical properties and to reduce wear. The investments were made to extend the service life of the rails and the grinding intervals for users. Despite these investments, there are still some knowledge gaps regarding the relationship between microstructure and the mechanical properties of pearlitic steels, particularly in the areas of fatigue crack growth and fracture toughness.

Experimental research and characterization of air-cooled hypereutectoid rail steel have shown that the grain size of the pearlite colony and the misorientation angles between the pearlite colonies are important indicators of the fracture toughness of pearlitic steels.

The research results indicate that improvements in the production process are necessary to further optimize the mechanical properties of railway steel and its final microstructure and to capitalize on all the investments in composition.

Hot rolling temperatures still seem to be primarily determined by the forces and roller wear that occur during rolling. However, by adjusting hot rolling temperatures, the pearlite grain size and the pearlite colony orientation can be controlled. Therefore, it is advisable to investigate whether lowering the rolling temperature will improve the mechanical behavior, making investments in the chemical composition even more effective.

List of Figures

6

LIST OF TABLES

A

Preparations and lessons learned from the track test

A

A.1. INTRODUCTION

Performing experiments in an in-service track has the advantage that, in this research project, the ground rail surface is exposed to a wide variety of train traffic and to all other external influences that may be present. Some of these influences might never be considered when an experiment is performed under fully controlled conditions.

The specific circumstances also pose challenges. For example, the experiment cannot simply be interrupted for further examination of the surface condition at hand or because a desired surface condition is reached. Another challenge concerns the generalizability of the results. The experimental results are found for a specific test location. How can generalizability be taken into account in the design?

The purpose of this Appendix A is to show how the above-mentioned challenges were addressed in the experimental design, the results of which are described in Chapter 2. First, the main objectives and research questions are presented in section A.2. Section A.3 shows the specific preparatory activities that were carried out. The experimental design and the metallographic quick-scan, that is introduced as a check point, are introduced in section A.4. Finally, section A.5 presents the main lessons learned regarding the design and execution of field tests.

A.2. OBJECTIVES AND RESEARCH QUESTIONS

In the literature study, as presented in the introduction of Chapter 2, knowledge gaps were identified with regard to the breaking-in behavior and defect initiation mechanisms in the ground rail surface.

The surface condition of the rail that is installed before the experiment is defined by the stationary pre-installation milling, which is performed to remove the decarburized layer. The surface condition after 14 days in service is shown in Figure 2.3B, and is, during in-situ grinding, replaced by the ground surface condition, Figure 2.3C.

After grinding, a process of breaking-in starts. Characteristic aspects of the breaking-in are discussed in Chapter 4 and comprise surface roughness reduction, deformation and wear. During the breaking-in process, wear may initially be high but should decrease during a controlled breaking-in process [1, 2]. Machine operators use well-defined procedures to go through this breaking-in phase, but in track breaking-in is not controlled.

In the literature various loading conditions and mechanisms that can cause damage to rails are described. Concerning the ground rail surface, damage may initiate at transition zones between ground facets [3, 4] or at deeper grinding grooves [5]. The presence of white etching layers (WEL), the result of heat generation in the friction zones of abrasive particles during deep grinding [6], might cause damage initiation in these layers or at the verge of them [7]. Another mechanism is damages initiation as a result of the hard and brittle WEL being pressed into the softer matrix [8].

After studying the available research results regarding the running-in of the ground rail surface condition, the following two questions were formulated:

- How do the surface and subsurface conditions of a ground rail made from steel with improved wear properties, evolve?
  - What phases can be distinguished in the development of the contact surface? And what mechanisms play a role?
  - Are, at the contact surface, indications of the occurrence of high wheel slip present, for instance, adhesive material exchange and white layer formation?
  - If observed, at which transverse position on the rail do damages initiate?
  - Do these damages propagate to larger cracks, or are these worn off?
- Which features of the ground surface condition wear off and which may contribute to the development of damage?

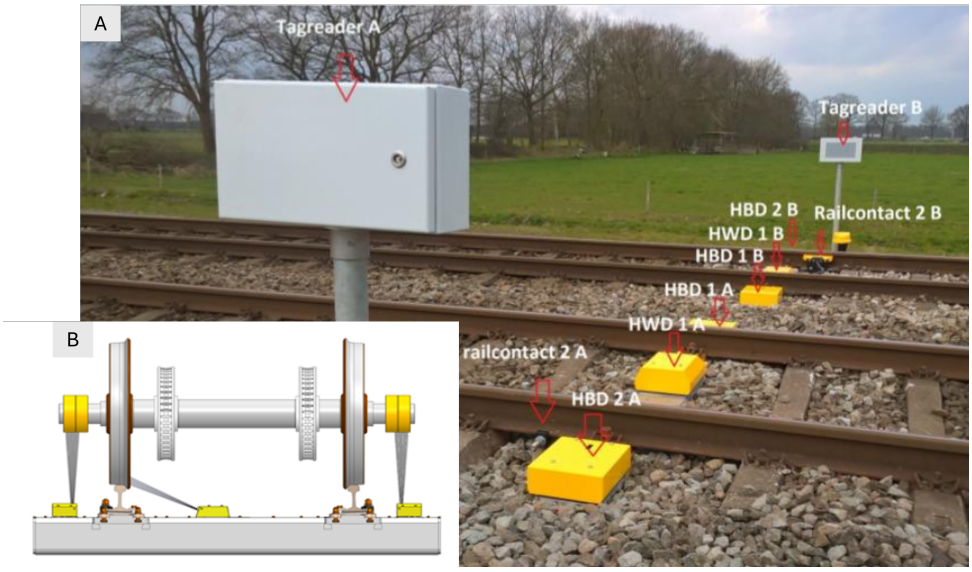

Figure A.1: A double track site with the hot axle box detector (HBD) and hot wheel detector (HWD) for train measurement. A) An overview of the detector site with RFID-tag readers to identify trains and the in-track detectors to measure wheel temperatures and axle box temperatures. B) Illustration of the detector site demonstrating the measurement positions and directions.

A.3. PREPARATIONS

For experiments conducted under controlled conditions, a relevant test setup and conditions must be selected, and experimental procedures and samples must be prepared. Conducting an experiment on a live track requires the coordination of necessary operational activities, such as the coordination between the installation of new rail to ensure a damage-free surface before grinding, and the performance of the preventive grinding maintenance itself. Because maintenance schedules are fixed, the inspection and removal of the rail were scheduled as much as possible before the start of the experiment.

This chapter presents two specific aspects of the preparation of the experiment; the site selection and a reference project that was carried out to determine inspection moments.

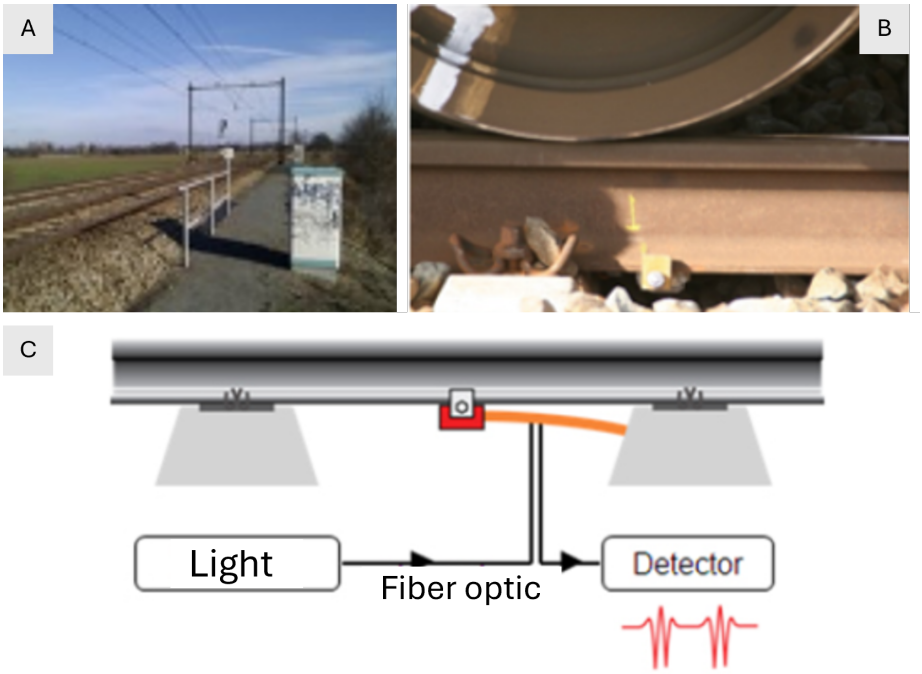

Figure A.2: Weighing in motion system. A) A measurement site. B) One of the 7 rail sensors that is installed on each rail. C) The schematic representation of the fiber optic system.

SITE SELECTION

The location selection is based on several operational criteria related to feasibility and criteria related to the experimental design.

- Accessibility and safety. The site, as presented in Figure 2.1, is easily accessible from the level crossing. The double track situation and the unobstructed view in both directions allow for daylight inspections.

- The load on the test site and the trains that pass. In the experiment the load which the ground rail has to endure cannot be controlled, but trains can be measured. One of the selection criteria therefore was the presence of a weighing-in-motion unit.

  Close to the test site a hotbox detector, see Figure A.1, is present. All trains are identified by the hotbox detector and coupled to measurement results of weighing-in-motion systems, see Figure A.2. The results are presented in Table 2.2.

Figure A.3: Running surface of the rail made from rail steel with improved wear properties. The arrows indicate the squat-type defects that are present. Defects cause only minor subsidence of the surface which is typical for rails made from these steels.

- History of rail damages. If damage to the rails at the selected location has occurred in the past, this is an indication that the loading conditions are such that damage may initiate during the experiment. For the selected test site it is known that, after standard R260Mn rails were installed, head check defects developed. After rails with improved wear resistance, R370CrHT rail grade, were installed squat-type defects [9] or grinding-related damages [8] developed. The results of the track inspection before the start of the experiment confirmed this, see Figure A.3. The available indications about the time to defect initiation for different types of defects show that a test duration of 7 to 10 MGT should be sufficient [8, 9, 10].

REFERENCE PROJECT

One of the challenges of conducting an experiment in an in-service railway line is that rail transport always has priority, both during the day and at night, and maintenance windows for inspection are limited.

In order to schedule daylight inspections and to select moments when rail samples can be extracted from the track for detailed analysis, the literature was studied and a reference project was carried out. In the literature some references are found for the roughness reduction and damage initiation as a function of load cycles or train load [3, 8, 9, 11].

A freshly ground rail on a railway line that sees only 80 trains per day was inspected daily to determine the rate at which the contact surface forms. Figure A.4 presents an impression of the reference location and the evolution of the freshly ground rail surface.

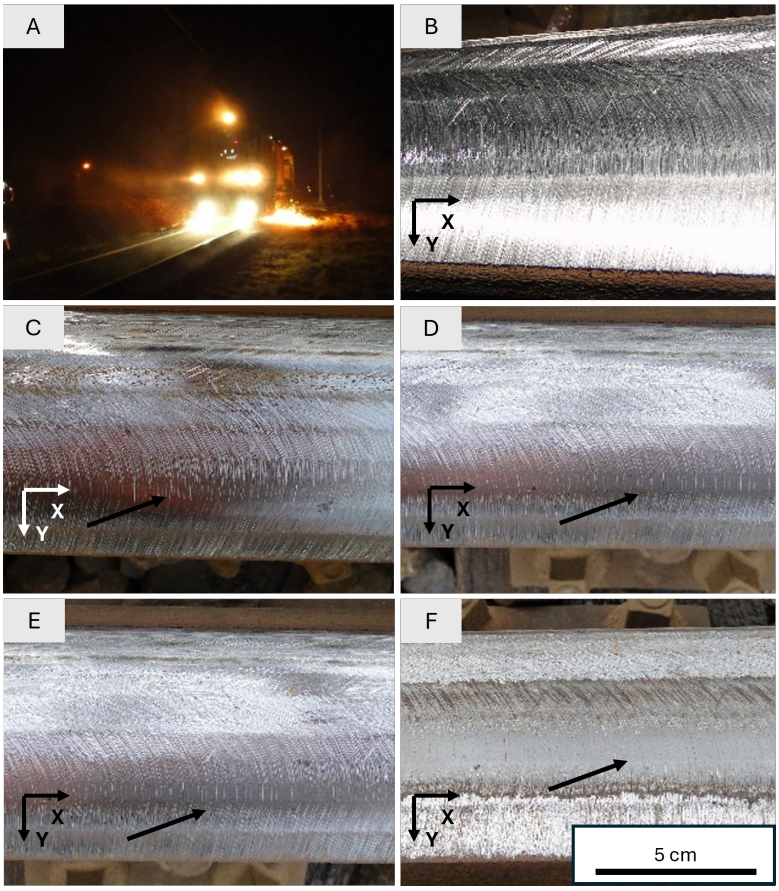

Figure A.4: Impressions of the evolution of the ground rail surface. A) Grinding performance. B) Freshly ground rail. C) Rail surface after 60 train passages, 1050 wheel passages and 13 kt of axle load. D) Rail surface after 140 train passages, 2400 wheel passages and 31 kt. E) Rail surface after 220 train passages, 3800 wheel passages and 49 kt. F) Rail surface after 440 train passages, 7700 wheel passages and 100 kt.

A.4. EXPERIMENTAL DESIGN

The experimental design is described in Chapter 2. In this section two additional aspects of the preparation are described; the inspection and replacement scheme, and the quick-scan that was introduced.

The inspection and replacement scheme contains the observation positions and extraction positions with identifiers for the location, see Figure A.5.

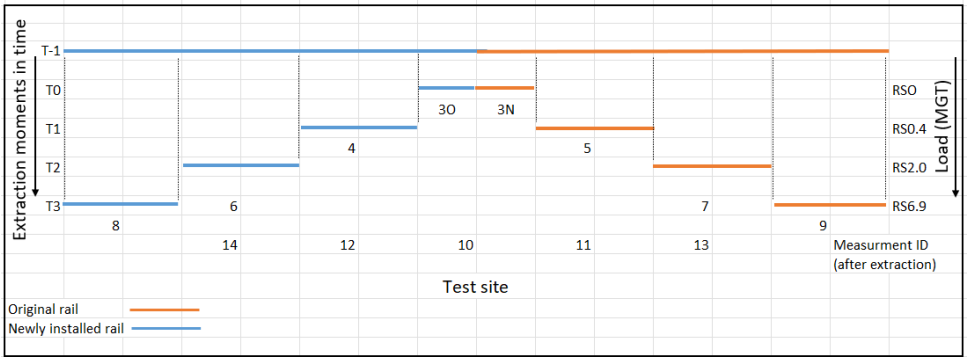

Figure A.5: The scheme for the extraction of rail samples and observation positions. On the left the installation, (T-1), and extraction moments, T1-T3, in time, are presented. On the right the sample identifiers used in Chapter 2, with the rail load since grinding in Mega tonne, is shown. The analysis presented in Chapter 2 only concerns the new rail with 3N (new), 5, 7 and 9 (identifiers during the project).

After extraction of the rail sample a metallographic quick-scan was made. The results are used to gain insight into the current surface condition so that decisions can be made about the next steps in the experiment. The final analysis that is presented in Chapter 2 is made after the finalization of the experiment. An example of such a quick scan is presented in Figures A.6 and A.7.

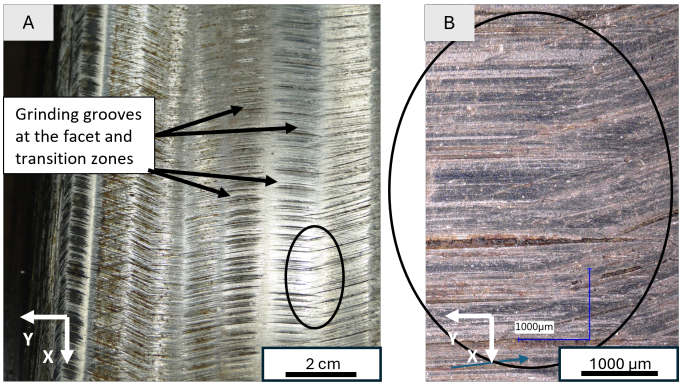

Figure A.6: Quick scan of the surface of RS0.4. A) The contact surface formation. B) A deeper grinding groove at the facet transition zone.

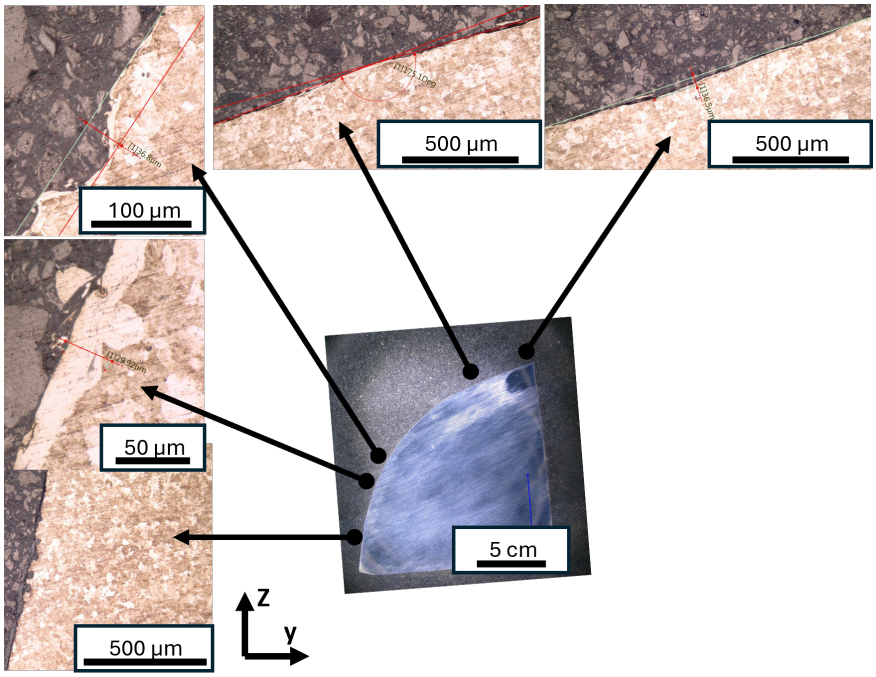

Figure A.7: Quick scan of RS0.4. The inserted metallographic microscope images show the surface condition at various positions of the gauge corner of the ground rail.

An overview of all inspections and measurements is presented in Table A.9 at the end of this appendix.

A.5. LESSONS LEARNED

In the previous sections additional information on the experimental design and preparations were presented. Despite the careful preparations, there are a number of points of attention for future experiments in in-service track.

- The freshly ground track surface undergoes rapid changes at the beginning of the experiment under the influence of passing trains. This was also observed in the reference project, and the inspection frequency was adjusted accordingly.

  The reference project was conducted on a tangent track section where a standard R260Mn steel rail was installed. Although some localized wear was observed a gradual and uniform reduction in roughness took place. The experiment itself was carried out in a curved track section.

  The reference project has contributed to the successful performance of the experiment in track. Nevertheless, differences in track lay-out and track use resulted in different observations of the rail wear.

- The wear processes occurring on the rail surface were evaluated using scanning electron microscopy (SEM) at low magnifications. The large depth of field of SEM is a well-known property and actually performing surface analyses using SEM showed the true capability of the method.
- Despite the fact that trains and train wheels are large, it was observed that the local processes that take place on the rail surface are crucial. In Chapter 2, Figure 2.6 the results of these localized processes are shown. See also Chapter 3 and reference [12].
- Local variations in wear and loading of rail surfaces that develop over time can best be studied by properly aligning all rail samples taken from the track. This experiment has shown that the characteristic length of the grinding process must be respected.
- To document the changes in surface condition in detail, it was decided to make replicas of the surface for later analysis. A fast-curing, two-component silicone rubber compound was used for this purpose. These replicas were made at the same rail position during every inspection. The analysis has not yet been performed for the following reasons:
  - Although all replicas are made at the same position on the rail surface, aligning the replicas and identifying the locations of interest using a 3D optical profilometer, which characterizes a small area, has proven to be time-consuming. A separate research project needs to be initiated for this purpose.
  - The wear of the rail surface is high, which resulted in wear particles ending up in the replicas even after cleaning the surface. The reflection of these wear particles results in measurement errors when interpreting the surface profile. See Figure A.8 for the first images of the surface.

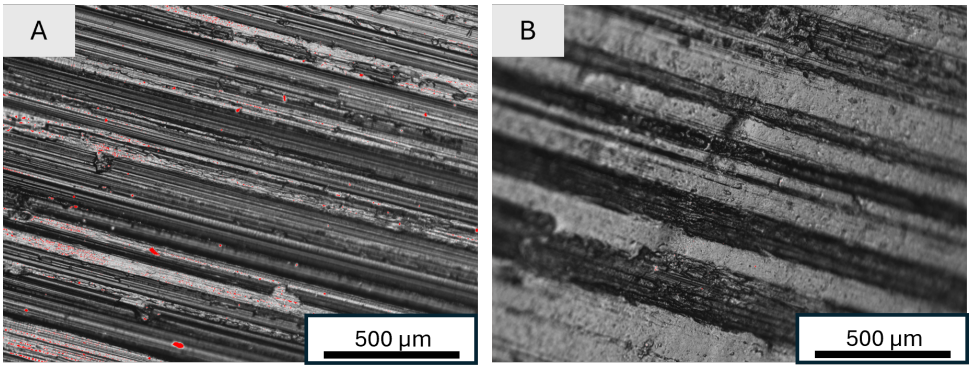

Figure A.8: Confocal images of the replicas of the rail surface which are used for 3D profile analysis. A) The freshly ground surface. B) The surface of the rail after it was in use for a day after grinding

Sample	Inspection type	Share of cum. load after grinding (%)	Date	Inspection findings	Surface roughness R_a (stdev)(µm)	Surface roughness R_v (stdev)(µm)	Hardness Hv (stdev)	Replica	Transverse profile measurement
	Night	installation	28 March	Rail installation Milled surface with longitudinal grinding pattern			410 (20)		Yes
1	**Night**	**0.0%**	**13/14 Apr**	**In-situ grinding fresh ground surface, light coloration in two facets**	**5.52 (1.06)**	**20.27 (4.08)**	**386 (22)**	Yes	Pre-and post-grinding
	Daylight	0.0%	14-Apr	Repetitive waviness in daylight					
	Daylight	0.5%	15- Apr	Surface smoothening at 1 facet on top of the rail				Yes	
	Daylight	1.1%	17- Apr	surface smoothening expands to adjacent facets				Yes	
	Daylight	1.7%	19- Apr	Wide smoothened zones, deeper grooves in transition zones become visible				Yes	
	Daylight	3.4%	24- Apr	Progressing wear, within corroded surface small contacts are visible				Yes	
2	**Night**	**6.2%**	**2-May**	**Sample 2 extraction**	**3.07 (1.02)**	**14.04 (4.15)**	**394 (13)**	Yes	Yes
	Daylight	11.5%	16-May	Widening of the contact surface, facets show various stages of wear				Yes	
	Night	15.7%	30-May	Clear pattern of deep grooves	2.29 (0.37)	12.70 (1.70)	386 (8)	Yes	
	Night	23.5%	20-June	Shallow damage, initiating at the surface damage from maintenance	2.18 (0.70)	12.36 (2.83)	390 (13)	Yes	
3	**Night**	**29.5%**	**4-July**	**Sample 3 extraction**	**2.49 (1.15)**	**11.51 (4.13)**	**399 (8)**	Yes	Yes
	Daylight	50.0%	21-Aug	Running band; deep grooves in the center, clear pattern at both sides				Yes	
	Night	74.1%	17-Oct	Same patterns although more shallow	1.48 (0.70)	8.73 (4.19)	406 (10)	Yes	Yes
	Daylight	96.4%	9-Dec	Small crack from roughness, repetitive patterns					
4	**Night**	**100.0%**	**18-Dec**	**Sample 4 extraction, finish grinding field test**	**1.34 (0.73)**	**6.36 (2.62)**	**406 (22)**		

Figure A.9: The inspections, measurement results, and visual characterization. The measurement results of measurements performed in the lab are presented in bold text.

BIBLIOGRAPHY

[1] P.J. Blau. "On the nature of running-in". In: *Tribology International* 38.11-12 (2005), pp. 1007–1012. ISSN: 0301679X. DOI: 10.1016/j.triboint.2005.07.020.

[2] S. Fukagai et al. "Transitions in rolling-sliding wheel/rail contact condition during running-in". In: *Tribology International* 149 (2020). ISSN: 0301679X. DOI: 10.1016/j.triboint.2019.03.037.

[3] F. Fau et al. "Effect of grinding quality, lubrication quality and rail hardness on flaking defect initiation on high rails". In: *Proc. 10 th Int. Conf. Contact Mech. Wear Rail/Wheel Systems CM2015, Colorado, USA*. Vol. 30. 2015.

[4] M. Mesaritis et al. "Post-field grinding evaluation of different rail grades in full-scale wheel/rail laboratory tests". In: *Tribology International* 177 (Jan. 2023). ISSN: 0301679X. DOI: 10.1016/j.triboint.2022.107980.

[5] B. Schotsman. *Spalling defects in MHH steel rails, a study on the defect initiation and spalling after aggressive grinding*. Tech. rep. Utrecht: ProRail, Oct. 2017.

[6] Z.B. Hou and R. Komanduri. "On the mechanics of the grinding process, Part II - Thermal analysis of fine grinding". In: *International Journal of Machine Tools and Manufacture* 44.2-3 (Feb. 2004), pp. 247–270. ISSN: 08906955. DOI: 10.1016/j.ijmachtools.2003.09.008.

[7] R.I. Carroll and J.H. Beynon. "Rolling contact fatigue of white etching layer: Part 1. Crack morphology". In: *Wear* 262.9-10 (Apr. 2007), pp. 1253–1266. ISSN: 00431648. DOI: 10.1016/j.wear.2007.01.003.

[8] M. Steenbergen. "Rolling contact fatigue in relation to rail grinding". In: *Wear* 356-357 (June 2016), pp. 110–121. ISSN: 00431648. DOI: 10.1016/j.wear.2016.03.015.

[9] S.L. Grassie. "Squats and squat-type defects in rails: the understanding to date". In: *Proceedings of the Institution of Mechanical Engineers, Part F: Journal of Rail and Rapid Transit* 226.3 (2011), pp. 235–242. ISSN: 0954-4097 2041-3017. DOI: 10.1177/0954409711422189.

[10] M. Hiensch and N. Burgelman. "Rolling contact fatigue: Damage function development from two-disc test data". In: *Wear* 430-431 (2019), pp. 376–382. ISSN: 0043-1648. DOI: https://doi.org/10.1016/j.wear.2019.05.028. URL: https://www.sciencedirect.com/science/article/pii/S0043164818313991.

[11] H. Chen and M. Ishida. "Influence of Rail Surface Roughness Formed by Rail Grinding on Rolling Contact Fatigue". In: (2006).

[12] S. Simon et al. "Tribological characterization of rail squat defects". In: *Wear* 297.1-2 (Jan. 2013), pp. 926–942. ISSN: 00431648. DOI: 10.1016/j.wear.2012.11.011.

ACKNOWLEDGEMENTS

This thesis is the result of my Ph.D.-project that started in 2019. It has been a challenging and inspiring time in which I have met many new people. Many of them have inspired me and have contributed to my research, the results of which are presented in this dissertation. I would like to thank them here.

First I would like to thank my promotors, Jilt Sietsma, Maria Santofimia Navarro, and Roumen Petrov, for their continuous support.

Jilt, the idea for this Ph.D.-project originated from my graduation project of the metallurgy course at the University of Applied Sciences Utrecht. Erik Vegter was my supervisor and, as a committee member, you had to assess my work. We had to write the research proposal and find funding to expand the graduation work into a Ph.D. research project, which we succeeded in doing. I started this Ph.D.-project on January 1st, 2019, part-time for 2 days a week.

My personal motivation was twofold: first, curiosity and the desire to gain a better understanding of railway steels and second, to develop the professional skills for an inspiring second half of my career. Infrastructure manager ProRail wanted to gain more insight into the crack susceptibility of ground rails to be able to adjust grinding maintenance programs.

I am truly grateful for the opportunity you provided me to start this Ph.D.-project. I got to know you as a highly dedicated supervisor who is always alert to what could and perhaps should be improved in my work, and who, at the same time, always showed genuine interest in me as a person. I have to thank you for all the discussions we had. It helped me sharpen my thoughts and improve my research results. One of your, often-used, comments will always be remembered by me. It is, in my words: *Is it really necessary to perform additional experiments? Are you sure you've gotten the most out of the data you already collected?*

I had both the privilege and challenge to work with three supervisors, each with their specific interests, approach, and strengths.

Maria, during the project you gradually got more and more involved. Especially during the last two years you helped me with planning and scheduling. It was also nice to follow your course *Steel science* and to study and discuss research articles from other research fields. I have to thank you for your detailed comments on my articles. These were always both positive and critical and foremost focused on the article structure. Your support helped me a lot in developing my writing style, to present research results in the clearest possible way, and finishing the Ph.D.-project.

Roumen, thank you for your contribution to my experimental designs. Your recommendations for sample preparation and not to forget, your critical feedback on my work. Your quick thinking and sharp questions during our meetings have challenged me to prepare meetings well, and to look critically at my own work and the choices I make.

A

The chapters in this thesis are the results of successful scientific collaborations with several researchers, both within Delft University of Technology and outside. Working with Vitória Mattos Ferreira (Delft University of Technology) has been a pleasure. I will remember your patience and precision in both sample preparation and the operation of microscopes. Several conference contributions and journal papers were written in co-operation with Davide Leonetti (Eindhoven University of Technology). Performing linear elastic fracture mechanics tests and the associated data analysis as presented in this thesis, opened a new research field for me. Visiting a conference in Rome, ending up discussing the perfect recipe for *pomodore* preparation with passionate Italian researchers, will be remembered as one of the highlights of our collaboration. I hope that in the near future we can continue to conduct joint research to contribute to the reliability of the railways.

One of the advantages of starting a Ph.D.-project later in my career is that I could fall back on a professional network. It was wonderful to be able to consult many people from that network and discuss my research approach and findings. Matthijn de Rooij (University of Twente), Henk Slot (TNO), Martin Hiensch, Thijs Hendrikx, Patrick Gottmers, Jari Boesten (Dekra Rail), Stephen Lewis, Andrew Wilson, and Jacob Corteen (British Steel), Luuk Kurvers (Strukton Rail), Bert Bakker (Volker Rail), and everyone I haven't thought of right now. Thank you for the interesting discussions, suggestions, and active involvement to make this project a success.

The research approach of this project is strongly experimentally oriented and the results were obtained by performing specifically designed experiments. It required the assistance of several specialists who were willing to teach, help, discuss and support in both design and analysis of the results. I am thankful to Kees Kwakernaak, Remko Seijffers, Nico Geerlofs, Hans Hofman, Jurriaan van Slingerland, Durga Mainali Sharma, and Vitaly Bliznuk (University of Ghent).

During my time working in Delft, I always felt very welcome. Prisca Koelman and Reina Boerrigter were always interested in my work and progress. During my project, I shared the office with Peter van Liempt and Jan van Turnhout. I would like to thank both of them for their support, pleasant atmosphere and the informative discussions.

I have to thank my ProRail colleagues. Special thanks to Taco Sysling for the support to start this project and Danielle van den Aardweg for making more time available when it was needed most to write this thesis. Edwin Gelinck, Martine Teijgeler, Jeroen Smulders, Niels de Wit, Maider Oregui Echeverria-Berreyarza, Coen Valkenburg, Sharon Michielsen, Niek van de Koppel, as my direct colleagues, thank you for your support, showing interest and give me time to complete this project.

Finally, the most important person to thank is my wife, Marit. I know you preferred not to be mentioned here, but without your patience and understanding this project would never have been possible. I am extremely grateful to you for that.

It was my personal ambition to pursue a Ph.D.-project, knowing it would likely require most of my free time as well. Now that I've finished, a period of reflection begins for me to determine how I want to continue my career.

BIOGRAPHY

Bart SCHOTSMAN

Bart Schotsman is a senior railway specialist employed by the Dutch rail infrastructure manager ProRail. He works on various topics related to railway rails, such as rail grade selection, rail maintenance, and rail inspection.

Besides maintenance management of the rail infrastructure, Bart also works on research projects to improve rail service life, to find the root cause of unexpected failures and the future perspective of rail steels, especially decarbonization and recycling.

What characterizes Bart's approach is that he combines both practical and theoretical perspectives. To determine causes of failure, field observations are combined with data analysis and available scientific research results.

Bart received a bachelor's degree in Mechanical Engineering at the TH Rijswijk in 2002. At the TUe, a part-time master in Technology Policy, with a specialization in numerical modeling, was completed with a master's degree in 2009. During his professional career Bart has taken post-bachelor courses on maintenance technology and metallurgy to acquire the basic knowledge for further specialization in inspection techniques, maintenance management and the maintenance and selection of railway rails.

Professional career

2015	-		ProRail, senior track specialist, working on: Rail grade and rail profile selection. Inspection, sizing and criticality of rail defects. Rail maintenance; grinding and milling programs. Research on grinding effectiveness, crack growth, new steel types, lubrication and circularity in production of railway steel.
2012	-	2015	ProRail, track specialist and department manager, working on: Scheduling of track and switch replacements, and on the analysis and prevention of repetitive failures. Department manager of the regional Technology and Analysis department in Rotterdam.
2008	-	2012	ProRail, track monitoring specialist, working on: Analysis of track measurement data, and on design and specification of measurement systems. Project manager in projects for the purchase and contracting of measurement systems and services.
2006	-	2008	Statistics Netherlands. Researcher.
2002	-	2006	THRijswijk and Rotterdam University of Applied Sciences. Teacher of control systems engineering.

Education

2019	-	2025	Delft University of Technology, ME, Materials Science & Engineering, Microstructures of metallic materials. Ph.D.-research project *Fundamental study of contact fatigue strength of rail after grinding*. Thesis entitled: *Damage behavior of ground pearlitic railway steel.*
2015	-	2017	University of Applied Sciences Utrecht, Metallurgy (post-BSc). Graduation project: *Spalling defects in MHH steel rails, a study on the defect initiation and spalling after aggressive grinding.*
2011	-	2012	University of Applied Sciences Utrecht, Maintenance Technology (post-BSc).
2003	-	2009	Eindhoven University of Technology, Faculty of Technology Management. Technology & Policy, MSc. thesis: *Productivity growth dynamics in the EU.*
1999	-	2002	TH Rijswijk, Mechanical Engineering (BSc), Production Technology and Energy Technology. Graduation project: *Design and realization of a dosing system for low-pressure resin injection production using epoxy.*
1997	-	1999	Utrechts Conservatorium.

List of Publications

Journal papers related to the thesis

- **B. Schotsman**, M.J. Santofimia, R.H. Petrov, J. Sietsma, *Surface characterization and microstructural evolution of railway rails in a medium-wide curve after preventive grinding*, Wear, 2025, Volumes 580–581, 206237, ISSN 0043-1648, https://doi.org/10.1016/j.wear.2025.206237.

- **B. Schotsman**, J. Huisman, M.J. Santofimia, R.H. Petrov, J. Sietsma, *Microstructure evolution and damage development in the rails of a single-track railway line after preventive grinding*, Wear, 2025, Volumes 576-577, 206101, ISSN 0043-1648, https://doi.org/10.1016/j.wear.2025.206101.

- **B. Schotsman**, V. Mattos Ferreira, D. Leonetti, R.H. Petrov, M.J. Santofimia, J. Sietsma, *Experimental investigation on the fatigue and fracture toughness properties of hypereutectoid rail steel*, Engineering Fracture Mechanics, Volume 313, 2025, 110657, ISSN 0013-7944, https://doi.org/10.1016/j.engfracmech.2024.110657.

Other journal papers

- D. Leonetti, **B. Schotsman**, *Experimental investigation on the fatigue and fracture properties of a fine pearlitic rail steel*, Fracture and Structural Integrity, 18(69), 2024, 142–153, https://doi.org/10.3221/IGF-ESIS.69.11.

Conference papers

- D. Leonetti, V. Mattos Ferreira, **B. Schotsman**, *Fracture behavior and mechanical characterization of R350HT rail steel*, Procedia Structural Integrity, Volume 47, 2023, 219-226, ISSN 2452-3216, https://doi.org/10.1016/j.prostr.2023.07.015.

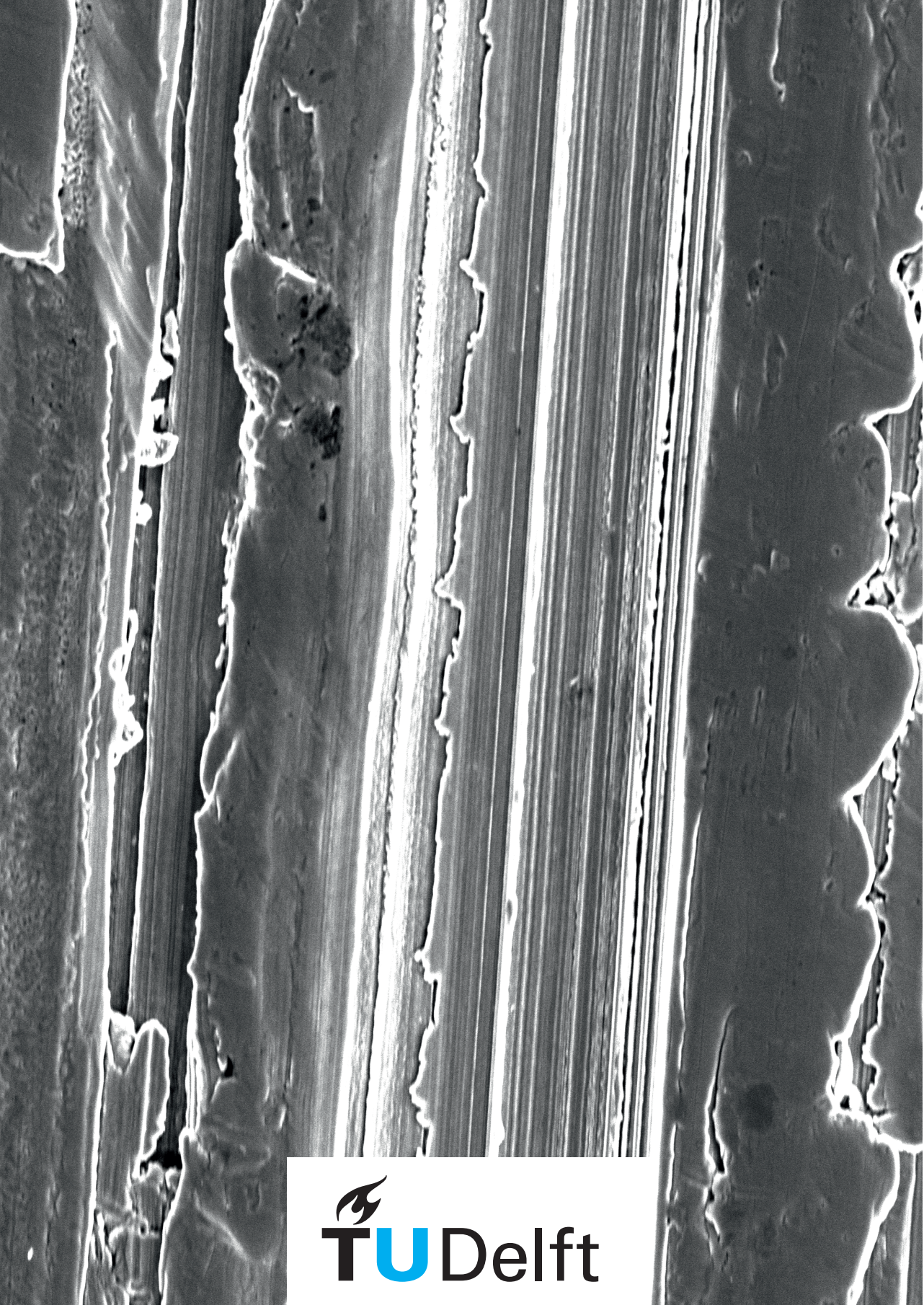
TU Delft